



Brno University of Technology
Faculty of Mechanical Engineering
Institute of Machine and Industrial Design

Vysoké Učení Technické v Brně
Fakulta strojního inženýrství
Ústav konstruování

PROCESSING OF METALLIC MATERIALS BY SELECTIVE LASER MELTING AT ELEVATED TEMPERATURES

ZPRACOVÁNÍ KOVOVÝCH MATERIÁLŮ SELEKTIVNÍM
LASEROVÝM TAVENÍM ZA ZVÝŠENÝCH TEPLŮT

Ing. Martin Malý

Author
Autor práce

doc. Ing. Daniel Koutný Ph.D.

Supervisor
Vedoucí práce

Dissertation Thesis
Dizertační práce

Brno 2022



Brno University of Technology
Faculty of Mechanical Engineering
Institute of Machine and Industrial Design

Vysoké Učení Technické v Brně
Fakulta strojního inženýrství
Ústav konstruování

PROCESSING OF METALLIC MATERIALS BY SELECTIVE LASER MELTING TECHNOLOGY AT ELEVATED TEMPERATURES

ZPRACOVÁNÍ KOVOVÝCH MATERIÁLŮ SELEKTIVNÍM LASEROVÝM TAVENÍM
ZA ZVÝŠENÝCH TEPLŮT

Ing. Martin Malý

Author

Autor práce

doc. Ing. Daniel Koutný Ph.D.

Supervisor

Vedoucí práce

Dissertation Thesis

Dizertační práce

Brno 2022

STATEMENT

I hereby declare that I have written the PhD thesis *Processing of metallic materials by Selective Laser Melting technology at elevated temperatures* on my own according to advices of my supervisor doc. Ing. Daniel Koutný, Ph.D., and using the sources listed in references.

Brno, _____

.....

Ing. Martin Malý

BIBLIOGRAFIC REFERENCE

MALÝ, M. *Processing of metallic materials by Selective Laser Melting technology at elevated temperatures*. Brno, 2022, 127 p. PhD thesis. Brno University of Technology, Faculty of Mechanical Engineering, Institute of Machine and Industrial Design. Supervisor: doc. Ing. Daniel Koutný, Ph.D.

ACKNOWLEDGEMENT

I would like to express my thanks to all the people who supported me during my doctoral studies. First of all, I have to mention the supervisor doc. Daniel Koutný, Ph.D., who gave me support whenever it was needed. I also thank my colleagues from REAT group and colleagues from TU Graz who made a friendly work place for me. Thank to doc. Libor Pantělejev, Ph.D. and doc. David Paloušek, Ph.D. for your advices. Many thanks to my family for your support. Without you, my studies would not be possible to finish.

ABSTRACT

This dissertation thesis deals with the influence of preheating on the components produced using Selective Laser Melting (SLM), also known as Laser Powder Bed Fusion (LPBF) technology. The thesis contains an overview of the current state of knowledge in the field of preheating and the physical nature of preheating. Furthermore, the work contains an overview of the effect of preheating on specific types of materials. These types of materials included in the state of the art are titanium, intermetallic, nickel and aluminium alloys, and copper. From the state of knowledge, promising research areas were identified, where preheating could lead to more efficient production using LPBF technology and to expansion of the area of processable materials. These areas include the investigation of the effect of preheating in combination with other process parameters on the residual stresses of Ti6Al4V alloy, the effect of preheating on nickel alloy Inconel 939 and copper. The premise of the Ti6Al4V and Inconel 939 topics was that preheating would reduce residual stresses, and thus will be possible to reduce the necessary amount of support structures. The results can lead to more cost-effective production using LPBF technology. This hypothesis was rejected. Despite the reduction in residual stresses in Ti6Al4V, they were not fully eliminated and, in addition, a rapid degradation of unused powder was detected, which increases production costs. The preheating of the Inconel 939, against the assumption based on behaviour of other materials, led to higher deformations and thus residual stresses, due to the evolution of precipitates. Another selected area where preheating could lead to an increase in the portfolio of processable materials is the processing of copper. Copper is a difficult to process material using LPBF technology due to its high thermal conductivity and laser reflectivity. The experiments confirmed a very positive effect of preheating on the relative density of the samples. The samples reached relative density values of over 99% when fabricated with preheating at 400 °C. Thus, preheating can significantly improve the process ability of reflective and high conductive materials. All of the results lead to a better understanding of the behaviour of the materials during processing by LPBF technology and may lead to its further expansion to more industries. The results are summarized in three publications that have been published in scientific journals.

KEYWORDS

Laser powder bed fusion, Selective laser melting, residual stress, preheating, Ti6Al4V, Inconel, copper

ABSTRAKT

Tato disertační práce se zabývá vlivem předehřevu na výrobu komponent 3D tiskem kovů technologií Selective Laser Melting (SLM), také známou pod označením Laser Powder Bed Fusion (LPBF). V práci je obsažen přehled současného stavu poznání v oblasti realizace předehřevu a fyzikální podstaty předehřevu. Dále je v práci obsažen přehled vlivu předehřevu na konkrétní typy materiálů. Mezi tyto typy materiálů byly zařazeny titanové, intermetalické, niklové a hliníkové slitiny a měď. Z rešeršní části byly identifikovány perspektivní oblasti, které doposud nebyly dostatečně zkoumány, a kde by předehřev mohl vést k zefektivnění technologie LPBF a rozšíření oblasti zpracovatelných materiálů. Mezi tyto oblasti bylo zařazeno zkoumání vlivu předehřevu v kombinaci s dalšími procesními parametry na zbytková napětí u slitiny Ti6Al4V, vliv předehřevu na niklovou slitinu Inconel 939 a na měď. Předpokladem u Ti6Al4V a Inconelu 939 bylo, že předehřev sníží zbytková napětí a bude tak možné snížit množství podpurných struktur během výroby, což by vedlo k zefektivnění technologie. Tato hypotéza byla zamítnuta, protože i přes snížení zbytkových napětí u Ti6Al4V nedošlo k jejich eliminaci a navíc, došlo k rychlé degradaci nepoužitého prášku, což zvyšuje náklady na výrobu. U Inconelu 939 dokonce zvýšená teplota vedla k vyšším deformacím, a tedy zbytkovým napětím v důsledku evoluce karbidické fáze. Další perspektivní oblastí, kde by předehřev mohl vést k zvýšení portfolia zpracovatelných materiálů, je měď. Měď je díky vysoké tepelné vodivosti a odrazivosti laserového záření považována za obtížně zpracovatelnou technologií LPBF. Z experimentů byl potvrzen velice pozitivní vliv předehřevu na relativní hustotu vzorků. Vzorky dosáhly hodnot relativní hustoty přes 99 % pokud byly tisknuty s předehřevem 400 °C. Bylo tedy experimentálně ověřeno, že předehřev může významně zlepšit zpracovatelnost skupiny materiálů, které mají nízkou pohltivost laserového záření a materiálů s vysokou teplenou vodivostí. Všechny výsledky vedou k lepšímu pochopení chování materiálů během zpracování technologií LPBF a mohou vést k jejímu rozšíření do dalších průmyslových odvětví. Výsledky jsou shrnuty ve třech publikacích, které byly vydány ve vědeckých časopisech.

KLÍČOVÁ SLOVA

Laser powder bed fusion, Selective laser melting, zbytková napětí, předehřev, Ti6Al4V, Inconel, měď

CONTENT

1	INTRODUCTION	12
2	STATE OF THE ART	14
2.1	Powder bed fusion technologies	14
2.2	Residual stress in the Laser powder bed fusion	15
2.3	Preheating in the Laser powder bed fusion	17
2.4	Influence of preheating on the selected materials processed using LPBF	19
2.4.1	Titanium alloys	19
2.4.2	Intermetallic alloys	23
2.4.3	Steels	25
2.4.4	Nickel-based alloys	29
2.4.5	Aluminium alloys	33
2.4.6	Copper	36
3	ANALYSIS AND CONCLUSION OF LITERATURE REVIEW	40
3.1	Titanium alloys	41
3.2	Intermetallic alloys	42
3.3	Steels	43
3.4	Nickel-based alloys	43
3.5	Aluminium alloys	44
3.6	Copper	44
3.7	Summary	45
4	AIMS OF THE THESIS	46
4.1	Scientific questions	46
4.2	Hypotheses	47
4.3	Thesis layout	48
5	MATERIAL AND METHODS	50
5.1	Specimens fabrication	50
5.2	Powder characterization	50
5.3	Measurement methods	51

5.3.1	Residual stress measurement	52
5.3.2	Relative density measurement	52
5.4	Experimental design	52
6	RESULTS AND DISCUSSION	53
7	CONCLUSIONS	105
8	LIST OF PUBLICATIONS	108
8.1	Papers published in journals with impact factor	108
8.2	Papers in conference proceedings	108
9	LITERATURE	109
10	LIST OF FIGURES AND TABLES	121
10.1	List of figures	121
10.2	List of tables	123
11	LIST OF SYMBOLS AND ABBREVIATIONS	124

1 INTRODUCTION

Additive technologies are in development for more than thirty years. In contrast to conventional technologies, where parts are produced by material removal, additively processed parts are made by gradual addition of material just where is needed. The result is a near net shape part produced without a special requirement for tooling even from the hard to process materials. Thus, those techniques open new possibilities for unique shape designs that allow fabrication of even more efficient components. Those techniques are more suitable for producing individual components with complex geometries than for serial production.

The Laser Powder Bed Fusion (LPBF) also called Selective Laser Melting (SLM) is the wide-spread technology for producing metal components. This technology uses a laser beam, which selectively layer by layer melting a metal powder. The process begins with the spread of the metal powder on the solid platform which is consequently melted by the laser beam in a specific shape according to the geometry [1]. Then the next layer of the powder is spread, and melting process continues until a complete part is created (Fig. 1-1). The whole process is maintained in protective gas of argon or nitrogen. The mechanical properties of the components produced are comparable with the convention manufacturing technologies and are many times even better in static loading performance due to the specific microstructure [2, 3].

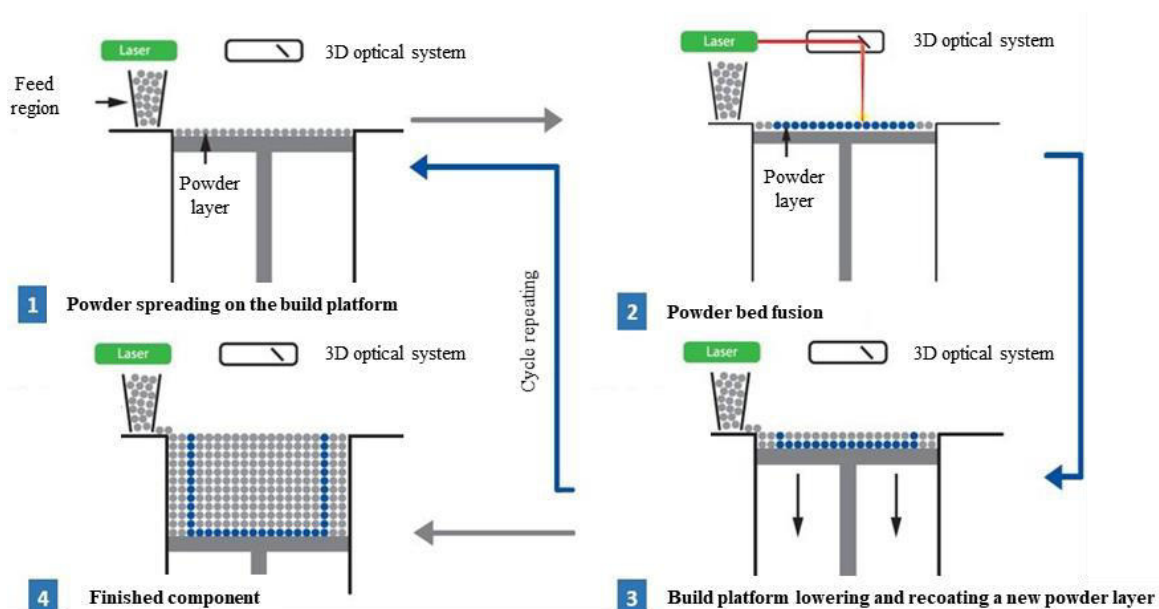


Fig. 1-1 Laser powder bed fusion (LPBF) production principle. [4]

The main challenges in the LPBF process that hinder the usability in even more applications are part accuracy, requirement of support structures, high surface roughness, low fatigue mechanical properties, and low amount of proven material.

Most of the issues mentioned here are related to the residual stress originating from the nature of LPBF technology. Nonhomogeneous heating and cooling lead to high-temperature gradients and the evolution of residual stresses [5]. The residual stress causing delamination, cracks and part deformation, thus the parts must be fixed to the build platform by volumetric material or support structures. The need of support structures limits designs with inner holes and channels where support removal is impossible. The support structures also prolong the build time, increase material consumption, and postprocessing effort. Furthermore, residual stress may cause cracks which are more common in materials with poorer weldability [6]. This restricts some materials from the process ability by LPBF technology. The thermal gradient and thus residual stress can be reduced by optimal set of laser-related process parameters, scanning strategy, or preheating of the build space [7–9]. The residual stress can also be eliminated after the production run using stress relieve annealing which can reduce residual stress by more than 70% [10], however, it cannot prevent failures during component production.

This thesis focuses on the application of high-temperature preheating in LPBF technology and its influence on residual stress, relative density, microstructure, and mechanical properties of a wide variety of material. The aim is to use elevated preheating temperatures to increase accuracy by reducing residual stress and distortion. Moreover, increase manufacture efficiency by decreasing the necessary amount of support structures and increasing the material portfolio by investigating hard-to-process material.

2 STATE OF THE ART

2.1 Powder bed fusion technologies

The standard terminology for additive manufacturing ISO/ASTM 52900:2015(E) defines powder bed fusion (PBF) technologies as the process where thermal energy selectively fuses regions of a powder bed. The technologies can be divided by source of thermal energy to Laser powder bed fusion (LPBF) and Electron beam melting (EBM). The EBM uses an electron beam for powder melting. The process is maintained in vacuum and usually high-temperature preheating is applied on the powder bed. The high-temperature preheating in EBM at temperatures from 600 °C to 1100 °C is usually performed on the build surface using the electron beam that is defocused and accelerated [11, 12]. The main focus of this thesis is on the LPBF technology which takes the largest share among the PBF technologies, more than 80% compared to EBM, due to lower machine costs and precise beam resolution [13].

LPBF uses a laser beam to melt the metal powder. The process is maintained in an inert atmosphere of nitrogen or argon. LPBF can process a large amount of materials including titanium, aluminium alloys, stainless steels, and nickel-based superalloys [14]. But researchers are still focused on the introduction of the new materials which can even increase the industrial acceptance of this technology [15]. The static mechanical properties reached by the processed components are comparable to those of conventionally fabricated [14]. Nevertheless, suitable process parameters must be used to reach a fully dense part. The non-optimal process parameters lead to defects such as gas porosity when too much energy is used. On the contrary, the lack of fusion and key hole porosity can occur when insufficient energy is used in the material [16]. Another obstacle for many industries is the repeatability and reproducibility issues caused by process complexity [17]. The fusion process is mainly influenced by the setting of the laser beam, which causes a nonhomogeneous rapid local heating and cooling of the material; thus, high thermal gradients occur [5]. Large thermal gradients cause nonhomogeneous thermal expansion of the material which leads to the introduction of residual stress. The residual stress are stresses that remain in material when equilibrium with the surrounding environment is reached [5]. The residual stress is the main factor that causes in-process deformations, warping, and cracks. Thermal gradients can be reduced by preheating of the part during the production run [8]. Powder bed preheating is commonly performed using a heated base plate up to 200 °C [4], but commercial systems capable of preheating up to 500 °C and 800 °C are now also available [18].

The main benefit of high-temperature preheating in LPBF is in lower temperature gradients, thus lower residual stress [19]. Furthermore, preheating decreases the energy necessary to melt the powder [20], increases the absorptivity of the material [21], changes the wetting conditions [22–24], and increases the timescale of solidification [25]. Thus, preheating in the LBPB has the ability to increase the portfolio of proven materials, increase the component accuracy, and production efficiency.

2.2 Residual stress in the Laser powder bed fusion

Residual stresses can be divided into three groups according to the scale on which they operate (Fig. 2-1a). Type I residual stresses operate on the length throughout the part or specimen, thus on the macroscopic scale [15]. Type I residual stress is mostly discussed and studied in the literature with regard to additive manufacturing because it is responsible for global deformations of the parts when their magnitude elevates the yield strength of material. Type II residual stress is caused by a local microstructural effect, such as the thermal and elastic properties in different orientation [5]. Type II residual stresses operate on the grain scale. Type III is caused by crystallographic disorders, such as vacancies, and substitutional atoms and operates on the atomic scales. Residual stresses of type II and type III are almost always present in polycrystalline material, but are difficult to measure [26].

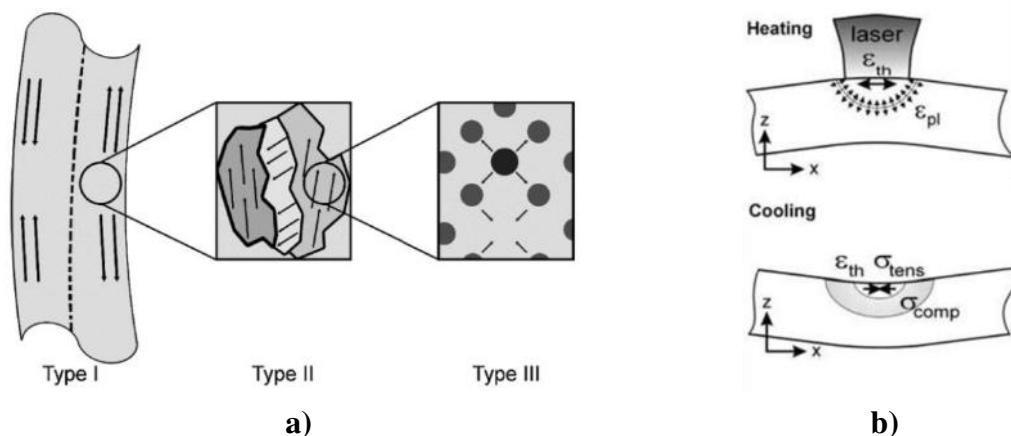


Fig. 2-1 a) Example of classification of residual stresses into three categories [15]; b) origin of the type I residual stress [27].

The macroscopic residual stresses of type I directly affect the mechanical properties and geometry of produced parts, thus they are only the type of residual stress discussed in the following text. They can also be directly affected by process conditions and laser settings. Thus, there are the most important with regards to part properties. The evolution of the type I residual stress is due to nonhomogeneous rapid heating from the laser source Fig. 2-1b. The laser source causes large thermal gradients that lead to nonhomogeneous thermal expansion of the material. The colder material beneath and around heated material restricts this expansion, which causes compression stress (Fig. 2-1b). The magnitude of compression stress may overpass the yield strength and thus plastic deformation may occur. During the cooling stage, the heated spot has a tendency to decrease its volume, which introduces tensile stress. The residual stress in the specimens is introduced in the two zones. Tensile stresses evolve on the upper and lower surfaces between the compressive stress zone in the middle of the specimen [27]. The greatest influence on residual stress has the material properties, geometry, stiffness of the base plate, scanning strategy, and temperature conditions [7–9, 28].

Residual stresses also influence the fabrication of overhangs. Overhangs and their defects were studied by Wang et al. [29, 30] who described the main challenges to their fabrication. The susceptibility to overhang defect formation is higher with increasing angle θ (Fig. 2-2). As a result of heat shrinkage, the tension forces are induced, which causes warping. The warping defect may accumulate until the unsupported part is elevated above the thickness of the layer. Then the exposed part is scanned by laser without powder and receives more energy, which can cause another deformation. In the worst case, the elevated surface may collide with the powder spreader and stop the fabrication run. Moreover, the heat dissipation of the overhang structure is limited during the fusion process because of the lower thermal conductivity of the unfused powder. The unfused powder act as an insulator with a lower thermal conductivity approximately 1-2 % of the bulk material [31]. Thus, the heat dissipation from overhang structures is lowered, which may result in large melt pool. In combination with gravity and capillarity forces, a larger melt pool may sink into supporting powder. Thus, decrease geometry accuracy and surface roughness. Therefore, the process parameters must be tuned to the lower energy input. Lower heat input can also prevent the adhesion of unfused powder particle to fused surfaces, which influences surface roughness.

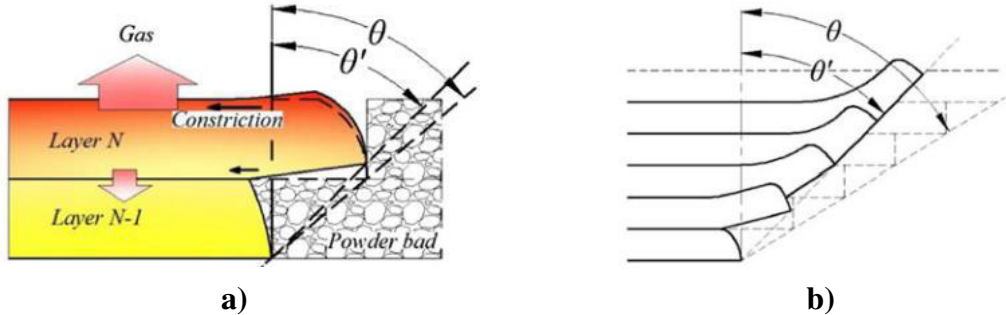


Fig. 2-2 a) warping principle; b) warping accumulation principle. [29]

Measurement of the residual stress can be divided into two main groups, nondestructive and destructive. Destructive distortion-based methods use the principle that residual stresses exist in the static equilibrium state and in any cut plane the sum of the residual stress normal to plane is zero [15]. When a new plane of the part is made, the stress must redistribute and deform the plane according to the magnitude of the residual stress. The newly deformed plane is measured and could be input into an analytical model or finite element model for residual stress calculation. The most used destructive techniques used in additive manufacturing are the hole drilling method, curvature, and contour method [32, 33]. Non-destructive diffraction techniques used in additive manufacturing are X-ray diffraction and neutron diffraction. Those techniques using Bragg's law to measure the lattice spacing and compare the results with unstrained parameters [15].

The most affecting element for the evolution of residual stress during the production run is the heat distribution in the processing part. Heat distribution can be affected by the setting of process parameters in the process that include laser-related process parameters, scanning strategy or powder bed preheating systems [34]. The powder bed preheating proved that it is an efficient technique for reducing residual stress in the process [8, 35]. The residual stresses can also be consequently eliminated after the production run by stress annealing [10], but cannot restrict the deformations and defects accrued during production. Thus, the fabricated part must be fixed on the platform directly or via support structures. Subsequently, the support structures increase the material consumption, prolong the fabrication time, and increase the postprocessing requirements.

2.3 Preheating in the Laser powder bed fusion

Preheating of the powder or part during the production run using laser powder bed fusion technology has a direct influence on the energy necessary to melt the metallic powder. The theoretical influence of the preheating can be expressed by eq. 2-1 [20]. For example, the energy necessary to melt stainless steel 316L preheated at 900 °C is 43 % lower compared to 80 °C [36].

$$Q = \rho c_p (T_l - T_0) + \rho L_f \quad (2-1)$$

where: Q	(J·m ⁻³)	is the energy necessary for melting the powder
ρ	(kg·m ⁻³)	- material density
c _p	(J·kg ⁻¹ ·K ⁻¹)	- specific heat
T _l	(K)	- melting temperature
T ₀	(K)	- initial temperature
L _f	(J·K ⁻¹)	- latent heat

The Eq. 2-1 can be estimated that the minimum energy for melting the 316L stainless steel is $8.46 \text{ J}\cdot\text{mm}^{-3}$ using preheating at $100 \text{ }^\circ\text{C}$. Nevertheless, the commonly used energy in LPBF is around $65 \text{ J}\cdot\text{mm}^{-3}$ estimated according to eq. 2-2. The difference between these values is caused by heat loss and reflection of the laser beam under real fabrication conditions [37].

$$E_o = \frac{LP}{LV \cdot HD \cdot LT} \tag{2-2}$$

- where: E_o ($\text{J}\cdot\text{mm}^{-3}$) is volumetric energy density
- LP (W) - laser power
- LV ($\text{mm}\cdot\text{s}^{-1}$) - laser velocity
- HD (mm) - distance between two neighbouring laser paths
- LT (mm) - powder layer thickness

Absorptivity of the laser beam is an important material characteristic which is influenced by the laser wavelength (Fig. 2-3a). The commonly used infrared lasers with a wavelength of around 1064 nm have good absorptivity on steel and nickel alloys, but, for example, absorptivity on copper, gold, and aluminium is less than 10% on the smooth surfaces. For that purpose green and blue lasers are now under development [38]. However, preheating has a decreasing effect on material reflectivity (Fig. 2-3b). Thus, it is a potential method that leads to the processing of a reflective material with infrared lasers.

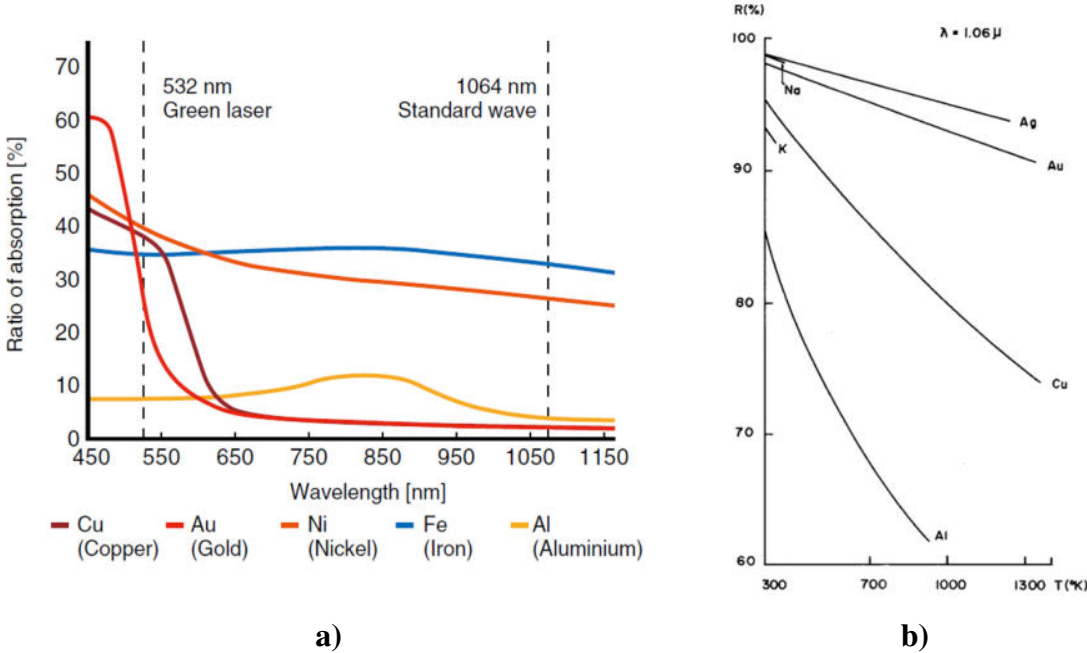


Fig. 2-3 a) influence of the absorption ratio on the laser wavelength [39]; b) influence of the temperature on the material reflectivity for 1064 nm wavelength [21].

Powder bed preheating in LPBF technology is in most cases realized using a preheated base plate [8, 40]. For preheating, resistive heating elements or induction coils are used. The preheating of the base plate has a disadvantage when high production runs are realized. The temperature of the top surface of the part gradually decreases during fabrication; thus, a non-consistent condition and differences in the microstructure were detected [41]. Thus, a different preheating system was developed and tested. The preheated base plate preheats the fabricated part and usually the new spread powder layer has a much lower temperature. Thus, the powder feedstock preheating device can decrease the temperature differences between the new and the already deposited powder layer [42]. The powder is preheated before it is spread on the manufactured part. For even more homogeneous conditions, the inertial atmosphere preheating device can be used [43]. The highest preheating temperatures were reached using an additional laser system which preheats the powder of the newly recoated layer before the laser scan the part. The preheat temperature in those cases can reach 2500 °C, which is suitable for the fabricating of ceramic materials without inner defects [44, 45]. The most efficient solution for homogeneous preheating is the combination of different types of preheating systems [46]. However, each material needs its individual preheating conditions to achieve an optimal result [47].

2.4 Influence of preheating on the selected materials processed using LPBF

The following text is divided into material groups for better readability. The aim is to define the influence of in-situ preheating on the properties of the fabricated material and to observe the suitable temperature ranges for group of materials.

2.4.1 Titanium alloys

The titanium alloys can be divided according to the occurrence of the material phases into α , β and $\alpha+\beta$ alloys. Ti6Al4V is the most widely used titanium alloy belonging to $\alpha+\beta$ group. In world production, it has 45% share among all titanium alloys. The ultimate and yield stress properties can reach after solution heat treatment to 970 MPa and 900 MPa, respectively. The elongation can reach 17 % [48]. The most common usage of this alloy is in the aviation, aerospace, automotive, and medical industries.

The observed microstructure of Ti6Al4V fabricated using LPBF was [49]:

- Bimodal (duplex) microstructure, composed of lamellar $\alpha+\beta$ colonies and interconnected equiaxed α prime phase
- Lamellar $\alpha+\beta$ structure, composed of α lamellae inside β grains

- Globular (equiaxed) microstructure, composed of globular primary α phase with β along the grain borders
- Acicular α' martensitic structure

The microstructure depends on the used process parameters. The microstructure most commonly observed in Ti6Al4V samples processed with LPBF is dominated by columnar grains and fine martensitic needles [50]. The martensitic evolution is caused by a rapid cooling rate of more than 410 K/s, and columnar grains were mostly observed in the building direction, which is the direction of heat dissipation. This microstructure type leads to high ultimate strength and low ductility. However, ductility can be further increased by using proper heat treatment.

In-situ base plate preheating was used for martensitic decomposition by Ali et al. [8]. Preheating at 570 °C led to α' martensitic decomposition to $\alpha+\beta$ structure which led to increased yield strength to 1176 MPa and elongation by 66 % compared to preheating at 100 °C (Fig. 2-4a). Furthermore, the preheating temperature higher than 570 °C led to a decrease in residual stress to zero (Fig. 2-4b). The martensitic decomposition was attributed to the decreased cooling rate after finalizing production run to 0.5 K/s, which is much lower than the cooling rate necessary for martensitic evolution. However, the preheating temperature higher than 570 °C did not lead to higher mechanical properties. Preheating at 670 °C caused a rapid decrease in elongation and preheating at 770 °C led to a rapid decrease in yield strength and the specimen failed during testing. The rapid decrease in mechanical properties in combination with high preheating temperatures was explained by inappropriate setting of process parameters. The process parameters did not change during production run and only the preheating temperature was increased, resulting in globularization of α phase and a different size of α lattices. Those microstructural changes caused weak spots and caused rapid specimen failure during testing (Fig. 2-4a).

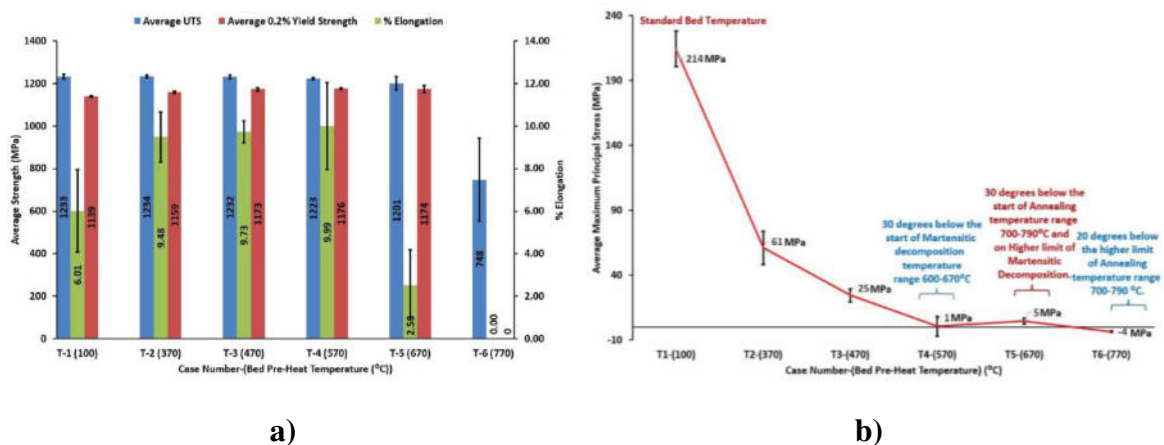


Fig. 2-4 The effect of powder bed preheating of LPBF processed Ti6Al4V; a) on the mechanical properties, b) on the residual stress. [8]

Xu et al. [51] studied parameters leading α' martensitic decomposition to $\alpha+\beta$ structure of Ti6Al4V. The tested were influence of dwell time (time between fusion of adjacent layers), diameter of the specimens, density of support structures, and layer thickness. It was found that for α' martensitic decomposition to $\alpha+\beta$ it is necessary to acquire sufficient time at the temperature of 600 to 850 °C. It was confirmed that the proper combination of parameters can lead to α' martensitic decomposition to $\alpha+\beta$ and control the size of lamellae structure on range of 1.15 to 0.8 μm . The highest effect from observed parameters had dwell time and layer thickness. Shorter time between scanning adjacent layers, higher layer thickness, lower support structures density, and larger specimen size lead to efficient α' martensitic decomposition.

Ali et al. [7] in his second research, which aimed at Ti6Al4V-ELI material, have studied the effect of scanning and remelting strategies on the evolution of residual stress. The compared scanning strategies were meander strategy with 45° and 90° rotation angle, and chessboard strategy with size of 5x5, 3x3, and 2x2 mm (Fig. 2-5). Furthermore, the 5x5 mm chessboard strategy was combined with rotation of 45° and 90° of the next chessboard field. The residual stress was measured using the hole-drilling method. The author also checked the combination of different scanning strategies with base plate preheating at 470 °C.

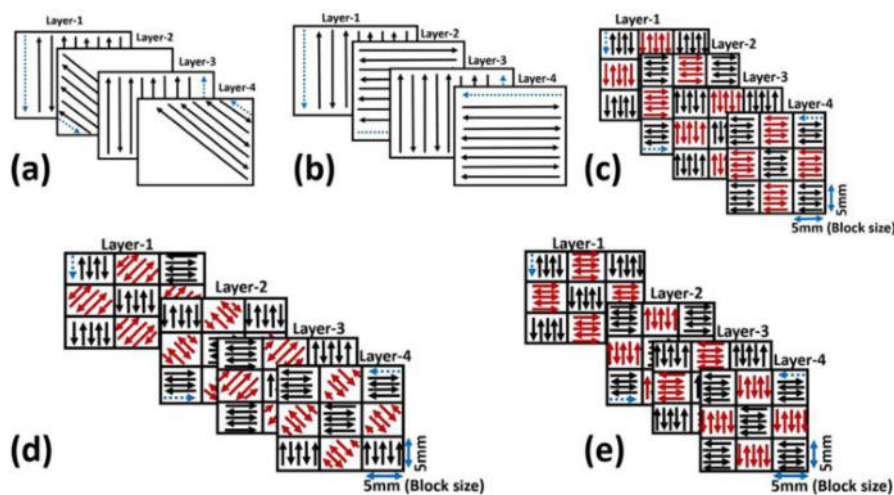


Fig. 2-5 The schema of scanning strategies used for assess the influence on the residual stress; a) meander with 45° rotation angle, b) meander with 90° rotation angle, c) chessboard scanning strategy, d) chessboard scanning strategy with 45° rotation angle , e) chessboard scanning strategy with 90° rotation angle. [7]

The lowest residual stress was measured using the meander scanning strategy with 90° rotation angle in the following layer, Fig. 2-6a. The chessboard strategy showed that an increased field length leads to higher residual stress, because of an increased delay time between adjacent trajectories; thus, a higher temperature difference Fig. 2-6b. The type of scanning strategy did not have an effect on the mechanical properties and a clear effect on the relative density.

Preheating at 470 °C led to a decrease in residual stress by 37.6 % on the specimen produced with the meander scanning strategy with rotation angle of 90° and by 44.1 % on the specimen with chessboard 5x5 mm scanning strategy compared to preheating at 100 °C.

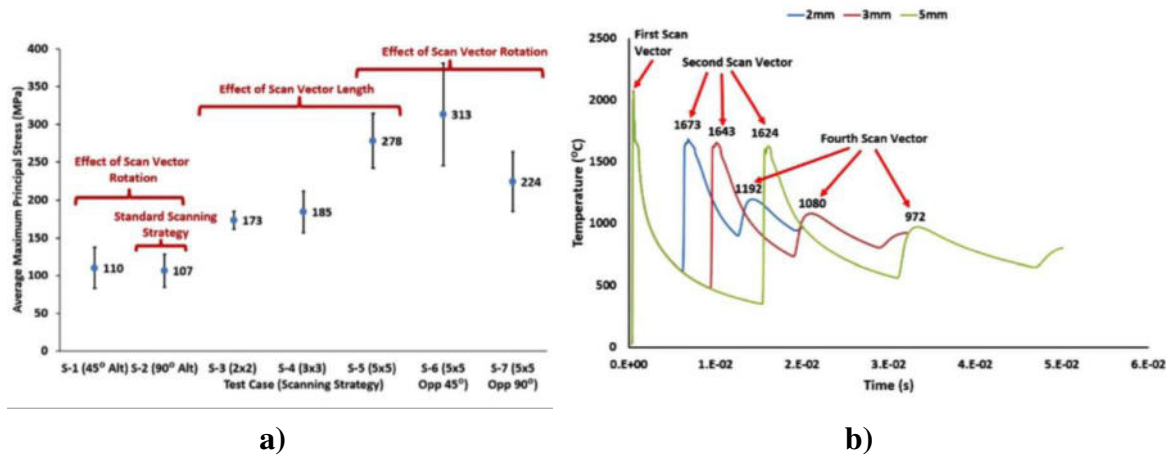


Fig. 2-6 a) The effect of scanning strategy of LPBF processed Ti6Al4V on the residual stress; b) the effect of the chessboard scanning strategy vector length on the temperature and cooling rate. [7]

Ali et al. also tested different remelting strategies and their influence on residual stress. The remelting strategy using the energy density increased to 150 % against process parameters, resulting in a 33.6 % reduction of the residual stress. Nevertheless, it had a negative impact on the mechanical properties probably due to increased oxidation. Remelting with a different energy density did not further decrease residual stress. For example, remelting with 50% energy density led to an increase of elongation but also an increase of porosity by 2.4 % and residual stress by 68.2 %. Therefore, the author does not recommend remelting strategies for the Ti6Al4V titanium alloy.

The residual stress of Ti6Al4V can be influenced by the setting of process parameters [28]. Longer exposition times, which is equivalent to laser velocity of lasers working in continuous mode, and lower laser power with persisted energy density led to a lower residual stress. This was due to lower cooling rate, thus, lower temperature gradients. Variation in laser-related process parameters did not lead to different ductility of Ti6Al4V, but the yield strength increased with higher exposition times and lower laser power. The higher layer thickness led to a lower residual stress as a result of the decreased cooling rate.

2.4.2 Intermetallic alloys

The preheating in LPBF was also studied on specimens fabricated from intermetallic alloys. Intermetallic alloys are usually composed of two main elements, creating intermetallic phases and alloying elements for desired phase stabilization. Intermetallic alloys exhibit physical properties very different from conventional alloys, for example, superconductivity, shape memory effect, high strength, stiffness creep, and corrosion resistance at elevated temperatures. Traditionally, intermetallic alloys were fabricated using casting, forging, hot extrusion, powder metallurgy, and rolling methods. Nevertheless, even for those methods, the production is a challenging process. Additive manufacturing offers a new possibility to produce intermetallic alloys in a near net shape. However, some challenges related to low ductility, low fracture toughness, high residual stresses, loss of alloy content, pores, and cracks must be overcome [52]. Powder bed preheating was proposed as a potential technique to mitigate some negative effects related to the evolution of residual stresses.

Shishkovsky et al. [53] studied the effect of preheating up to 500 °C on the shape memory alloy NiTi, which is composed of 45 wt. % of titanium and 55 wt. % of nickel. The highest relative density of 97.1 % was reached in combination with preheating to 500 °C. Specimens preheated at temperatures lower than 300 °C had an inconsistent weld tracks and cracks inside the material were observed.

The γ -TiAl's are used due to their high strength in high-temperature conditions up to 900 °C for aerospace components. In the early stages, LPBF processed γ -TiAl's had low relative density of 97 % and contained many defects such as cracks and unmolten powder [54]. The cracking can be suppressed by powder bed preheating. Preheating at 200 °C decreased, but did not completely eliminate the amount and length of cracks of the Ti₄₇Al₂Cr₂Nb alloy [55]. The relative density of the specimens reached 98.95 % using 300 W laser power and laser velocity of 30-50 mm/s. Doubenskaia et al. [56] applied preheating at 450 °C, nevertheless, reached a low maximum relative density of 93±2 % and specimens contained cracks. Furthermore, they detected evaporation of the Al constituent while using an elevated laser energy input.

Gussone et al. [37] processed Ti45Al2Cr2Nb γ -TiAl alloy using LPBF technology in combination with base plate preheating at 800 and 1000 °C. A wide range of process parameters was tested in an energy density range of 50-300 J/mm³. The higher energy density led to a decrease in the amount of Al content in the alloy, probably as a result of overheating. The clear effect of preheating temperature on the Al content was not detected (Fig. 2-7a). The energy density had a significant effect on the resulting microstructure (Fig. 2-7b), which is due to the loss of Al and the increased cooling rate of higher energy densities. XRD phase analysis showed that an energy density of 300 J/mm³ led to dominant peaks of β /B2 phase compared to 60 J/mm³ where was predominant γ and α_2 phase (Fig. 2-7c). The preheating did not have a significant influence on the detected phases. Despite the wide variety of tested process parameters and high-temperature preheating, cracks were always detected in specimens. Gussone attributed these cracks to a fast cooling rate and recommends a cooling rate lower than 10 K/min.

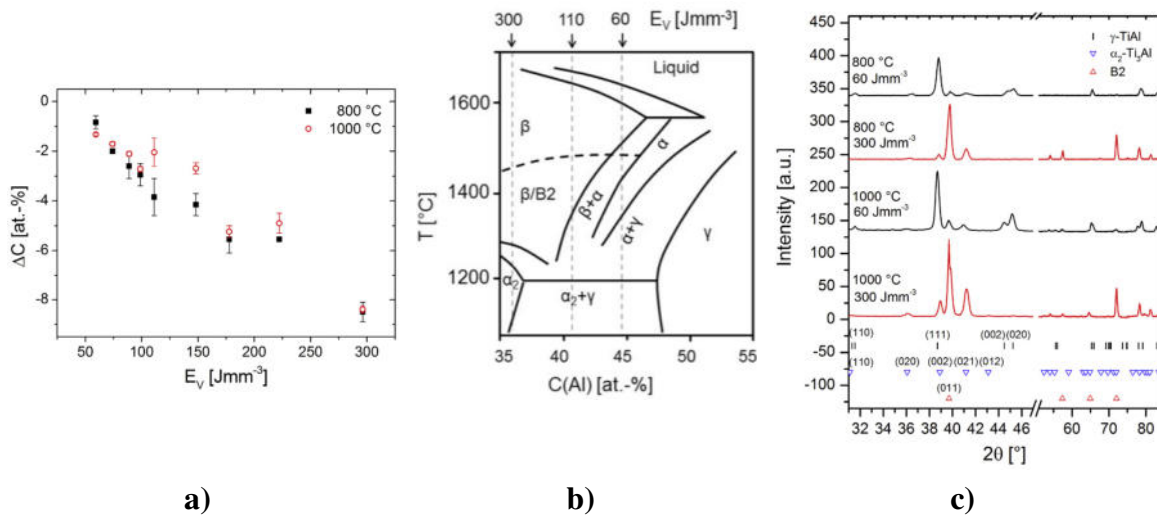


Fig. 2-7 a) Change of Al content as a function of energy density and preheating temperature; b) Quasi-binary Ti-Al phase diagram; c) XRD spectra for LPBF Ti45Al2Cr2Nb alloy processed at different energy density and preheating temperatures. [37]

Polozov et al. [57] were able to produce a fully dense Ti45Al2Cr2Nb γ -TiAl alloy using LPBF without cracks. Cracking was gradually eliminated as the preheating temperature increased (Fig. 2-8a-c). Specimen without cracks was preheated at 900 °C. A lower preheating temperature was not sufficient for brittle-ductile transition of the γ -TiAl, which is around 750-780 °C [58]. Preheating to 900 °C caused that the fabricated specimens stayed longer in the ductile zone and relieved any internal residual stresses and also slowed the cooling speed [52]. However, an increased number of spherical pores was observed when preheating at 900 °C was applied. The relative density measured in the specimens was higher than 99.8 % (Fig. 2-8d).

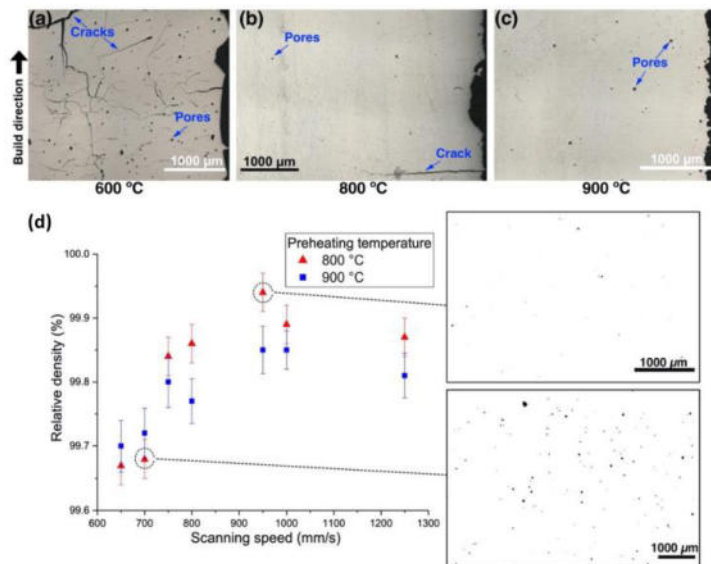
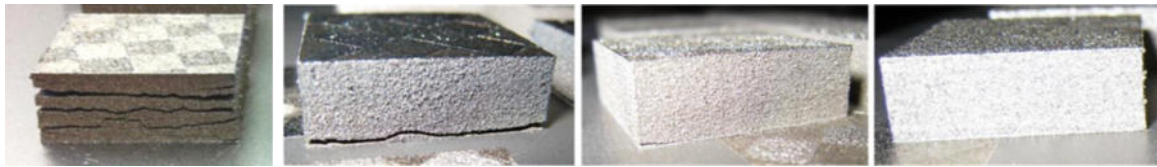


Fig. 2-8 Ti48Al2Cr2Nb processed using LPBF a-c) cross section image of specimen produced under different preheating temperatures d) influence of scanning speed and preheating temperature on the relative density. [57]

2.4.3 Steels

The production of a near net shape component is tempting especially for materials with high hardness and wear resistance. However, these material properties are usually associated with low ductility. In combination with rapid cooling rates and residual stress typical for the LPBF technology, crack formation and delamination of the material from the base plate cause problems. Typically, tool steels with a high carbon content are nearly impossible to produce without cracks using LPBF technology without using some method that restricts residual stresses. Many authors tested preheating to reduce temperature gradients, but using proper setting of laser-related process parameters can also lead to reduction of residual stresses. Thus, it also reduces the amount of cracks [59].

Kempen et al. [40] used base plate preheating up to 200 °C to fabricate M2 HSS steel without cracks. M2 HSS belongs to the group of tool steels that maintain its hardness even at high temperatures. The high hardness value is caused by the martensite crystalline structure. Kempen fabricated specimens without preheating and with preheating at 90, 150, and 200 °C. Specimens with visible macrocracks were reached with preheating at 200 °C (Fig. 2-9).



a) **b)** **c)** **d)**

Fig. 2-9 M2 HSS tool steel processed using LPBF in combination with base-plate preheating a) Without preheating; b) Preheating at 90 °C; c) Preheating at 150 °C; d) Preheating at 200 °C. [40]

Moreover, Kempen demonstrated that with applied base-plate preheating as another energy source can be reached higher relative density with the same laser velocity and lower top surface roughness (Fig. 2-10). The same effect also had remelting technique, but in comparison with preheating, the remelting prolongs the build time and the build cost. Furthermore, the remelting led to the production of more cracks caused by the higher temperature accumulated in the specimens, thus increasing the cooling rate, resulting in a more brittle martensite phase.

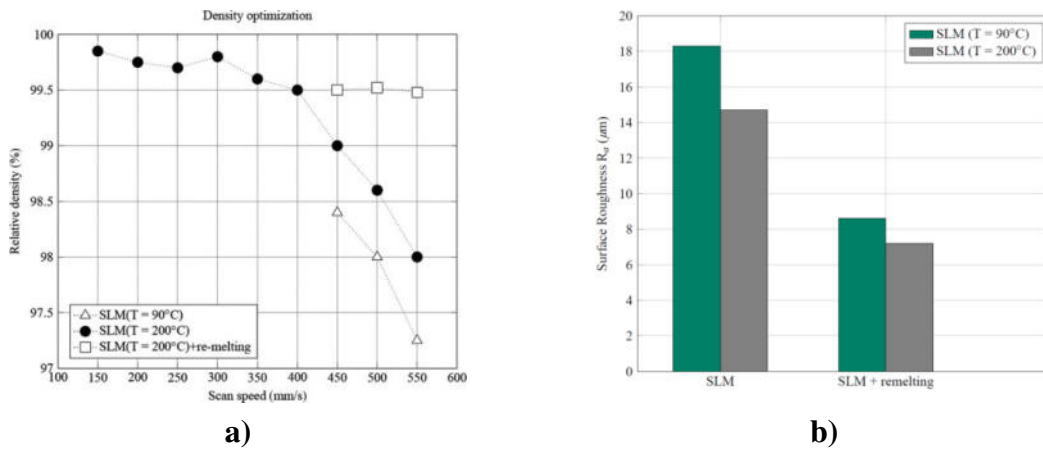


Fig. 2-10 M2 HSS tool steel processed using LPBF in combination with base-plate preheating a) the effect on relative density; b) the effect on top surface roughness. [40]

Yadroitsev et al. [36] investigated the effect of preheating and laser velocity on geometric and microstructure properties on single tracks produced from 316L stainless steel. For preheating, they used an infrared heater capable of preheating the build platform at 80, 30, 500, 700 and 900 °C. The laser velocity tested in the range of 80-2800 mm/s showed that the higher values than 2400 mm/s resulted in inconsistent weld tracks. Inconsistent weld tracks were also observed with preheating higher than 700 °C. Both cases led to the balling effect. Weld track instability under preheating higher than half of the material melting temperature was due to the sintering process of the unfused powder particles, thus changing its properties of density and temperature conductivity. The laser velocity showed that it is a flexible process parameter for changing melt pool width w_2 , depth h_2 , and weld track width w_1 (Fig. 2-11). The preheating temperature mainly controlled the wetting angle α , melt pool depth h_2 and the height of the weld track h_1 .

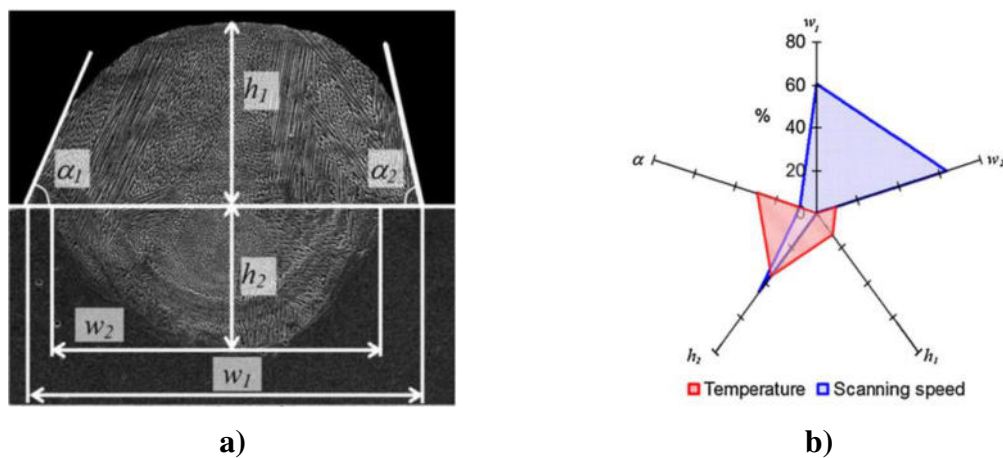
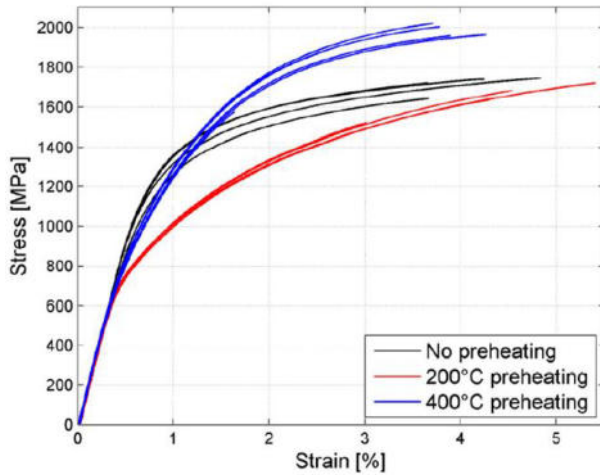
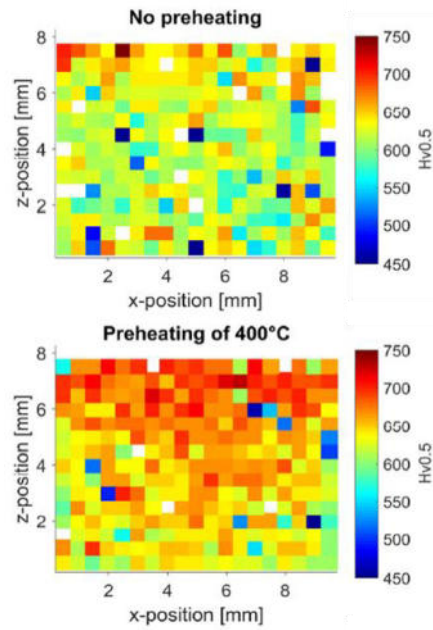


Fig. 2-11 Influence of preheating temperature and laser velocity on weld track geometrical properties made of 316L a) weld track cross-section; b) graphical representation. [36]

Mertens et al. [60] studied the change in mechanical properties of H13 tool steel as a function of the preheating temperature up to 400 °C. The residual stress in the top specimen surface changed from compressive of -324 MPa to tensile of 371 MPa as the preheating temperature increased from 20 to 400 °C. The preheating also had an effect on the microstructure. The fine bainitic microstructure observed at preheating at 400 °C was more homogeneous, leading to better mechanical properties (Fig. 2-12a). The measured ultimate strength reached 1965 ± 145 MPa at the preheating temperature of 400 °C while in the specimen without preheating it was just 1712 ± 103 MPa. The conventional ultimate strength of H13 tool steel is 1990 MPa. The preheating also had an effect on the hardness where higher preheating led to a higher overall hardness of 650-700 HV (Fig. 2-12b).



a)



b)

Fig. 2-12 Influence of preheating temperature on properties of H13 tool steel on: a) mechanical properties; b) Vickers microhardness measured on cross-sectioned specimens. [60]

Krell et al. [61] also processed H13 tool steel (X40CrMoV5-1) using LPBF. The proper combination of process parameters in combination with preheating temperatures was investigated. Moreover, the powder reusability was assessed. The preheating temperature was used up to 300 °C according to the martensite start temperature at 285 °C.

The appropriate combination of process parameters was found to reach the relative density of 99.95 % and in the combination with preheating at 300 °C the cracking was eliminated (Fig. 2-13a). The elimination of cracks was explained as a result of temperature gradient reduction, lower elastic modulus, and yield strength, which led to residual stress relaxation in the plastic flow of the material. The oxygen content increased as higher preheating temperatures were used. Furthermore, oxygen content uptake was also confirmed in densified specimens (Fig. 2-13b).

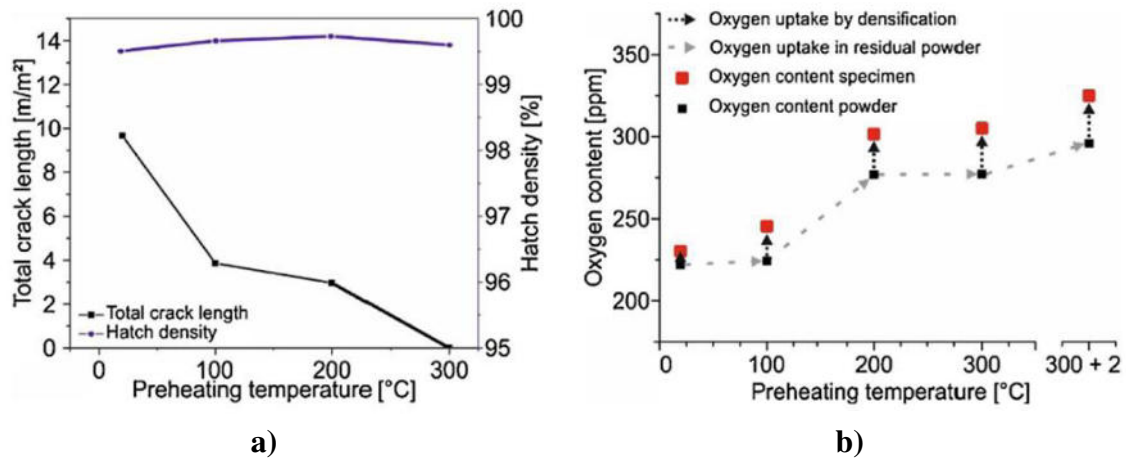


Fig. 2-13 Influence of preheating temperature on properties of H13 tool steel on: a) relative density and crack length; b) unfused powder oxidation and solidified material oxygen uptake. [61]

Many other studies confirmed that preheating is necessary for producing hard-to-weld tool alloys with an increased amount of carbon, which gives them their excellent mechanical properties. Boes et al. [62] was able to reduce the crack density of X65MoCrWV3-2 to $0.41 \cdot 10^{-4} \mu\text{m}^{-1}$ processed with preheating at 300 °C. As reported, lower preheating temperatures were not able to be used due to cracks. The reduction in crack density was explained as a consequence of preheating at a higher temperature than the martensite start 226.3 °C, which increased the ductility of the alloy. This technique is also used for welding martensitic alloys. Jochen et al. [6] processed Cr-Mo-V (W360 AMPO) martensitic tool steel by LPBF in combination with preheating at 300-450 °C. The result was a homogeneous material with bainitic microstructure with a hardness of 52-55 HRC. Higher preheating temperatures led to an increase in the amount of oxygen in fused specimens. Specimens fabricated without preheating had a martensitic microstructure with austenite.

2.4.4 Nickel-based alloys

Nickel-based alloys possess excellent oxidation resistance and creep properties at high temperatures and are used in the energy and aerospace industry. The traditional process for near net shape fabrication is casting. However, LPBF offers higher shape complexity [63]. The most widely used nickel-based alloy in LPBF is Inconel 718 (IN718), which is suitable for application up to 650 °C [64]. For applications at higher temperature, a different alloy must be used. For example, Inconel 939 (IN939), which is due to its high-chromium content and strengthening by gamma prime (γ' – Ni₃(Al, Ti, Nb)) precipitates and carbides capable of being used for a long time at temperatures up to 850 °C [65]. The limitation of the processing of nickel-based alloys by LPBF is the formation of cracks. This is a function of the aluminium and titanium content associated with the formation of γ' precipitations (Fig. 2-14a) [66].

Hagedorn et al. [67] processes nickel-based superalloy MAR M-247 by LPBF a with relative density higher than 98 %. MAR M-247 is classified as a difficult to weld alloy due to its excessive crack formation. The cracks were eliminated with applied preheating at 1200 °C and laser power 100 W, laser velocity 200 mm/s and hatch distance 0.08 mm. The resulting microstructure was composed of cubic γ' precipitates and carbides, giving this alloy excellent creep resistance (Fig. 2-14b). Thus, preheating gives the possibility to process nickel-based alloys susceptible to cracking by LPBF.

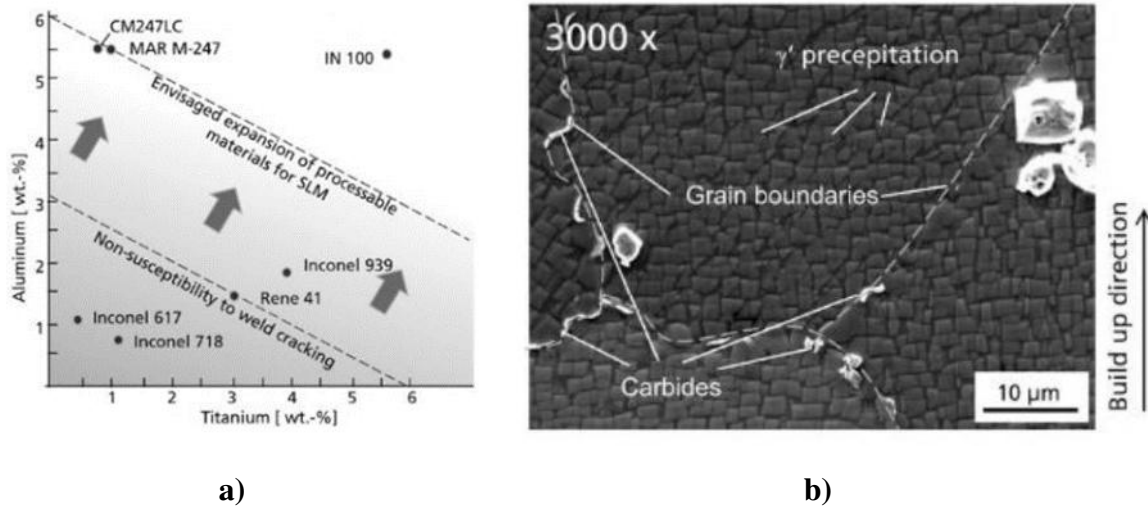


Fig. 2-14 a) Classification of nickel-based superalloys based on susceptibility to weld cracking as a function of aluminium and titanium content [66].; b) SEM image of microstructure of MAR M-247 alloy produced without cracks with applied preheating at 1200 °C [67].

Park et al. [68] studied IN718 under preheating at 50, 100, and 150 °C and varied laser-related process parameters to reach fully dense specimens. The fully homogeneous samples had 99.9% of relative density despite the change of preheating. The highest porosity of 0.018% was observed at preheating at 50 °C. The pores had a spherical shape and a size up to 20 μm . Higher preheating temperatures of 100 and 150 °C led to decrease in porosity to 0.011% and 0.008%, respectively. Thus, created a better condition for melting the powder. Preheating in the range of 50-150 °C had almost no influence on the tensile properties and hardness. The yield strength at 50, 100 and 150 °C was 681 ± 11.3 MPa, 679 ± 7.8 MPa and 687 ± 0.7 MPa. Elongation reached values of 28%, $27.5 \pm 0.7\%$ and $27.5 \pm 0.7\%$ (Fig. 2-15a). The hardness values at preheating at 50, 100 and 150 °C was 310.8 ± 8.9 HV, 312.3 ± 9.1 HV and 314.9 ± 11.3 HV (Fig. 2-15b). The residual stress measured using the XRD method on the cross-sections of cubic specimens was highest in σ_z direction (building direction) with preheating at 50 °C (Fig. 2-15c). The value of the σ_z residual stress gradually decreased from 422 MPa to 332 MPa as the preheating temperature increased from 50 to 150 °C. The preheating temperature had no effect on σ_x residual stresses.

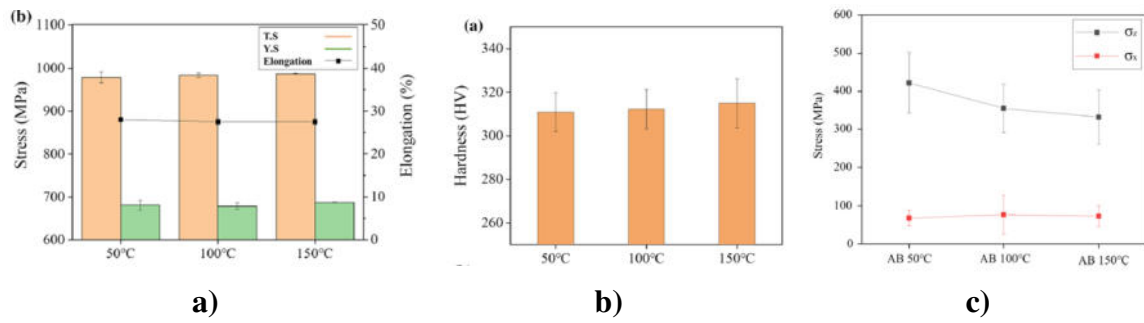


Fig. 2-15 Effect of preheating temperature of 50, 100 and 150 °C on IN718; a) mechanical properties; b) micro hardness; c) residual stresses. [68]

The observed microstructure was composed of a dendritic structure developed toward the centre of the melt pool as a consequence of faster solidification of the melt pool boundary and temperature differences (Fig. 2-16). The result of the higher preheating temperature is an increase in the inner-dendritic spacing and the width of the precipitates. The inner-dendritic spacing was measured at 0.48 ± 0.01 , 0.52 ± 0.12 and 0.59 ± 0.11 μm as the preheating temperature changed from 50 to 150 °C. The width of the precipitates was consequently 0.16 ± 0.04 , 0.20 ± 0.03 and 0.23 ± 0.04 μm . The precipitates occur as a result of a high and nonequilibrium cooling speed, which leads to a nonhomogeneous concentration of alloying elements. That leads to micro-segregation and precipitate formation. The precipitates in IN718 are composed of Nb, Mo, and C.

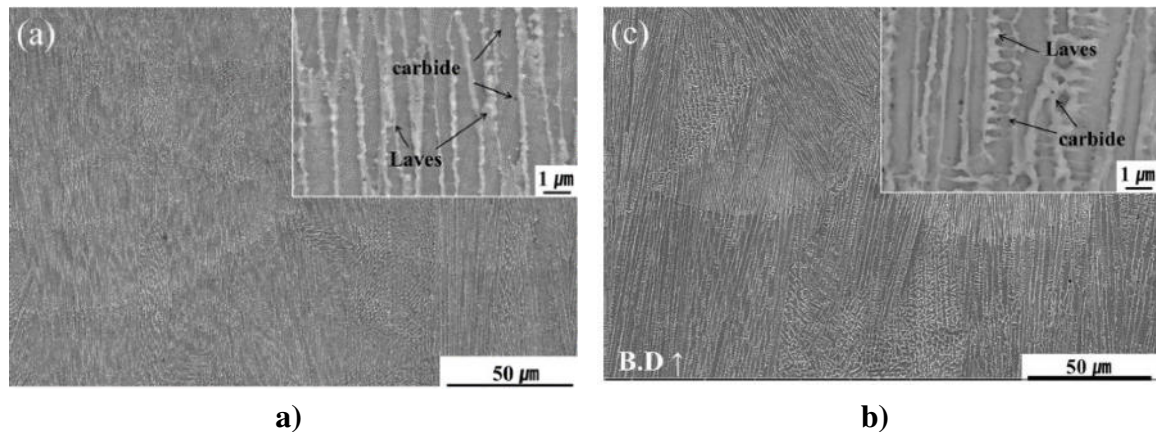


Fig. 2-16 Effect of preheating temperature of 50 and 150 °C on microstructure of IN718; a) preheating at 50 °C; b) preheating at 150 °C. [68]

IN718 and the effect of the powder bed preheating on the residual stresses was studied by Mirkoohi et al. [69]. Within his study, an analytical model was created and validated to predict residual stresses. The model calculates the temperature field and predicts residual stress. The temperature field is calculated using moving heat source which considers the heat losses, multilayer and multiscan aspects, temperature-dependent material properties, latent heat of fusion and preheating. Preheating can effectively reduce residual stress, which was up to temperatures of 100 °C validated by XRD analysis on fabricated specimens (Fig. 2-17). The predicted and measured data were in good agreement.

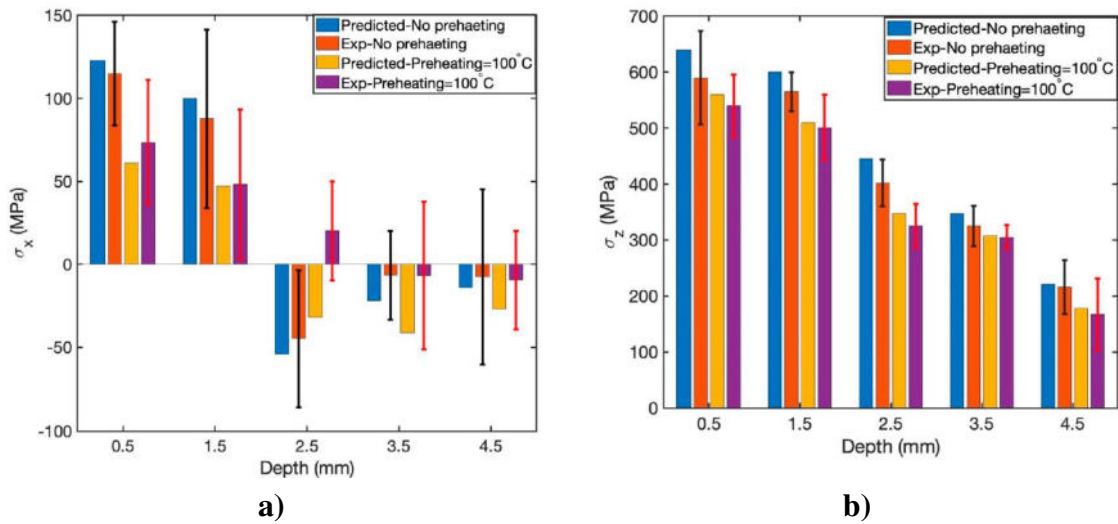


Fig. 2-17 Validation of analytical model for predicting the residual stresses of IN718; a) σ_x direction; b) σ_z direction (build direction) [69]

However, according to this analytical model, excessive preheating can even increase residual stresses Fig. 2-18. According to the author, excessive preheating can lead to heat accumulation and grain coarsening in the melt zone and heat affected zone, which can reduce yield strength.

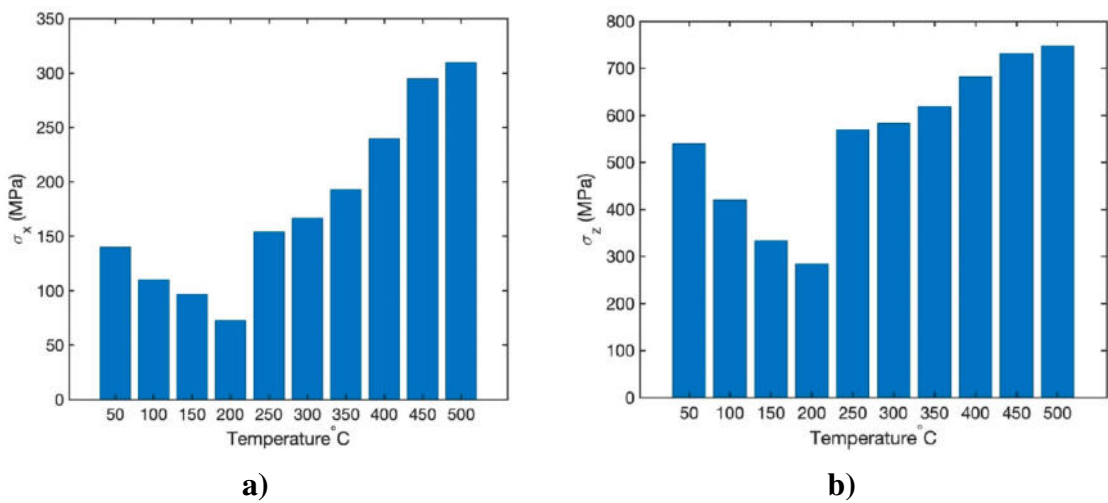


Fig. 2-18 Effect of preheating on residual stress of IN718 prediction of analytical model; a) σ_x direction; b) σ_z direction (build direction) [69]

2.4.5 Aluminium alloys

The most widely used aluminium alloy in the LPBF is AlSi10Mg. The effect of preheating on distortions and residual stresses in this alloy was studied by Buchbinder et al. [35] who fabricated cantilever geometry at preheating temperatures of 100-250 °C. The sides of the cantilevers were cut in as built state and the distortion value was measured. The distortions are caused by residual stresses; therefore, this method is suitable for fast comparison of process parameters. The preheating had a significant effect on the distortions. As the preheating temperature increased, the distortions gradually decreased until preheating at 150 °C. Preheating at 200 and 250 °C caused elimination of distortions (Fig. 2-19a). However, the preheating temperature higher than 150 °C led to a rapid decrease of microhardness due to grain coarsening (Fig. 2-19b).

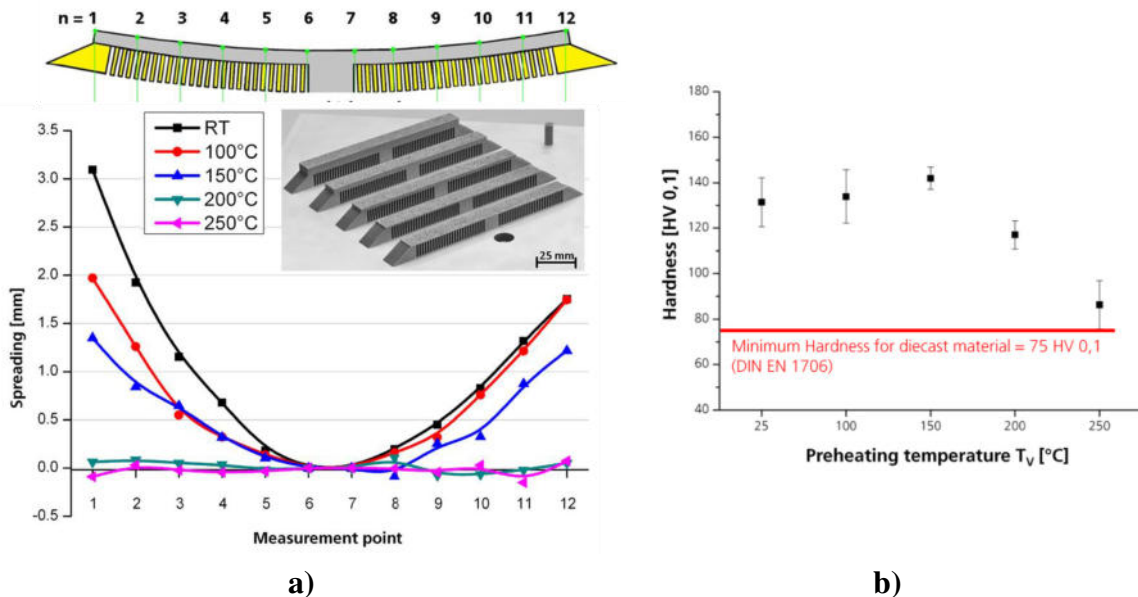


Fig. 2-19 Effect of preheating on AlSi10Mg: a) distortions of cut specimens; b) microhardness. [35]

AlSi10Mg is a die casting alloy that belongs to Al-Si base alloys that predominate in the LPBF process due to its relatively easy processing behavior. This is due to the small difference between the melting and solidifications temperature. The exhibit good mechanical properties. However, for application up to 300 °C, the Al-Cu alloy EN AW 2618 is better choice. This alloy is classifies as hard to weld and was studied Koutný et al. [70]. The author studied the influence of the laser-related process parameters, scanning strategy, support structures and preheating on densification behaviour and crack formation. Within this study, no crack-free specimen was created even with applied preheating. Nevertheless, it was found that the chessboard scanning strategy and the application of support structures can significantly influence the heat distribution and decrease the amount of cracks. Furthermore, preheating at 400 °C in combination with the chessboard strategy can nearly eliminate cracks. However, preheating increased the amount of spherical pores inside the samples probably due to excessive heat input from a laser source.

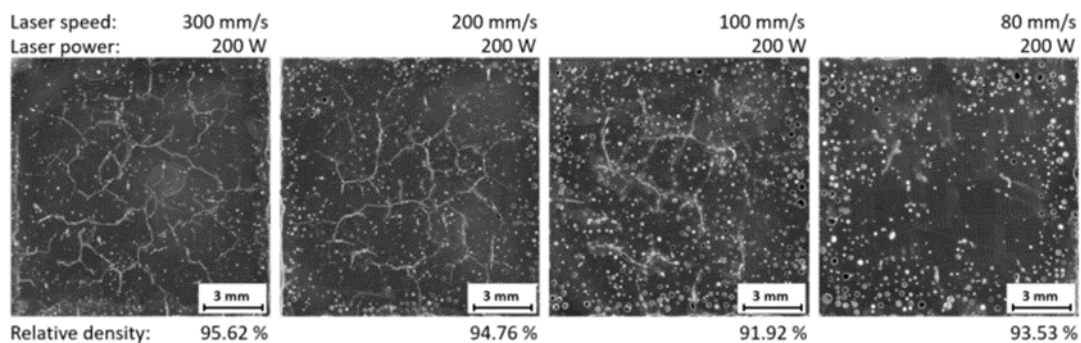


Fig. 2-20 EN AW 2618 processed by LPBF with preheating at 400 °C. Specimens with chessboard scanning strategy and gradually decreasing laser velocity. [70]

EN AW 6000 and 7000 groups of aluminium alloys are highly demanding alloys for processing by LPBF due to their high strength. However, they are also hard to weld alloys and suffer from crack formation. Syed et al. [71] processed the crack-free EN AW 6061 alloy by LPBF in combination with preheating at 500 °C (Fig. 2-21). The maximum measured relative density of 98.7 % was measured in the preheated specimen. In general, the relative density of the preheated specimens was higher. Mechanical properties and hardness compared in as built and T6 heat treated state reached values of the wrought material.

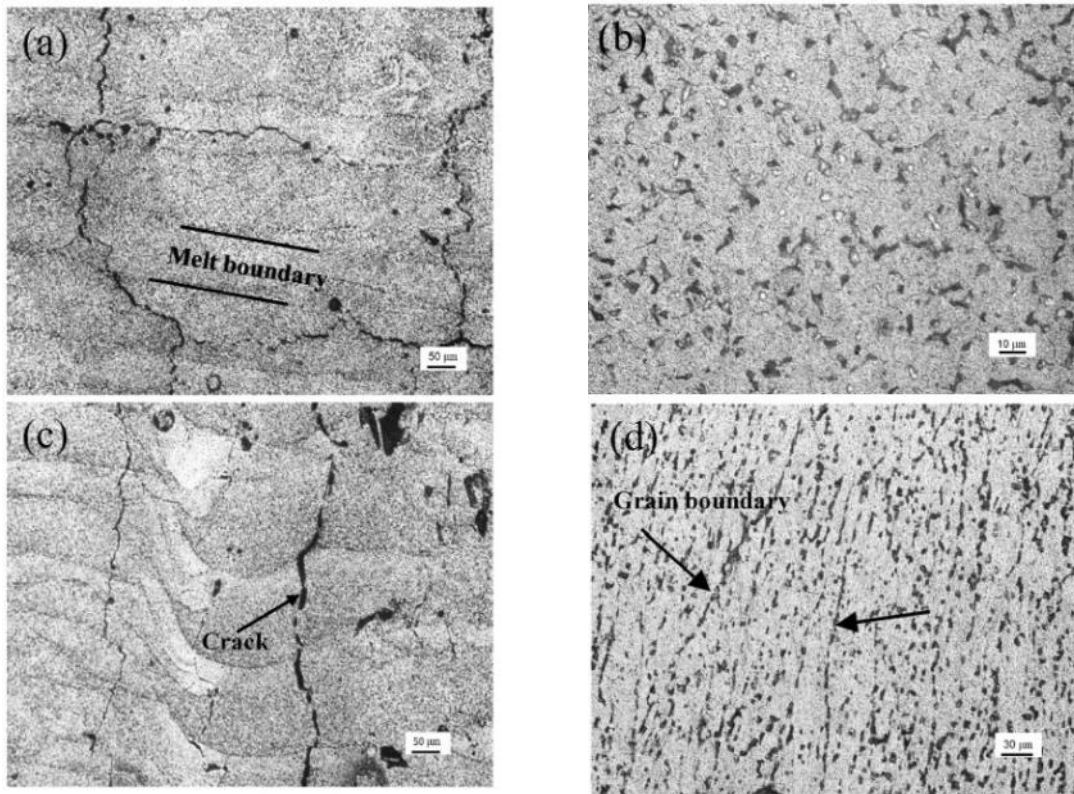


Fig. 2-21 Cross-section LOM images of EN AW 6061 alloy; a) non-preheated specimen, XY section; b) non-preheated specimen, XZ section (building direction); c) preheated specimen at 500 °C, XY section; d) preheated specimen at 500 °C, XZ section. [71]

Vora et al. [72, 73] used a different approach to the use of preheating in LPBF technology. The main idea was to eliminate residual stresses by preheating for the elimination of the needed support structures. For his research, two powders of Al-Mg and Si-Cu-Ni alloys were used, which in-situ fabrication were solidified in Al339 eutectic alloy. In combination with preheating, the author was able to solidify material to relative density of 98%. In addition, the specimens with overhang of 10 mm and deformation of 0.1 mm without support structures were fabricated (Fig. 2-22).

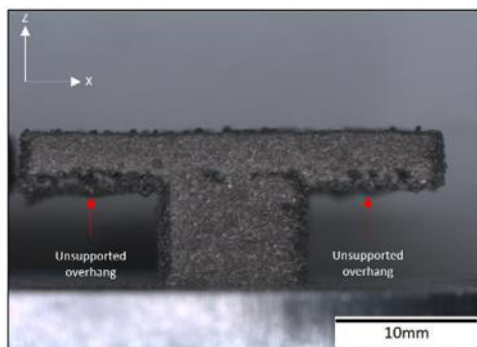


Fig. 2-22 Test specimen in-situ fused to Al339 alloy from a blend of two alloys fabricated at preheating of 380 °C with 10 mm overhang. [72]

2.4.6 Copper

Copper exhibits excellent thermal and electrical conductivity. Moreover, copper has antibacterial, catalyst effect, and excellent corrosion resistance. Thus, it is desired material for heat exchangers, electric applications, and other applications [74]. The high shape complexity of LPBF allows us to fabricate thin-wall structures with better resolution in comparison with EBM. Thus, the production of copper parts using LPBF may lead to more effective components with complex geometry, for example coolers, which can increase the performance of our machines [75]. However, the fabrication by LPBF must overcome the issues connected with low laser energy absorptivity of lasers with wavelength 1000-1100 nm, high thermal conductivity, and oxygen affinity [76–79]. These issues researchers tried to overcome by using high-powerful infrared lasers with power up to 1 kW, alloying or adding elements into pure copper, using preheating to low temperatures, and by using lasers with wavelength with better absorptivity [80].

Lykov et al. [81] in 2015 studied processing of pure copper using LPBF equipped with a 200 W CO₂ laser. The specimen with the highest relative density of 88.1 % was fabricated with maximum reachable 200 W of laser power and relatively slow laser velocity of 100 mm/s. Kaden et al. [82] used a pulse laser with a wavelength of 1030 nm to produce compact but porous structures of pure copper. The compactness was acquired by complete fusion of particular powder grains (Fig. 2-23).

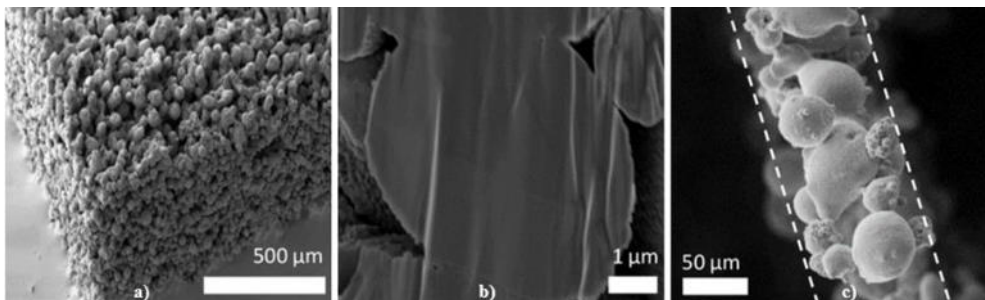


Fig. 2-23 Pure copper produced using LPBF. [82]

Trevistan et al. [83] used for copper processing fiber laser with wavelength of 1000 nm with maximum power of 200 W. To eliminate the issue with low relative density, the authors tried to use a preheating of 100 °C. The preheating temperature decreases the thermal conductivity of copper [84], thus, has ability to affect its solidification. Nevertheless, the maximum relative density was only 83 % using the following process parameters: 195 W, 400 mm/s and hatch distance 0.08 mm. The specimens were composed of lack of fusion defects and cracks (Fig. 2-24).

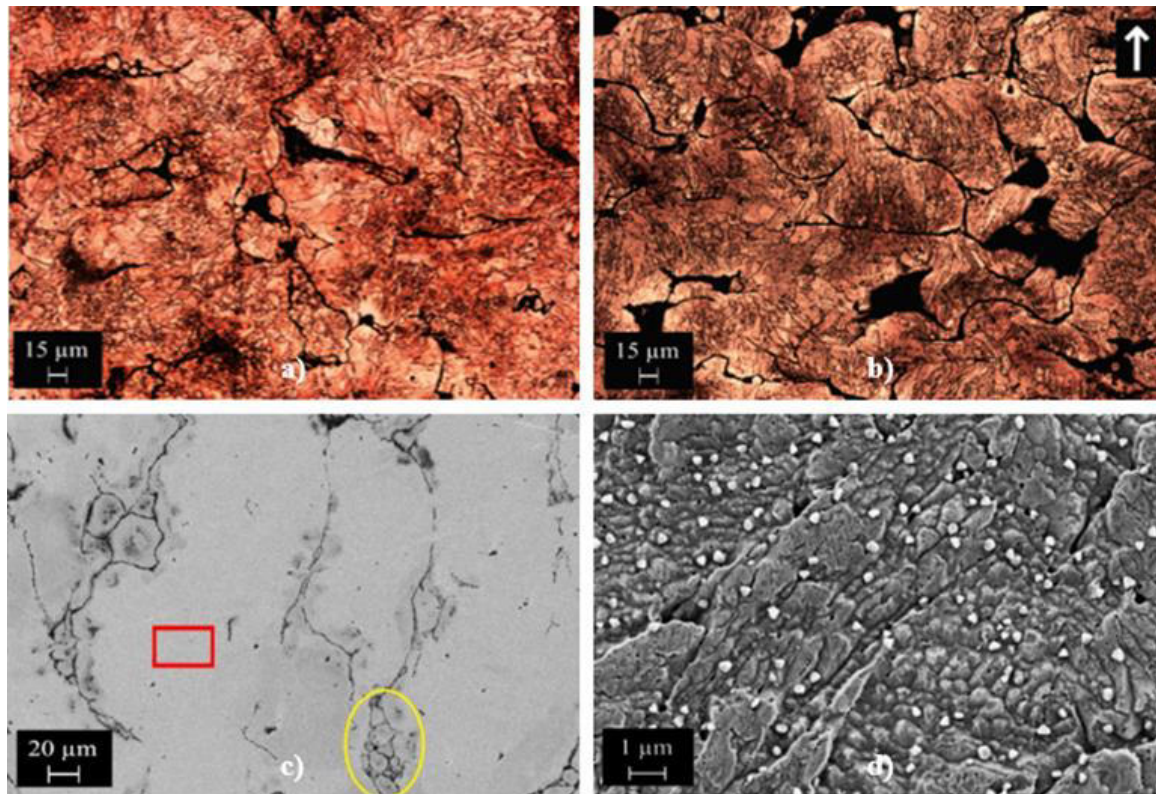


Fig. 2-24 Copper produced using LPBF in combination with preheating at 100 °C. [83]

Ikeshoji et al. [85] in 2017 used for pure copper processing fibre laser with a maximum power of 800 W and reached a relative density of 96.9 %. The main aim was to find an optimal hatch distance, which will lead to a higher relative density. From range of 0.025-0.12 mm, the optimum hatch distance is 0.1 mm in combination with laser velocity of 300 mm/s.

Colopi et al. [86] mentioned that for stable the melting process of copper, it was necessary to use a high-powerful fibre laser for sufficient power delivery. Thus, the authors used a 1 kW 1070 nm fibre laser with spot diameter of 78 μm . The authors defined the process parameter range leading to a stable process and relatively homogeneous samples. The maximum relative density reached was 97.8 % (Fig. 2-25a). However, the specimens were more homogeneous in the centre and the surfaces that were adjacent to the free unfused powder were highly porous (Fig. 2-25b). The authors contribute this to the high thermal conductivity of copper, which affects the heat distribution in the specimens, leading to heat accumulation in the centre of the specimen and fast cooling of the sides. Thus, there is insufficient energy on the sides for stable melting process.

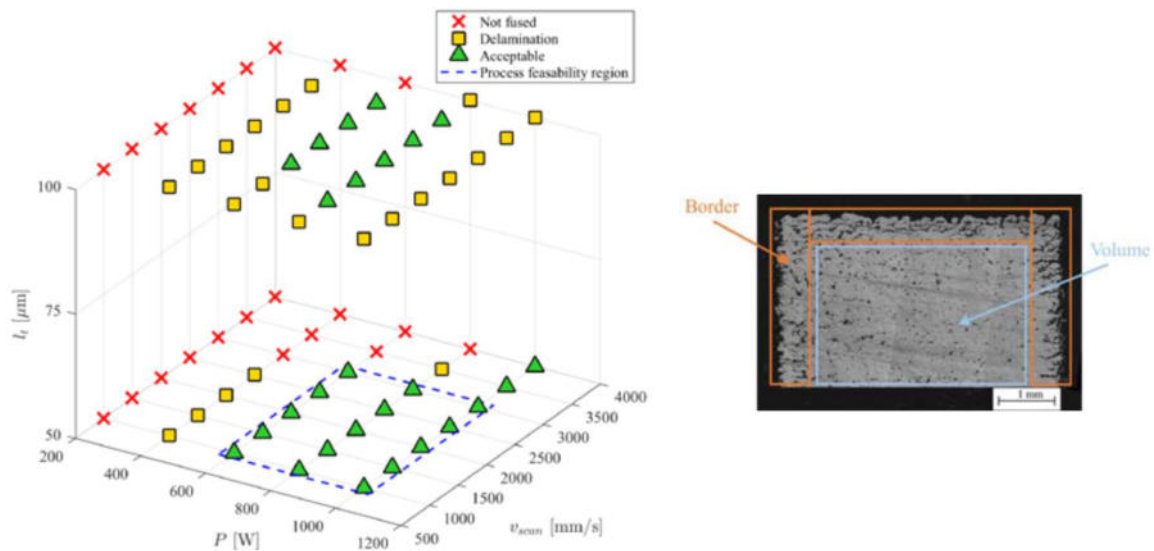
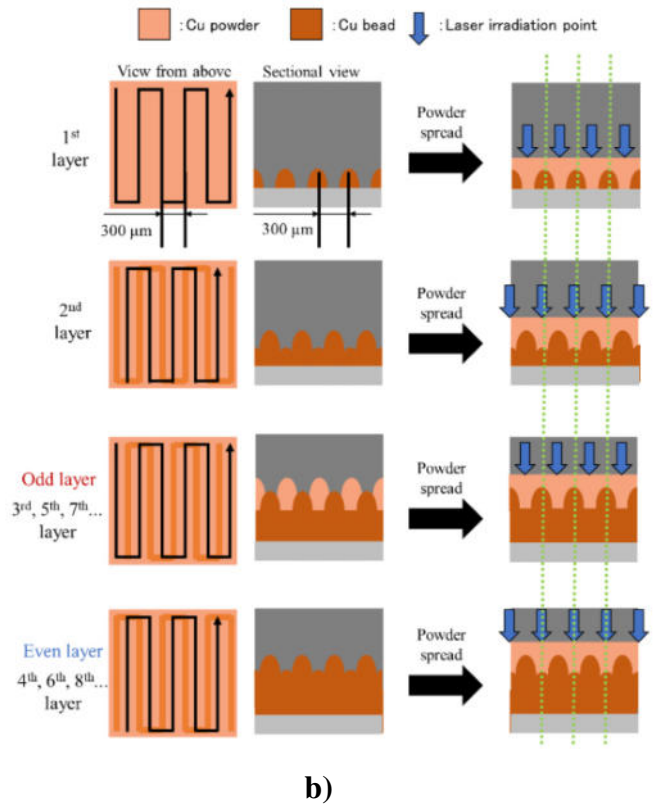
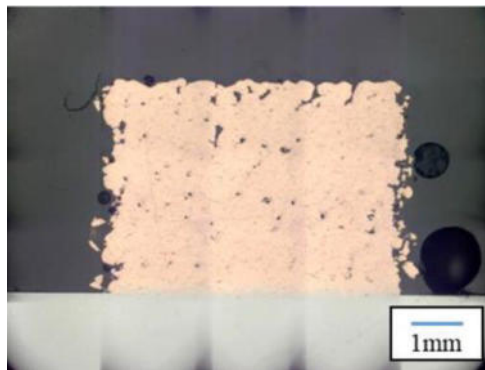


Fig. 2-25 a) Process map for copper processing using LPBF; b) cross-section of copper specimen showing relatively homogeneous center and porous borders. [86]

The relative density of copper was improved by Jadhav et al. [87], who with a 1030 nm fibre laser with a maximum power of 1 kW and a spot diameter of 40 μm , reached a maximum relative density higher than 98 %. The first trials in his study with laser power of 300 W lead to a relative density of 84 %. Nevertheless, by applying laser power of 600 to 800 W, laser velocity of 200-600 mm/s, and hatch distances of 0.07 and 0.09 the relative density was improved to more than 98 %. The specimen with the higher relative density was tested for electrical conductivity which reached 88 % of the fully homogeneous conventionally manufactured specimen.

It is evident that increasing laser power leads to higher relative densities of copper. A different approach was used by Hori et al. [88] who used blue diode laser with a maximum laser power of 200 W and reached a relative density of 99.1 %. The authors also compared the size of the fused zone of near-infrared and blue diode lasers and found that the fusion zone of the blue diode lasers was two to four times larger. To reach high relative density of volumetric samples, just switching to blue laser was not enough, and relative density reached just 94 %. Thus, authors developed special scanning strategy for reaching relative density of 99.1 % (Fig. 2-26).



a) Copper fabricated using blue diode laser; **b)** Scanning strategy for reaching relative density of 99.1 %. [88]

3 ANALYSIS AND CONCLUSION OF LITERATURE REVIEW

Intensive research is currently being conducted in the field of additive manufacturing of metals using PBF technologies. Researchers and industry are more focused on the LPBF in compared to EBM due to higher resolution, lower operating and machine costs [13]. Research activities in LPBF are mainly devoted to introducing new materials, process parameter tuning, and process parameters relation to microstructure and mechanical properties [15]. However, the LPBF allows to fabricate fully homogeneous parts with static mechanical properties comparable to conventionally fabricated parts [14]. There are still unknown gaps in the knowledge of material behaviour during processing, defects problems, repeatability, and reproducibility issues that restrict higher industrial acceptance [16, 17]. Furthermore, fabricated components suffer from low fatigue properties [49], high surface roughness, accuracy, and residual stresses. The residual stresses cause in-process part distortion and warping; thus, strong support structures are needed. Residual stresses also cause cracks in fabricated materials. Cracking is more common in materials with poorer weld ability [6]. Residual stresses evolve in the material due to high thermal gradients, nonhomogeneous and rapid cooling [27].

The efficient method for in-process minimizing residual stresses is realized by preheating. In the EBM, the preheating at high temperatures is realized by a defocused and accelerated electron beam, which is a common technique for producing crack-free fully dense components [11, 12]. The preheating in LPBF also become standard technique preferably to reduce thermal gradients in fabricated parts [8]. The preheating is realized mostly by the preheated base plate. The preheating in LPBF has effect on: lower thermal gradients [40]; decreased cooling rate [8]; lower energy necessary to melt the powder [20]; increased laser absorptivity [21]; the bigger size of the melt pool [36]; and microstructural changes [8, 60]. Thus, the preheating may be beneficial to increase material portfolio by reducing negative effects connected to laser beam reflectivity and residual stresses such as cracks, accuracy, and large amount of support structures. However, the oxygen content may increase in the fabricated component and the unfused powder due to preheating [61]. Thus, an inert atmosphere in appropriate quality must be ensured during the fabrication run.

Many researchers have tested preheating and its effect on the process ability of different kinds of materials. It was found that each group of material suffers from some process issues and needs to set its optimal process parameters, including a proper level of preheating temperature [8, 47]. The following text discusses the effect of preheating on observed material groups.

3.1 Titanium alloys

The titanium alloys offer an exceptional strength to weight ratio, therefore, are highly desired for complex parts fabricated using LPBF. The most used titanium alloy is Ti6Al4V. The predominant microstructure of Ti6Al4V observed in LPBF is composed of columnar grains and fine martensitic needles [50]. This microstructure leads to low ductility which may lead to in-process crack formation and warping due to high residual stresses. The martensitic evolution is caused by a rapid cooling rate of more than 410 K/s needles [50]. However, the ductility can be increased after production run by heat treatment. However, in-process defects must be minimized, for example, by process parameter adjustment or preheating [8, 51].

For in-situ martensitic decomposition it is necessary to acquire a temperature higher than 600 °C for a sufficient time [51]. This can be achieved by a shorter time between scanning adjacent layers, a higher layer thickness, lower density of support structures, and a larger specimen size [51]. However, those techniques are not always reachable while producing real parts. For example, part size cannot be changed, the scanning time depends on part size, thus cannot be lowered, a higher layer thickness would increase surface roughness and a lower support structures density may lead to warping. Thus, preheating may be a proper technique that is also applicable to real part production.

It was found, that preheating at 570 °C leads to α' martensitic decomposition to $\alpha+\beta$ structure which led to the increased of yield strength to 1176 MPa and elongation by 66 % against preheating at 100 °C [8]. Furthermore, the preheating temperature higher than 570 °C led to a decrease of residual stress to zero. The residual stresses can be further decreased using the meander scanning strategy with a rotation angle of 90° [7]. Furthermore, the remelting scanning strategy can be used to reduce residual stress. However, it may have a negative impact on mechanical properties and porosity [7]. Residual stresses can also be influenced by laser-related process parameters. The longer exposition time (lower laser velocity) and lower laser power with persisted energy density lead to lower residual stresses [28].

At present, studies devoted to the fabrication of titanium alloys using LPBF have been investigated the effect of preheating on the residual stresses, on static mechanical properties, and on the microstructure. Studies were mainly focused on the effect of preheating without tuning other process parameters. For example, Ali et al. [8] did not tune laser-related process parameters and, as they found, it has a negative impact on the mechanical properties while high temperatures were used. Therefore, a study that would assess the multifactorial experiment with a combination of process parameters and preheating is missing.

3.2 Intermetallic alloys

The intermetallic alloys exhibit very different physical properties from conventional alloys, for example, superconductivity, shape memory effect, high strength, stiffness creep, and corrosion resistance at elevated temperatures. The LPBF offers a new possibility to produce intermetallic alloys in near net shape. However, some challenges related to low ductility, low fracture toughness, high residual stresses, loss of alloy content, pores, and cracks must be overcome [52]. Thus, preheating was proposed and tested as a potential technique to mitigate those issues.

Overcoming these issues requires high preheating temperatures greater than 500 °C. The shape memory alloy NiTi processed with preheating at 300 °C had inconsistent tracks and cracks were observed. Preheating at 500 °C led to crack mitigation; however, the relative density reached just 97.1 % [53].

The γ -TiAls used in applications up to 900 °C were processed in the early stages using LPBF with a relative density of 97 % and contained many defects such as cracks and unmolten powder [54]. Preheating up to 450 °C decreased cracking [56]. Nevertheless, high temperatures must be used to fully eliminate cracks. Preheating must ensure temperature for a sufficient time in the fabricated material above the brittle-ductile transition, which is around 750-780 °C [58]. The crack-free specimen was produced with preheating to 900 °C [57]. However, the spherical pores gradually arise as the preheating temperature increased. Probably because of the excessive energy input from the laser beam. The high energy density also led to a decrease in the amount of Al content which affects the microstructure of the loss of resulting material [37]. Preheating even at 1000 °C was detected to have no effect on the loss of Al content. Thus, it can be assumed that the main effect is caused by energy density received from the laser beam. Thus, a proper combination of laser-related process parameters and preheating temperature can lead to crack free γ -TiAls without Al content loss. However, high-temperature preheating of around 900 °C must be used.

3.3 Steels

The LPBF is suitable for producing complex shapes even from hard-to-manufacture materials. Thus, tool steels with high hardness and wear resistance are tempting for researchers and industry. High hardness is usually associated with low ductility, which in LPBF due to residual stress leads to crack formation. High hardness is typical for tool steels with high carbon content, leading to a brittle martensitic crystalline microstructure due to rapid cooling [40]. Thus, the preheating should be higher than the martensite start temperature to increase ductility, lower temperature gradients, lower elastic modulus, and yield strength. That lead to relaxation of residual stress into the plastic flow of the material. Thus, crack formation restriction [61, 62]. A significant reduction of crack density was observed when alloys X65MoCrWV3-2 and X40CrMoV5-1 were processed with preheating at 300 °C [61, 62]. However, preheating led to a slightly increased oxygen content in solidified material and unfused powder [61]. Furthermore, preheating has the ability to increase the build ability of LPBF technology. It was demonstrated that preheating as another heat source even at 200 °C allows to use a higher laser velocity and maintain relative density at the same level [40].

3.4 Nickel-based alloys

Nickel-based alloys are susceptible to crack formation with an increasing content of Ti and Al elements [66]. Preheating in LPBF technology was presented as an efficient method for processing nickel-based alloys, which are susceptible to cracking. However, extremely high preheating temperatures up to 1200 °C were used [67].

In addition, preheating can decrease the residual stresses. Preheating up to 150 °C of IN718 decreased σ_z (building direction) residual stresses by 90 MPa compared to 50 °C [68]. The σ_x residual stresses did not significantly change in this temperature range. However, preheating had an effect on the microstructure, where with increasing preheating temperature, the inner-dendritic spacing and width of precipitates also increased. It may explain the slightly increased hardness values that increased from 310.8±8.9 HV to 314.9±11.3 HV when the temperature changed from 50 to 100 °C. The development of residual stress of IN718 according to the preheating temperature was simulated up to the preheating of 500 °C [69]. The analytical model showed that up to 200 °C the residual stresses will decrease. This was also experimentally confirmed. However, according to the simulation, higher preheating temperatures would lead to increased residual stresses due to heat accumulation and grain coarsening. This prediction was not tested experimentally.

3.5 Aluminium alloys

The most widely used aluminium alloy AlSi10Mg needs for reduction of deformation and residual stresses preheating temperature at least at 200 °C [35]. However, at temperatures higher than 150 °C the hardness decreased due to grain coarsening. The elimination of residual stresses by preheating was used to fabricate an overhang structure without support structures. With applied preheating of 380 °C an overhang was fabricated with a length of 10 mm from Al339 alloy [72]. Overhangs are usually not fabricable in LPBF due to heat shrinkage and tension forces [29, 30]. This method may potentially reduce the amount of support structures. Al-Si base alloys predominate in the LPBF process because of their relatively easy processing behaviour and no propensity to cracking. However, some applications require temperature-resistant or high-strength aluminium alloys. That properties offer Al-Cu alloys or EN AW 6000 and 7000 alloy groups. However, these alloys are classified as hard to weld and suffer from crack formation. The Al-Cu alloy was tested under preheating up to 400 °C, which significantly reduced cracks, but did not completely eliminate them [70]. The crack-free EN AW 6061 alloy was fabricated by LPBF using preheating at 500 °C [71]. The alloy reached mechanical properties in as build and heat treated T6 state comparable to wrought material.

3.6 Copper

Copper exhibits excellent thermal and electrical conductivity thus, is a desired material for heat exchangers, electric applications, and other applications [74]. However, the fabrication by LPBF brings issues related to the low laser energy absorptivity of lasers with wavelength 1000-1100 nm, high thermal conductivity, and oxygen affinity [76–79]. These issues researchers tried to overcome by using high-powerful infrared lasers with power up to 1 kW, alloying or adding element into pure copper, using preheating, and by using lasers with wavelength with better absorptivity [80]. However, even high-power lasers or blue diode lasers did not lead to fully homogeneous specimens [87, 88]. The researchers mainly focused on the adjustment of the laser-related process parameters and only one study was performed on the use of preheating at 100 °C [83]. Preheating has the ability to decrease laser power delivered from the laser source [20, 40], decrease the high thermal conductivity of copper [84], and decrease the reflectivity of the laser [21]. These factors can lead to copper processing with high relative density.

3.7 Summary

Based on analysis of the literature review, perspective research topics were pointed out for increasing knowledge of processing materials using LPBF. The first topic aims to process titanium Ti6Al4V and nickel-based IN939 alloys using high-temperature preheating. The review of the literature showed that there are still unknown gaps in knowledge of how Ti6Al4V behaves in high-temperature preheating in combination with other process parameters. Furthermore, the behaviour of IN939 under high-temperature preheating was simulated, but it needs to be experimentally tested. Those studies will further increase the knowledge about how process parameters and their combination affect residual stresses and relative density. The assumption is that higher preheating will lead to reduction of residual stress, which can be further used to reduce the quantity of necessary support structures. Thus, increase productivity and decrease financial expenses of LPBF by reducing manufacture time, waste material, and easier postprocessing.

The second perspective topic aims at increasing material portfolio. Preheating in LPBF has the ability to increase relative density. Moreover, it can act as another heat source, which can decrease laser power requirements. Thus, it can significantly improve the relative density of copper processed by using LPBF equipped with infrared lasers. It can lead to the fabrication of complex parts with unique properties.

4 AIMS OF THE THESIS

This dissertation thesis aims to experimentally investigate the effect of preheating on the Ti6Al4V alloy, Inconel 939 nickel-based alloy, and copper processed using LPBF. The main focus will be on the reduction of residual stress in the case of Ti6Al4V and IN939. Copper research will focus on clarifying the preheating effect in combination with other process parameters to maximize relative density. To achieve the main goal of this thesis, the solution of following subgoals will be necessary:

- Identification of main process parameters which affect the residual stress
- Finding a suitable method for residual stress measurement
- Finding a proper method for assessing multivariable experiments
- Elucidation of the effect of preheating and other process parameters on the residual stresses and relative density of Ti6Al4V specimens
- Elucidation of the effect of preheating on the residual stresses and relative density of IN939 specimens
- Defining the effect of high-temperature preheating and other process parameters on the relative density of copper specimens processed using infrared fiber laser

4.1 Scientific questions

Q1. Can the right combination of process parameters and preheating to 550 °C lead to the elimination of residual stresses in Ti6Al4V alloy and the cost-effective production of components manufactured using LPBF?

Q2. How does preheating affect the residual stresses of the nickel-based alloy IN939 processed using LPBF?

Q3. What is the effect of high-temperature preheating on the relative density of copper samples prepared with an LPBF system using infrared fibre laser?

4.2 Hypotheses

H1. Preheating temperature can significantly reduce residual stresses in Ti6Al4V [8]. However, residual stresses are also influenced by other process parameters, such as laser velocity, laser power, dwell time, and support structures [28, 51]. Thus, a proper combination of preheating and other process parameters should lead to the elimination of residual stresses even with preheating temperatures lower than 570 °C. The temperature of 570 °C was stated as the level for residual stress elimination [8].

H2. The effect of preheating was evaluated on different types of material and it was concluded that each group of materials needs its own process conditions [47]. The situation with preheating is the same; the appropriate magnitude of this parameter should be found. In general, a reduction in residual stresses can be expected at higher preheating temperatures [8]. Thus, residual stresses should decrease even in the IN939 alloy. However, excessive preheating can even increase residual stresses, as was simulated for the IN718 alloy [69].

H3. High reflectivity and thermal conductivity restrict the process ability of copper using LPBF [80]. Thus, the high-powerful laser systems must be used, or new lasers with different wavelengths must be developed [38, 86, 88]. High-temperature preheating has the ability to reduce those negative effects [84, 85]. Moreover, with applied preheating less energy must be acquired by the laser [20, 40]. Thus, those factors have potential to overcome issues with processing copper using infrared fiber lasers, and it can lead to homogeneous production of copper components.

4.3 Thesis layout

The dissertation thesis is composed of three scientific papers published in peer-review journals with an impact factor. The first article *Effect of Process Parameters and High-Temperature Preheating on Residual Stress and Relative Density of Ti6Al4V Processed by Selective Laser Melting* [I.] aims to answer the first scientific question of what is the proper combination of process parameters and preheating to reach the lowest residual stresses of the Ti6Al4V. The observed parameters were hatch laser velocity, hatch laser, power, border laser velocity, dwell time, and preheating up to 550 °C. Furthermore, the article discusses the effect of preheating on the unfused powder and its reusability. The second article *Effect of Preheating on the Residual Stress and Material Properties of Inconel 939 Processed by Laser Powder Bed Fusion* [II.] answers the second scientific question on how preheating affects the residual stresses of IN939. The effect of preheating on residual stress was experimentally tested up to preheating at 400 °C. Furthermore, the mechanical properties, macrostructure and microstructure changes, and also powder reusability were discussed. The third article *Effect of high-temperature preheating on pure copper thick-walled samples processed by laser powder bed fusion* [III.] aims to elucidate the effect of high-temperature preheating on copper, which is the subject of the third scientific question. In that article, a multivariable experiment focused on maximization of the relative density of the copper wall specimens was tested. The proper combination of laser power, laser velocity, layer thickness, hatch distance, sample thickness, and preheating up to 400 °C leading to maximum relative density was evaluated.

- I. MALÝ, Martin, Christian HÖLLER, Mateusz SKALON, Benjamin MEIER, Daniel KOUTNÝ, Rudolf PICHLER, Christof SOMMITSCH a David PALOUŠEK. Effect of Process Parameters and High-Temperature Preheating on Residual Stress and Relative Density of Ti6Al4V Processed by Selective Laser Melting. *Materials* [online]. 2019, 12(6), 930. ISSN 1996-1944. Available at: doi:10.3390/ma12060930



Journal impact factor = 3.748, Quartile Q1 (Metallurgy & Metallurgical Engineering)

Citations: 48

Author's contribution: 70%

- II.** MALÝ, Martin, Klára NOPOVÁ, Lenka KLAČURKOVÁ, Ondřej ADAM, Libor PANTĚLEJEV a Daniel KOUTNÝ. Effect of Preheating on the Residual Stress and Material Properties of Inconel 939 Processed by Laser Powder Bed Fusion. *Materials* [online]. 2022, **15**(18), 6360. ISSN 1996-1944. Available at: doi:10.3390/ma15186360

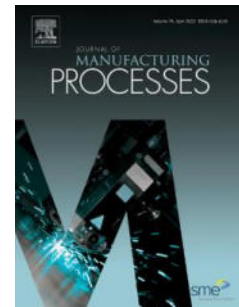


Journal impact factor = 3.748, Quartile Q1 (Metallurgy & Metallurgical Engineering)

Citations: 0

Author's contribution: 33%

- III.** MALÝ, Martin, Daniel KOUTNÝ, Libor PANTĚLEJEV, Laurent PAMBAGUIAN a David PALOUŠEK. Effect of high-temperature preheating on pure copper thick-walled samples processed by laser powder bed fusion. *Journal of Manufacturing Processes* [online]. 2022, **73**, 924–938. ISSN 15266125. Available at: doi:10.1016/j.jmapro.2021.11.035



Journal impact factor = 5.684, Quartile Q2 (Engineering, Manufacturing)

Citations: 7

Author's contribution: 52%

5 MATERIAL AND METHODS

5.1 Specimens fabrication

All specimens were fabricated on the SLM 280HL 3D printer equipped with 400 W ytterbium fibre laser YLR-400-WC-Y11 (IPG Photonics, Oxford, USA) with a focus diameter of 82 μm and a Gaussian shape power distribution. As a protective gas, argon was used for Ti6Al4V and IN939, and nitrogen for copper. The powder humidity was measured before each experiment using a Hytelog hydrothermometer.

For powder bed preheating in study I., focussed on Ti6Al4V alloy, a heating platform from SLM Solutions Group was used. The device was able to preheat the build platform up to 550 $^{\circ}\text{C}$, but the build area was reduced to a cylindrical shape with 90 mm in diameter and 100 mm in height. For preheating, a resistive heating element was used and the temperature was controlled by a thermocouple placed below the base plate made of stainless steel. The powder bed preheating in studies II. and III. was realized by an in-house manufactured heating device. The resistive heating elements in this heating device can preheat a top surface of the building platform up to 400 ± 10 $^{\circ}\text{C}$. The temperature was controlled by a PID regulator and by a thermocouple placed below the base plate. The device was calibrated before the start of the printing process by measuring the build surface temperature and its dependence on the set temperature on the PID regulator. The samples were printed on a base plate made of stainless steel in the II. study and copper in the III. study.

5.2 Powder characterization

The chemical composition, particle shape, and size distribution characteristics of the powders used for fabrication of the specimens were measured. The powder shape was evaluated by SEM. The chemical composition was determined by EDX and particle size by the laser diffraction method. The powders were fabricated by the gas atomization method.

In study [I.], Ti6Al4V powder was used with a particle mean size of 43 μm and a median size of 40.9 μm . Particles up to 29.97 μm represented 10% of particle distribution, while particles up to 58.61 μm represented 90%. The chemical composition acquired by EDX fits to the standard composition of the Ti6Al4V (Tab. 5-1).

Tab. 5-1 Chemical composition of virgin Ti6Al4V powder in weight percentage (wt. %).

Al	C	Fe	V	O	N	H	Ti
6.38	0.006	0.161	3.96	0.087	0.008	0.002	Bal.

In the study [II.], IN939 powder was used with a particle mean size of 35.8 μm and a median size of 34.3 μm . Particles up to 24.7 μm represented 10% of the particle distribution, while particles up to 48.7 μm represented 90%. The chemical composition acquired by EDX detected values of IN939 powder composition (Tab. 5-2).

Tab. 5-2 Chemical composition of virgin IN939 powder in weight percentage (wt. %).

Cr	Co	Ti	W	Al	Ta	Nb	Ni
20.00 \pm 0.40	18.23 \pm 0.90	3.83 \pm 0.45	1.83 \pm 0.15	1.63 \pm 0.15	1.60 \pm 0.10	0.83 \pm 0.15	51.57 \pm 0.75

In the study [III.], copper powder of 99.5% purity was used with a particle mean size of 25.9 μm and a median size of 25.7 μm . Particles up to 22.8 μm represented 10% of particle distribution, while particles up to 29.4 μm represented 90%. The chemical composition of copper powder, declared by material supplier, is stated in Tab. 5-3.

Tab. 5-3 Chemical composition of virgin copper powder delivered by vendor.

Cu (wt %)	As (ppm)	Bi (ppm)	S (ppm)	Sb (ppm)	Ag (ppm)	Mg (ppm)	P (ppm)
Bal.	<20	<20	<20	<15	<10	<10	<10
Pb (ppm)	Si (ppm)	Sn (ppm)	Zn (ppm)	Al (ppm)	Cd (ppm)	Co (ppm)	Cr (ppm)
<10	<10	<10	<10	<5	<5	<5	<5
Fe (ppm)	Mn (ppm)	Ni (ppm)					
<5	<5	<5					

5.3 Measurement methods

Measurement methods are described in detail in the attached studies. In this chapter, methods for residual stress and relative density evaluation are described.

5.3.1 Residual stress measurement

Residual stress was indicated by deformations of specially designed bridge-like specimens Fig. 5-1. The bridge curvature method is often used in LPBF for fast comparison of process parameters and their influence on residual stress [89, 90]. The distortions were measured on the top surface in half-cut state using the 3D scanner Atos TripleScan 8M.

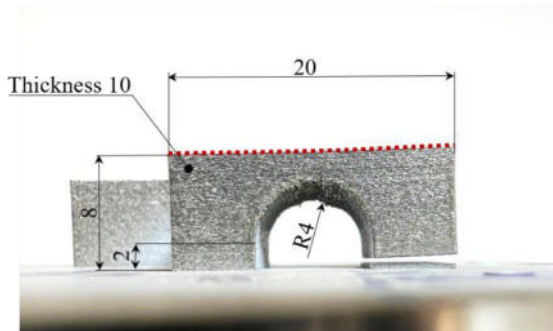


Fig. 5-1 Bridge-shaped specimen in the cut state with dimensions and marked top surface (red dotted line).

5.3.2 Relative density measurement

Relative density was measured in all publications by optical method from the polished cross-sectioned specimens. The relative density was evaluated in ImageJ v. 1.52k software in the inner area of the cross-sectioned specimens. The images for evaluation were converted to 8-bit type and relative density was evaluated with an automatic threshold.

5.4 Experimental design

In the experiments, a combination of process parameters was usually tested. Therefore, to determine their influence on the observed result, the methods for experimental planning were used. The surface response design and fractional factorial methods were also used to decrease possible combinations of process parameters. Therefore, decrease the number of specimens. The acquired data were analysed in Minitab software. The variables tested with the results are well described in the attached studies.

6 RESULTS AND DISCUSSION

In the experimental study [I.] *Effect of Process Parameters and High-Temperature Preheating on Residual Stress and Relative Density of Ti6Al4V Processed by Selective Laser Melting*, the influence of various process parameters in combination with preheating on residual stress and relative density of Ti6Al4V was tested. Process parameters that were experimentally tested were selected according to the literature review. The tested process parameters were: hatch laser speed, hatch laser power border laser velocity, waiting time between adjacent layers, and powder bed preheating up to 550 °C. For a comprehensive evaluation, the surface response design method was used to find the process parameters that have the greatest influence on residual stress and relative density. Furthermore, the evaluation method has found their optimal combination. At the end of the study, the effect of preheating on the unfused powder was evaluated.

The range of laser-related process parameters was defined according to standard process parameters used for Ti6Al4V adjusted for preheating temperature of 200 °C. The tested preheating temperature range was from 200 to 550 °C, which was the maximum of the used preheating device. The hatch laser power was tested in range of 100 to 275 W, hatch laser velocity from 700 to 1100 mm/s, and border laser velocity from 350 to 800 mm/s. Overall, preposition was that with higher preheating temperature, it will be possible to reach fully homogeneous specimens with higher laser velocities and thus, higher production rate. The delay time (time between scanning adjacent layers) was tested in the range of 22 to 73 s.

The distortions of the specimens and thus the residual stresses were mainly affected by preheating. The analysis of variance also showed that preheating and hatch laser power have a linear characteristic on the distortions, however, the hatch laser velocity and dwell time have a non-linear characteristic. The lowest distortions can be reached according to the regression model with the highest laser power, the lowest laser velocity, the shortest dwell time, and maximum preheating. The linear contribution of preheating was calculated as 46.31%. The second most influencing parameter was hatch laser power with a contribution of 17.22%. The increasing dwell time led to higher distortions and the parameter had 5.26% linear contribution effect on the distortions. Thus, the results showed that the highest energy density in combination with the highest preheating and the shortest dwell time leads to the lowest distortions. This means that the highest temperature accumulated in the specimens during the production run can be expected. This conclusion fits the overall observed behaviour of Ti6Al4V [8, 51] and can be explained as the slowed cooling speed and longer time in the ductile state which led to the relieve of internal stresses [52]. The overall distortions decreased, but they were not fully eliminated and the specimen without distortion was not fabricated. The results show that a higher energy density can lead to even lower distortions in combination with a preheating of 550 °C. However, slow laser velocity can significantly prolong fabrication time, and high laser power can lead to increased porosity [70].

The result showed that the relative density of the Ti6Al4V specimens was mainly influenced by hatch laser power and velocity. These parameters had together a linear contribution of 84.96% to the relative density. The dwell time in the observed range had a minimum linear contribution of 1.58% to the relative density. The preheating temperature had a positive effect on relative density. The linear contribution was 2.88%. Thus, it was confirmed that preheating has a positive effect on the relative density. However, in the case of Ti6Al4V, the contribution of preheating in the range of 200 to 550 °C on the relative density was less than 3%, but it can be important for other materials, for example copper. Furthermore, higher laser velocities can be used in combination with preheating. Thus, it has a potential to increase productivity.

The important conclusion was made with the effect of preheating on the unfused powder. High-temperature preheating led to visible changes in the colour of the Ti6Al4V powder. Thus, the unfused powder was analysed, and the source of changed optical properties was discovered. Preheating at 550 °C led to rapid increase in oxygen and hydrogen content, which exceeded the maximum values allowed by the ASTM B348 Grade 5 standard. The higher temperature increased the diffusion rate of oxygen and hydrogen [91], which are present due to the residual oxygen content in the inert atmosphere and the moisture contained in the powder. Oxygen content in Ti6Al4V increases ultimate and yield strength, but decreases ductility [92–94]. The ductility is also decreased by hydrogen, which can lead to part failures; thus, the content of hydrogen and oxygen is strictly monitored [95, 96]. The content of oxygen and hydrogen was not measured in the produced parts. However, powders that contain an elevated amount of these elements are not reusable for critical components because of the risk of failure. Standardly used preheating at 200 °C did not cause a change in hydrogen content, but a slightly increased oxygen content was detected. However, the chemical composition of the powder used in combination with 200 °C preheating did not exceed the maximum allowed value. Thus, it is still recyclable.

The first study showed that preheating at 550 °C of Ti6Al4V in combination with the process parameters can lead to the significant reduction of residual stress. However, the residual stresses were not fully eliminated. Furthermore, the increased oxygen and hydrogen content in the unfused powder restricts its reusability. Thus, this method is not cost effective in combination with relatively expensive titanium powder. The solution may be in using vacuum instead of an inert atmosphere and also in minimizing the moisture in the powder. However, the vacuum system will further increase the machine and operating costs. Further research was conducted with IN939, which is the heat resistant alloy; thus, the problem with oxygen content may be minimal.

The second study *Effect of Preheating on the Residual Stress and Material Properties of Inconel 939 Processed by Laser Powder Bed Fusion* [II.] aimed mainly at evaluating the preheating on residual stresses in the IN939 alloy. Furthermore, the effect on relative density, macrostructure, microstructure, mechanical properties, and unfused powder was observed. In this study, the effect of preheating was evaluated at the three levels; room temperature, 200 °C, and 400 °C.

The results of the deformation of the bridge curvature specimens showed that due to the preheating of 400 °C, the distortions and therefore the residual stresses unexpectedly increased. This result contradicts studies of other materials, such as aluminum, steels, and titanium [8, 35, 40] and the conclusion of the first study [I.] with Ti6Al4V. Furthermore, studies on IN718, which is a nickel-based alloy, showed that preheating from room temperature to 200 °C should decrease residual stresses [68, 69]. However, the IN718 simulation showed that higher preheating temperatures can even increase residual stresses due to overheating and grain coarsening [69].

IN939 showed a minor increase in distortion of 4.2 % in bridge curvature specimens when the preheating temperature changed from room temperature to 200 °C. A higher increase in the distortion was observed when preheating was used at 400 °C. Then the distortions increased about 16.2 % compared to room temperature.

The preheating of the base plate had an influence on the mechanical properties of IN939. The mean hardness and tensile properties such as ultimate tensile strength and 0.2 % proof stress increased and the elongation at break decreased. The specimen fabricated at room temperature had a mean hardness of 321 ± 26 HV 1 and the specimen at 200 °C 326 ± 19 HV 1. The hardness increased significantly to 359 ± 22.5 HV 1 when 400 °C preheating was applied. A similar trend was observed with the tensile properties. When room temperature and 200 °C preheating was applied, there was just a minor influence on the ultimate tensile strength, 0.2 % proof stress, and elongation at break. However, the ultimate tensile strength and 0.2 % proof stress increased by 26 % and 25 %, respectively, and the elongation at break decreased by 48.8 % when comparing the room temperature and the preheating to 400 °C.

The relative density of IN939 specimens did not change significantly and in all preheating levels was higher than 99.8%. No cracks were observed in any specimen. The difference in macrostructure was observed in the mean width of the melt pool. The mean melt pool width of the room temperature specimen was measured as 88.5 μm, 101.7 μm and 123.4 μm for the specimens preheated at 200 °C and 400 °C. Thus, melt pool width increased by 39.4% compared room temperature and 400 °C means a lower cooling rate can be expected.

The lower cooling rate and thermal gradients caused by preheating had a significant effect on the microstructure of IN939. Preheating at 400 °C resulted in wider columnar grains by 16% compared to room temperature. However, the overall frequency of occurrence of columnar grains decreased. The decrease in their occurrence is attributed to the reduced thermal gradients, which was also detected in the IN718 study. Preheating affects the orientation of the fine grains and contributes to the columnar to equiaxial transition by reducing the thermal gradients [68, 97]. Furthermore, the carbide phase was detected in specimens made of IN939.

Excellent mechanical properties at elevated operating temperatures of IN939 are usually acquired by precipitation hardening heat treatment. Heat treatment leads to precipitation of γ' phase and carbides. The precipitates detected by backscattered electron SEM are composed of MC-type carbides based on their location between grains, contrast, and size. The preheating temperature had a significant influence on the size and appearance of the carbide phase. The mean size of the carbide phase increased from 0.061 μm at room temperature by 41% at preheating at 200 °C and by 72% at preheating at 400 °C. The occurrence of carbide phase slightly decreased at preheating to 200 °C by 8.7% compared to the value of the room temperature specimen where $1.26 \pm 0.41 \mu\text{m}^{-2}$ was measured. However, preheating at 400 °C increased the occurrence of carbide phase per area by 23.8% compared to room temperature.

In addition, a significant influence of location on the specimen was detected. The three locations were measured, bottom, center, and top of the specimens. The location at the top is approximately in distance of 7 mm from the bottom location. The size and occurrence per area of the carbide phase gradually dropped from the bottom to the top location. The most significant drop occurred in specimens preheated at 400 °C. Then the average grain size and occurrence per area dropped by 14.6% and 37.8% compared the bottom and upper locations of the specimens.

The results of occurrence per area and size of the carbide phase showed that higher preheating temperature leads to increased concentration and size of carbides in IN939 alloy. Furthermore, a significant effect on the size and concentration of the carbide phase had time for which the specimens were exposed to elevated temperatures. The size and amount of carbide phase correspond to the measured tensile properties, hardness, and deformations. The carbide phase increased the ultimate tensile strength, 0.2 % proof stress, and hardness, but decreased elongation at break. Moreover, formation of precipitates caused the increased level of inner residual stresses and higher deformation of the specimens.

The chemical composition of the main alloy elements in the unfused powder detected by EDX was not changed. Furthermore, the powder grains of the powder used during preheating at 400 °C were not sintered together. However, the EDX analysis, which compared the virgin and powder used at preheating of 400 °C, detected a slightly increased oxygen content, but the concentration did not exceed the detection limit of 2 wt. % of XRD analysis. The oxygen content increased even though the concentration was strictly controlled and kept below 0.1 %.

The study of IN939 and its behaviour under high-temperature preheating showed that an increase in the preheating temperature cannot automatically acquire lower residual stresses. Although the unfused powder did not rapidly oxidise using the preheating temperature of 400 °C, the residual stresses increased due to the evolution of the carbide phase. Thus, preheating as a method for residual stress reduction is not appropriate for IN939.

The third study *Effect of high-temperature preheating on pure copper thick-walled samples processed by laser powder bed fusion* [III.] aimed to elucidate the effect of preheating 400 °C and other process parameters on the copper specimens fabricated using LPBF. The first study showed that preheating had the positive effect on the relative density of Ti6Al4V specimens. Thus, the preposition was that it will also have a positive impact on the relative density of copper. Therefore, the main objective of the third study was to fabricate homogeneous thin-walled specimens. Moreover, the effects of layer thickness, laser speed, laser velocity, hatch distance, sample width, scanning, and remelting strategy were studied. The copper material is suitable for its high thermal conductivity for the fabrication of coolers that are mainly composed of thin wall structures. Thus, the objective was to fabricate walls with thicknesses of 0.5 to 1.7 mm. The multivariable experiments were evaluated by surface response design and fractional factorial method.

The copper is a relatively new material in LPBF therefore, the process parameters leading to the maximum relative density are unknown. Thus, the correct combination needed to be set. For that purpose, the experiment that evaluated laser power, laser velocity, hatch distance, and sample width was conducted. The 31 specimens were fabricated at preheating of 200 °C and once with a layer thickness of 0.05, and second with 0.03 mm. The maximum value of the relative density of samples with 0.05 mm layer thickness was 88.9% and samples with 0.03 mm 95.9%. With decreasing layer thickness, the mean relative density increased by 7%. Thus, the layer thickness was identified as the most influencing parameter for the relative density. According to this experiment, the combination of laser-related process parameters that lead to maximum relative density was found as: laser power 400 W, laser velocity 505 mm/s.

The effect of preheating 400 °C was tested on specimens which process parameters were set for the fractional factorial evaluation method. Preheating at 400 °C showed a significant improvement in relative density that increased in mean value by 4.4% compared to 200 °C specimens. The relative density measured by optical microscopy of some specimens was greater than 99%. The main reason was attributed to a much smoother build surface, which is one of the conditions to reach a high relative density [75, 98]. The smoother surface was attributed to the wider weld tracks and improved wetting conditions that were observed in the thin-wall experiment. Preheating decreased the cooling rate, therefore the melt pool had more time to spread. However, in all specimens, unconnected layers were observed, which can decrease thermal and mechanical properties [99]. Copper has a high affinity to oxygen and the creation of a thin oxide film that hinders wettability and flowability [78]. Thus, the issue with unconnected layers was attributed to oxide layers. This conclusion was confirmed by EDX element mapping, which confirmed oxides in voids between unconnected areas. However, preheating at 400 °C led to oxidation and sintering of the unfused powder. The SEM and EDX analysis confirmed a high level of oxidation of the powder grains. After the production run where preheating was used at 400 °C, the powder grains were covered with oxide layers with a thickness of 1 to 3 µm. However, the increased oxidation of the copper specimens was not detected.

Remelting in combination with 400 °C preheating was tested to further increase relative density. Remelting had a positive impact on the relative density, which in mean value increased by 2.8%. Remelting further increased the temperature in the bulk material, which increased the time required for dissolving oxides. Oxides are less stable at elevated temperatures [78].

This study showed that copper can be processed by a relatively low powerful laser with a maximum laser power of 400 W and wavelength of 1064 nm and reach a relative density over 99%. However, the high relative density was reached just in combination with preheating at 400 °C. Nevertheless, the main issue was identified in oxidation, which hinders bonding of layers and tracks. Preheating in combination with remelting showed that further increasing the temperature in fabricated specimens can lead to a higher relative density due to disassociation of oxides. However, preheating caused strong oxidation and sintering of the unfused powder, which restricts its reusability. Increased oxidation as a result of preheating was not indicated in the fabricated specimens. Thus, the positive influence of preheating, which can lead to the production of copper components in unique shapes with relative density greater than 99%, can outweigh the negatives connected to unfused powder waste.

Article

Effect of Process Parameters and High-Temperature Preheating on Residual Stress and Relative Density of Ti6Al4V Processed by Selective Laser Melting

Martin Malý ^{1,*}, Christian Höller ², Mateusz Skalon ³, Benjamin Meier ⁴, Daniel Koutný ¹, Rudolf Pichler ², Christof Sommitsch ³ and David Paloušek ¹

¹ Faculty of Mechanical Engineering, Institute of Machine and Industrial Design, Brno University of Technology, Technická 2896/2, 616 69 Brno, Czech Republic; Daniel.Koutny@vut.cz (D.K.); David.Palousek@vut.cz (D.P.)

² Institute of Production Engineering, Graz University of Technology, Inffeldgasse 25F, 8010 Graz, Austria; christian.hoeller@tugraz.at (C.H.); rudolf.pichler@tugraz.at (R.P.)

³ Institute of Materials Science, Joining and Forming, Graz University of Technology, Kopernikusgasse 24/I, 8010 Graz, Austria; mateusz.skalon@tugraz.at (M.S.); christof.sommitsch@tugraz.at (C.S.)

⁴ Materials—Institute for Laser and Plasma Technology, Joanneum Research, Leobner Straße 94, 8712 Niklasdorf, Austria; benjamin.meier@joanneum.at

* Correspondence: Martin.Maly2@vut.cz; Tel.: +420-541-144-927

Received: 26 February 2019; Accepted: 18 March 2019; Published: 20 March 2019



Abstract: The aim of this study is to observe the effect of process parameters on residual stresses and relative density of Ti6Al4V samples produced by Selective Laser Melting. The investigated parameters were hatch laser power, hatch laser velocity, border laser velocity, high-temperature preheating and time delay. Residual stresses were evaluated by the bridge curvature method and relative density by the optical method. The effect of the observed process parameters was estimated by the design of experiment and surface response methods. It was found that for an effective residual stress reduction, the high preheating temperature was the most significant parameter. High preheating temperature also increased the relative density but caused changes in the chemical composition of Ti6Al4V unmelted powder. Chemical analysis proved that after one build job with high preheating temperature, oxygen and hydrogen content exceeded the ASTM B348 limits for Grade 5 titanium.

Keywords: Selective Laser Melting; Ti6Al4V; residual stress; deformation; preheating; relative density; powder degradation

1. Introduction

One of the most popular additive manufacturing technologies is Selective Laser Melting (SLM). SLM technology allows the production of nearly full density metallic parts with mechanical properties comparable to the ones produced by conventional methods. Components are made layer-by-layer directly from powdered material, where each layer is selectively melted in an inert atmosphere by a laser beam [1–3].

Due to non-uniform spot heating and fast cooling, thermal gradients are formed in materials, which lead to the development of residual stresses [1]. Residual stress (RS) is described as stress which remains in the material when the equilibrium with surrounding environment is reached [4]. Unwanted RS in SLM can cause part failure due to distortions, delamination or cracking.

The RS measurement is possible by mechanical and diffraction methods; magnetic and electric techniques; and by the ultrasonic and piezoelectric effect. Mechanical measurements are usually based on material removal and its relaxation or measuring part distortion. Typical mechanical measurement

is a drilling method with an accuracy of ± 50 MPa [4]. The main advantage of this method is its ability to measure RS to the depth of 1.2 times the diameter of the drilled hole. The Bridge Curvature Method (BCM) is often used in case of the SLM for the fast comparison of process parameters and their influence on the RS [5]. The principle is based on measuring the distortion angle, after the sample is cut off from the base plate, using the bridge-like samples. Measuring accuracy could be affected by imprecise cutting or by angle evaluating method, thus measurement of the top surface inclination was proposed as a better technique [6,7]. Value of the RS can be determined by the simulation of measured distortion in Finite Element Method (FEM) analysis [8].

Ali et al. [9] proved that higher exposure time and lower laser power with preserved energy density lowered the RS due to lower cooling rate and temperature gradient. The variation of laser power and exposure time did not cause a change in yield strength of Ti6Al4V, but elongation increased with lower laser power and higher exposure time. The cooling rate and also the RS can be affected by layer thickness. Higher layer thickness prolonged the cooling rate and RS was lower, but with higher layer thickness the relative density was lowered [9,10].

Scanning strategy has a significant effect on the RS. Ali et al. [11] observed that with longer scanning vectors the RS increased. Due to prolonged time between scanning adjacent scan tracks, higher thermal gradients were induced. The lowest RS had a stripe strategy with the ninety-degree rotation. This conclusion was also confirmed by Robinson et al. [12]. Ali et al. [11] did not observe the positive or negative effect of the scanning strategy on mechanical properties nor relative density.

Powder bed preheating can significantly reduce the amount of RS [5,13,14]. Ali et al. [15] demonstrated that for Ti6Al4V-ELI material preheating of the build platform to the temperature of 570 °C effectively eliminated the RS. A positive influence of preheating on microstructure and mechanical properties of H13 tool steel was observed by Mertens et al. [16]. The preheating up to 400 °C in his study improved mechanical properties and the parts had more homogeneous microstructure. Formation of cracks can be also affected by preheating, which was observed during printing aluminium of 2618, 7075 [17,18] and tool steel [19].

In this study, the BCM samples made of Ti6Al4V were used to evaluate the effect of process parameters on the relative density and the RS. Investigated parameters were hatch laser speed, hatch laser power border laser velocity, waiting time between adjacent layers and powder bed preheating up to 550 °C. The design of experiment and the surface response method were used for a comprehensive evaluation of the effects of observed process parameters. Furthermore, the influence of high-temperature preheating on powder degradation was evaluated.

2. Materials and Methods

2.1. Powder Characterization

In this study, Ti6Al4V gas atomized powder (SLM Solutions Group AG, Lübeck, Germany) was used. The chemical composition of virgin powder delivered by the manufacturer is in Table 1. The powder shape was checked by scanning electron microscopy (SEM) LEO 1450VP (Carl Zeiss AG, Oberkochen, Germany). Figure 1a shows that the powder particles have a spherical shape with a low amount of satellites. The particles size distribution was analysed by laser diffraction analyser LA-960 (Horiba, Kyoto, Japan). Measured particle mean size was 43 μm and median size 40.9 μm . The particles up to 29.97 μm represented 10% of particle distribution while particles up to 58.61 μm represented 90% (Figure 1b).

Table 1. Chemical composition of virgin Ti6Al4V powder.

Al (wt %)	C (wt %)	Fe (wt %)	V (wt %)	O (wt %)	N (wt %)	H (wt %)	Ti (wt %)
6.38	0.006	0.161	3.96	0.087	0.008	0.002	Bal.

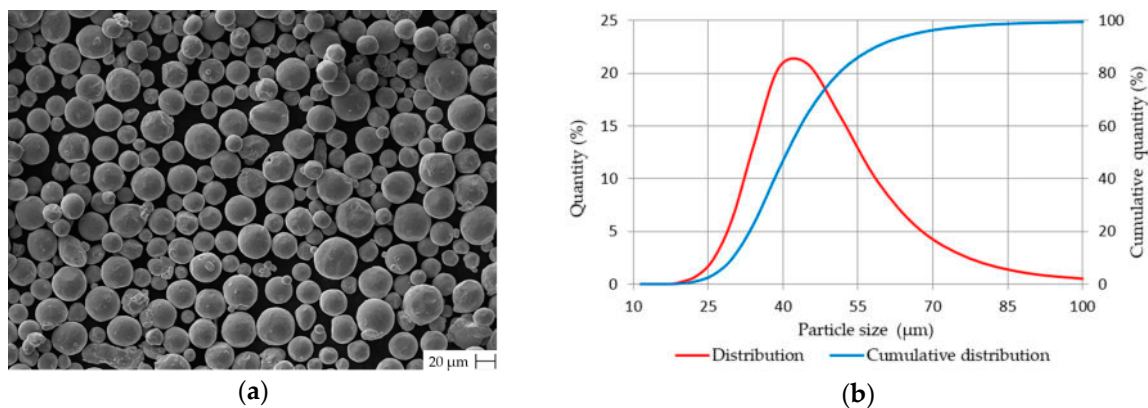


Figure 1. Ti6Al4V gas atomized powder characterization (a) shape evaluation by SEM; (b) particles size distribution.

The chemical composition of used powder was evaluated by the following methods. The aluminium content was checked by the inductively coupled plasma atomic emission spectroscopy. Oxygen and nitrogen contents were evaluated by hot extraction in helium by LECO TCH 600 (LECO Corporation, Saint Joseph, MO, USA). The hydrogen concentration was verified by the inert gas fusion thermal conductivity method JUWE H-Mat 2500 (JUWE Laborgeraete GmbH, Viersen, Germany). The accuracy of all methods is Al ± 0.327 wt %, O ± 0.008 wt % and N ± 0.0025 wt %.

2.2. Sample Fabrication

The samples were manufactured on the SLM 280^{HL} (SLM Solutions Group AG, Lübeck, Germany) 3D printer. The machine is equipped with 400 W ytterbium fibre laser YLR-400-WC-Y11 (IPG Photonics, Oxford, MS, USA) with a focus diameter of 82 µm and a Gaussian shape power distribution. Argon was used as a protective atmosphere during the process and the O₂ content was kept below 0.05 %. Before each experiment, the humidity of the powder was measured by the hydro thermometer Hytelog (B + B Thermo-Technik GmbH, Donaueschingen, Germany) with an accuracy of $\pm 2\%$. The powder humidity was kept under 10%. The heating platform (SLM Solutions Group AG, Lübeck, Germany) was used to preheat the powder. This device is able to preheat the build platform up to 550 °C, but the build area is reduced to a cylindrical shape with 90 mm in diameter and 100 mm in height. For the preheating a resistive heating element is used and the temperature is controlled by a thermocouple placed below the base plate. The temperature of a printed component may be slightly lower than the measured temperature by the thermocouple. However, the maximum height of parts printed in this study is 12 mm, thus the temperature field should be relatively homogeneous. Build data were prepared in Materialise Magics 22.03 (Materialise NV, Leuven, Belgium).

2.3. Sample Geometry

The geometry of samples was designed according to the BCM shape (Figure 2a) [5], therefore the effect of chosen process parameters on distortion and RS can be evaluated. Support structures were used for all samples to simulate the condition during the printing of real components. To restrict distortion during the SLM process (before cutting off) the 4 mm high block supports were reinforced with 1 mm block spacing, while fragmentation was switched off. Teeth top length was set to 1 mm. Support structures were added just under the pillars. Samples were rotated to 20° from recoating direction to ensure consistent powder spreading. Samples were cut in the middle of support structures and the evaluated parameter was top surface angle distortion α , which is the sum of α_1 and α_2 (Figure 2b).

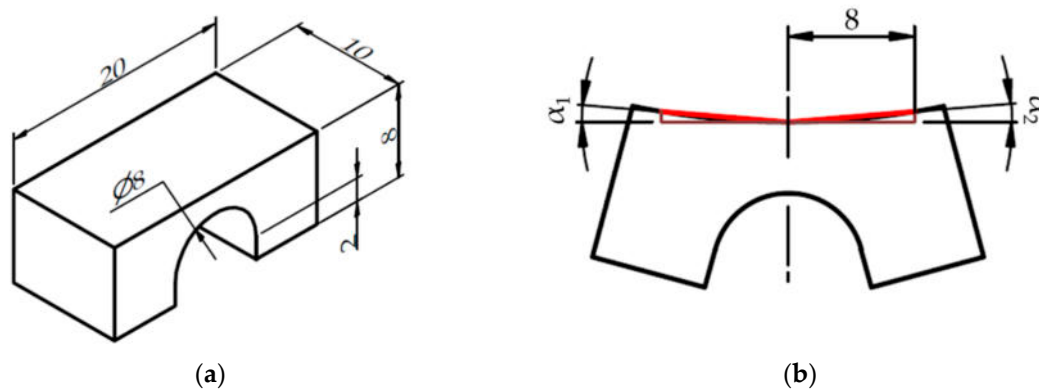


Figure 2. Samples geometry: (a) Dimensions of the BCM sample; (b) Measured bridge top surface angle distortion α is the sum of α_1 and α_2 . Dimensions presented in mm.

2.4. Design of Experiment

For data evaluation Design of Experiment (DoE) and Surface Response Design (SRD) were used. Hatch laser power (H LP), hatch laser velocity (H LV), border laser velocity (B LV), delay time (DT) and preheating temperature (T) were chosen as the variable factors. The range of parameters with central points is summarized in Table 2. The DT value is waiting delay between two adjacent layers, which was set in the printing machine. The real delay (RD) value which was used for result evaluation is composed of set DT between two layers and 13 s recoating time. If the DT is zero, then the RD value is composed of 13 s recoating time and scanning time. The temperature range was set from the common preheating temperature 200 °C to the maximum temperature of 550 °C that our equipment is capable to evolve.

Table 2. Table of used process parameters for Design of Experiment (DoE) and Surface Response Design (SRD).

Values/Parameters	H LP (W)	H LV ($\text{m}\cdot\text{s}^{-1}$)	B LV ($\text{m}\cdot\text{s}^{-1}$)	DT (s)	T (°C)
Minimum value	100	700	350	0	200
Middle point	187.5	900	575	30	375
Maximum value	275	1100	800	60	550

The half fraction of the SRD was built with the five continuous variable parameters. This means twenty-six samples plus four repetition central points. To minimize the number of global parameters, which has an influence on the whole build job, the face-centered design was used.

For evaluation, Minitab 17 (Minitab Inc., State College, PA, USA) was used. Data of the top surface angle distortion α were evaluated with full quadratic terms with 95% confidence level for all intervals and with backward elimination of 0.1. Relative density data were evaluated on samples 1–16 as the half fraction of factorial design. Then the data were assessed with 95% confidence level and insignificant term combinations were manually deleted.

Border laser power was set to 100 W and hatch spacing to 0.12 mm. The layer thickness of 50 μm and stripe strategy with a maximum stripe length of 10 mm and a rotation of 67° was used. Fill contour was turned off. Other parameters were set as standard.

2.5. Distortion Evaluation

The 3D optical scanner Atos TripleScan 8M (GOM GmbH, Braunschweig, Germany) was used for assessing distortions of the bridges. Each sample was scanned after cut-off from the base plate and after coating by TiO₂ mating spray with the thickness of around 3 μm [20]. The 3D scanned surface data were evaluated in GOM Inspect 2018 (GOM GmbH, Braunschweig, Germany).

The top surface angle distortion α was measured on the top surface of the bridge as is shown in Figure 2b. First, the Computer-aided Design (CAD) data of the undeformed bridge was fitted by Gaussian best fit function on the scanned data. Then three cross sections were created parallel to the YZ plane in distance 0, 8 and -8 mm. Lines using Gaussian best fit function were fitted on the top surface in each cross section (Figure 3a). Next, points in distance 0, 3 and -3 mm in Y direction were created on those three lines (Figure 3b). Then the distance was measured between middle and side points. Finally, X and Z components from each measured distance were used for calculating angle distortions by tangent function. Left and right sides were calculated separately. Therefore, the α value was calculated as the sum of angles on both sides. The result of the top surface angle distortion α value is the mean value of three measurements of one sample.

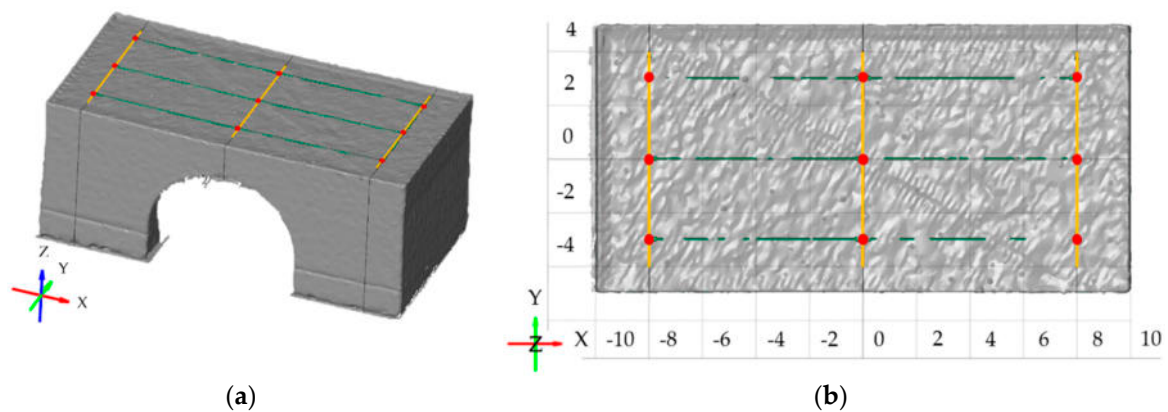


Figure 3. Distortion evaluation, fitted lines are yellow, line points are red and measured distances are green: (a) Isometric view on scanned data; (b) Top view of scanned data.

2.6. Relative Density Measurement

Relative density was determined using an optical method and was calculated as the mean value of parallel to build cross sections (Figure 4a). Value of relative density was evaluated in ImageJ v. 1.52k (National Institutes of Health, Bethesda, MD, USA). First, the picture of the cross section was converted to 8-bit type. Next, an automatic threshold was applied and relative density was evaluated in the areas defined by red rectangles (Figure 4b).

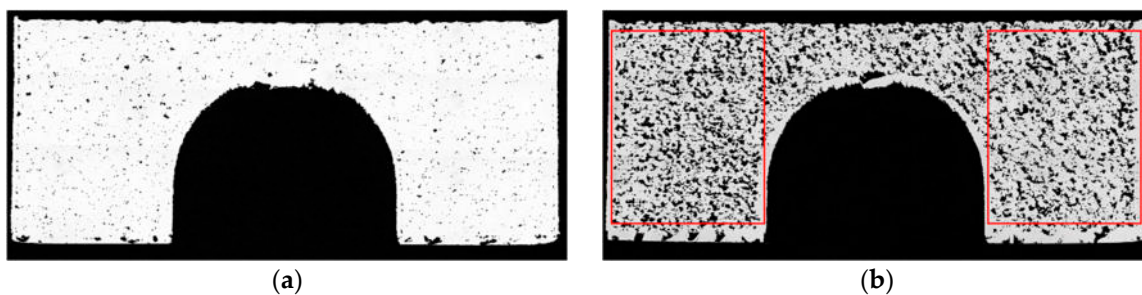


Figure 4. Cross sections of the BCM samples: (a) Cross section of sample 1; (b) Cross section of the sample made with the lowest energy density (Sample 3), red rectangles show area for relative density evaluation.

3. Results

3.1. Top Surface Distortion and Relative Density

The experimental design matrix and results of top surface angle distortion α and measured relative density are summarized in Table 3. Samples were sorted in printing order and horizontal lines represent a group of samples which were printed together in one build job.

Table 3. DoE and SRD test matrix with process parameters, the value of top surface angle distortion α and relative density.

Sample Number	H LP (W)	H LV (mm/s)	B LV (mm/s)	TD (s)	RD (s)	T (°C)	α (°)	Relative Density (%)
1	100	700	800	0	22	200	1.499	97.59
2	275	700	350	0	22	200	0.294	98.68
3	100	1100	350	0	22	200	1.201	74.04
4	275	1100	800	0	22	200	1.110	99.97
5	275	1100	350	60	73	200	1.127	99.60
6	100	700	350	60	73	200	1.413	97.06
7	100	1100	800	60	73	200	1.416	81.33
8	275	700	800	60	73	200	0.859	99.37
9	275	1100	350	0	22	550	0.437	99.69
10	100	700	350	0	22	550	0.389	98.68
11	275	700	800	0	22	550	0.406	99.43
12	100	1100	800	0	22	550	0.456	82.33
13	100	1100	350	60	73	550	0.917	91.17
14	100	700	800	60	73	550	0.520	98.93
15	275	1100	800	60	73	550	0.377	99.35
16	275	700	350	60	73	550	0.244	99.51
17	100	900	575	30	43	375	0.905	-
18	187.5	1100	575	30	43	375	0.943	-
19	187.5	900	575	30	43	375	1.000	-
20	187.5	900	800	30	43	375	0.771	-
21	275	900	575	30	43	375	0.454	-
22	187.5	900	350	30	43	375	0.764	-
23	187.5	700	575	30	43	375	0.795	-
24	187.5	900	575	30	43	375	0.740	-
25	187.5	900	575	0	17	375	0.174	-
26	187.5	900	575	60	73	375	0.876	-
27	187.5	900	575	30	43	550	0.392	-
28	187.5	900	575	30	43	200	0.809	-
29	187.5	900	575	30	43	375	0.716	-
30	187.5	900	575	30	43	375	0.668	-

3.2. Surface Response Model for Top Surface Angle Distortion α

Minitab 17 was used to establish a regression model for prediction of the top surface angle distortion α responses to the H LP, H LV, B LV, RD and T. Equation (1) represents the SRM-based mathematical model of significant parameters, which represent the relation between observed parameters. Table 4 and Figure 5 show results from an analysis of variance (ANOVA). The correlation of the regression model for α value is confirmed by determination coefficients $R^2 = 91.82\%$ and adjusted $R^2 = 86.04\%$.

$$\begin{aligned} \alpha = & 4.01 - 0.00766 \text{ H LP} - 0.00854 \text{ H LV} + 0.003232 \text{ B LV} + 0.0382 \text{ RD} - 0.001802 \text{ T} \\ & + 0.000005 \text{ H LV} \cdot \text{H LV} - 0.000252 \text{ RD} \cdot \text{RD} + 0.000004 \text{ H LP} \cdot \text{H LV} + 0.000005 \text{ H LP} \cdot \text{T} \\ & - 0.000002 \text{ H LV} \cdot \text{B LV} - 0.000018 \text{ B LV} \cdot \text{RD} - 0.000002 \text{ B LV} \cdot \text{T} \end{aligned} \quad (1)$$

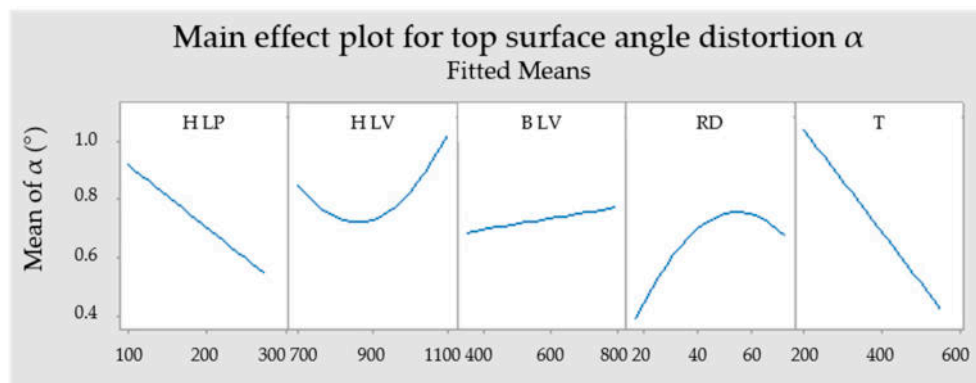


Figure 5. Main effect plot for top surface angle distortion α .

Table 4. ANOVA table for the top surface angle distortion α .

Source	DF	Contribution (%)	Adj SS	Adj MS	F-Value	P-Value
Model	12	91.82	3.44257	0.28688	15.9	0
Linear	5	73.01	2.81581	0.56316	31.21	0
H LP	1	17.22	0.64558	0.64558	35.78	0
H LV	1	3.62	0.13584	0.13584	7.53	0.014
B LV	1	0.59	0.03329	0.03329	1.85	0.192
RD	1	5.26	0.26462	0.26462	14.66	0.001
T	1	46.31	1.73648	1.73648	96.23	0
Square	2	4.73	0.17728	0.08864	4.91	0.021
H LV·H LV	1	1.79	0.17109	0.17109	9.48	0.007
RD·RD	1	2.94	0.11008	0.11008	6.10	0.024
2-Way Interaction	5	14.08	0.52797	0.10559	5.85	0.003
H LP·H LV	1	1.95	0.07309	0.07309	4.05	0.060
H LP·T	1	2.90	0.1089	0.10890	6.04	0.025
H LV·B LV	1	2.68	0.10043	0.10043	5.57	0.031
B LV·RD	1	4.62	0.17310	0.17310	9.59	0.007
B LV·T	1	1.93	0.07244	0.07244	4.01	0.061
Error	17	8.18	0.30677	0.01805	-	-
Lack-of-Fit	14	6.40	0.24014	0.01715	0.77	0.685
Pure Error	3	1.78	0.06662	0.02221	-	-
Total	29	100.00	-	-	-	-

In order to investigate the effect of high energy and high-temperature preheating on the distortion, an additional four bridge samples were made. Those samples were built with increasing H LP according to Table 5.

Table 5. Parameters of samples with increasing laser power and value of α .

Sample Number	H LP (W)	H LV (mm/s)	B LV (mm/s)	RD (s)	T (°C)	H Ed ($\text{J}\cdot\text{mm}^{-3}$) ¹	α (°)
31	275	700	350	22	550	65.5	0.363
32	300	700	350	22	550	71.4	0.224
33	325	700	350	22	550	77.4	0.313
34	350	700	350	22	550	83.3	0.098

¹ Calculated as $\text{H Ed} = \text{H LP} \cdot (\text{H LV} \cdot \text{Lt} \cdot \text{Hs})^{-1}$, Layer thickness (Lt) = 50 μm , Hatch spacing (Hs) = 120 μm .

3.3. Mathematical Model for Relative Density

Equation (2) represents a mathematical model of significant parameters with an influence on the relative density. Figure 6 shows a Pareto chart of standardized effect for evaluated relative density data. ANOVA results are shown in Figure 7 and Table 6. The correlation of the regression model for relative density value is confirmed by determination coefficients $R^2 = 89.38\%$ and adjusted $R^2 = 82.29\%$.

$$\begin{aligned} \text{Relative density} = & 136.67 - 0.1558 \text{ H LP} - 0.0628 \text{ H LV} - 0.00004 \text{ B LV} + 0.00766 \text{ T} + 0.0390 \text{ RD} \\ & + 0.000232 \text{ H LP} \cdot \text{H LV} \end{aligned} \tag{2}$$

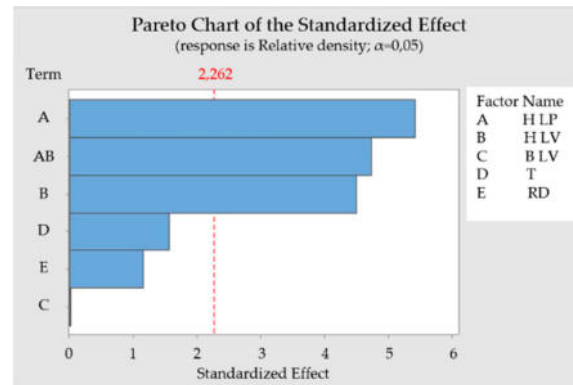


Figure 6. Pareto chart of the standardized effect to relative density.

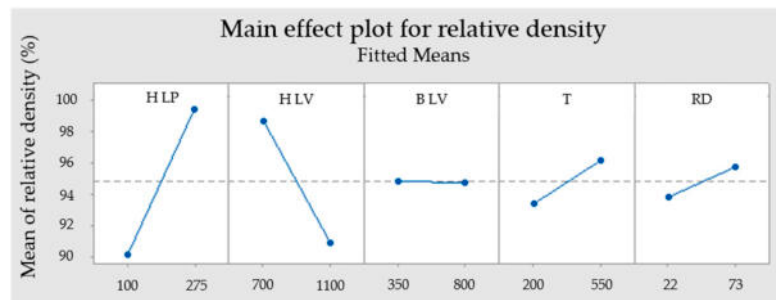


Figure 7. Main effect plot for relative density.

Table 6. ANOVA table for relative density.

Source	DF	Contribution (%)	Adj SS	Adj MS	F-Value	P-Value
Model	6	89.38	893.804	148.967	12.62	0.001
Linear	5	62.96	629.660	125.932	10.67	0.001
H LP	1	34.66	346.611	346.611	29.36	0
H LV	1	23.85	238.471	238.471	20.20	0.002
B LV	1	0	0.0010	0.001	0	0.993
T	1	2.88	28.756	28.756	2.44	0.153
RD	1	1.58	15.821	15.821	1.34	0.277
2-Way Interaction	1	26.41	264.144	264.144	22.38	0.001
H LP·H LV	1	26.41	264.144	264.144	22.38	0.001
Error	9	10.62	106.239	11.804	-	-
Total	15	100.00	-	-	-	-

3.4. Analysis of Used Powder

Figure 8a shows the influence of high-temperature base plate preheating (550 °C) on the powder. The powder significantly changed colour from silver to brown and there is a hint of particle

agglomeration. Therefore, the powder used in build job with 550 °C was checked by the SEM microscopy in order to investigate the particle agglomeration and their shape (Figure 8b).



Figure 8. The powder used in heating unit preheated to the 550 °C (a) Build job made with 550 °C; (b) SEM microscopy photo of the powder used with 550 °C.

Powder chemistry analysis was done after first build job with preheating to 200 °C and these results were compared with the powder used with 550 °C preheating. Results in Table 7 confirm a rise in oxygen content from 0.12 to 0.33 wt % and in the hydrogen from 0.002 to 0.0168 wt %. Aluminium content also slightly rose from 6.05 to 6.11 wt %, but nitrogen content decreased from 0.017 to 0.0149 wt %. Results are compared with the ASTM B348 Grade 5 titanium requirements and virgin Ti6Al4V powder chemical composition received by the vendor.

Table 7. Chemical composition analysis of the Ti6Al4V powder.

Powder State/Checked Elements	Al (wt %)	O (wt %)	N (wt %)	H (wt %)
ASTM B348 Grade 5	5.50–6.75	Max. 0.20	Max. 0.050	Max. 0.0125
Virgin Ti6Al4V	6.38	0.087	0.0080	0.0020
Ti6Al4V 200 °C	6.05	0.120	0.0170	0.0020
Ti6Al4V 550 °C	6.11	0.330	0.0149	0.0168

4. Discussion

4.1. Top Surface Angle Distortion α

The main contribution of each parameter on the distortion, and therefore the amount of residual stresses, can be derived from the ANOVA (Table 4). Further on the significance of each parameter can be evaluated by a p-value. If the value is lower than 0.05, then the parameter is significant, while the p-value of the lack-of-fit parameter should be high, which shows that the error value is not significant. The p-value of the lack-of-fit parameter 0.685 shows that the regression model for the top surface angle distortion α fits the measured data.

Table 4 and Figure 5 show that the most significant parameters for reduction distortions are T and H LP with 46.31% and 17.22% linear contribution. P-values of those parameters are 0. The RD and H LV are not that significant in comparison with the previous two parameters. Their linear contributions are 5.26% and 3.62%, while p-values are lower than 0.05, therefore parameters are significant. The B LV can be considered as an insignificant parameter with 0.59% linear contribution and the p-value greater than 0.05. Figure 5 indicates that H LP, B LV and T have linear behaviour in contrast to RD and H LV.

From the ANOVA results, it can be concluded that increasing the preheating temperature or laser power causes a reduction in deformation. In contrast, increasing H LV, B LV and RD lead to higher deformations. This can be contributed to the cooling rate, which is lower with slower laser movement,

higher preheating and shorter waiting time. Therefore, the thermal gradients, residual stresses and finally distortions are lower [9,11,15,21,22].

Optimal parameters for achieving the lowest distortion can be predicted from the fitted regression model (Figure 9). For reaching the lowest distortion it is predicted to use H LP 275 W, H LV 785 mm/s, B LV 350 mm/s, RD 17 s and T 550 °C. Predicted α is -0.182° . In contrast, the lowest distortion predicted with a preheating temperature of 200 °C is 0.139° .

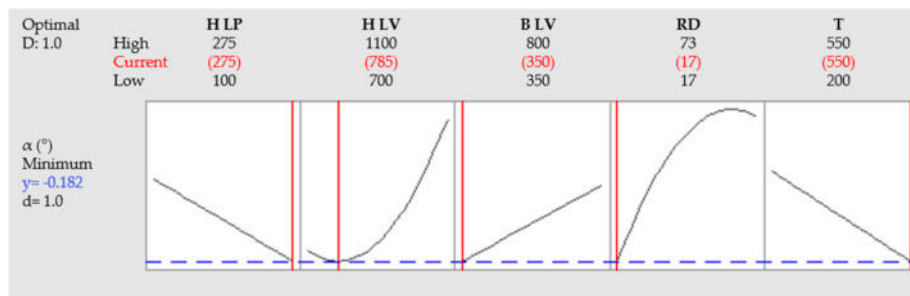


Figure 9. Predicted values for the lowest distortion in the full range of observed parameters.

Figure 10 shows the influence of energy density (ED) on the top surface angle distortion α . Samples used for this comparison were made with the same preheating temperature of 550 °C and 200 °C. The effect of B LV and RD was neglected. The interpolated line for 200 °C samples is constantly dropping with increasing ED and as was measured by Mishurova et al. [7], and this trend constantly continues. In contrast, the interpolated line for 550 °C samples with added high ED samples starts much lower than 200 °C line. The decrease of α value is gradual until 65 J/mm^3 and drops rapidly with higher ED.

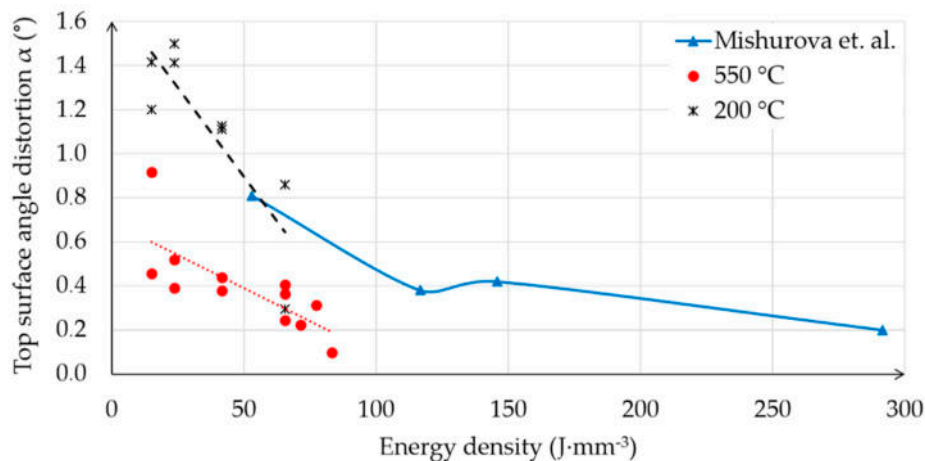


Figure 10. Effect of energy density on the top surface angle distortion α .

4.2. Relative Density

The most significant effect out of involved parameters influencing the relative density are H LP and H LV. The linear contribution is 34.66% for H LP and 23.85% for H LV. They are also significant in their two-way interaction with a contribution of 26.41%. P-values are 0 for H LP and 0.002 for H LV.

Preheating temperature has a linear contribution of 2.88% while its p-value of 0.153 is higher than 0.05. This means that this parameter in the observed range is not that significant for the model due to the high contribution of H LP and H LV. Relative density rose with higher T. Positive influence of preheating was also confirmed on stainless steel M2. It was proved by Kempen et al. [19] that with higher preheating temperature, higher laser velocities can be used while maintaining relative density.

The real delay has a linear contribution of 1.58% and a p-value of 0.277, which means the RD has minimal influence on relative density. Prolonged RD leads to an increase in relative density.

Border laser velocity with a linear contribution of 0 % and p-value 0.993 means that this parameter was not significant for the model, which can be due to the place where porosity was measured.

From the ANOVA (Figure 7) it can be deduced that a sample will have maximum relative density when values of H LP, RD and T are set as the highest and H LV as the lowest. This means the highest energy density is in the hatch.

4.3. Powder Degradation

There is clear evidence that the chemical composition of the powder significantly changed due to oxidation. Titanium alloys suffer high chemical affinity to oxygen leading to form a thin oxide layer even on air room temperature. Exposing titanium to an oxygen-containing atmosphere at elevated temperatures around 550 °C increase diffusion rates through thin oxide layers, and allows penetration of oxygen in the material [23]. After experiments with 550 °C preheating, oxygen content increased against 200 °C preheating from 0.12 to 0.33 wt % which is 0.13% higher than the ASTM B348 requirement for Grade 5 titanium.

Increased oxygen content in the Ti6Al4V causes an increase in yield and ultimate tensile strength, whilst ductility up to 0.19 wt % of the oxygen content remains constant [24]. Ti6Al4V additively manufactured alloy is due to rapid cooling mainly composed from α' martensitic microstructure even with preheating up to 550 °C [15]. Therefore, this is sensitive to oxygen content because of the concentration of oxygen higher than 0.22 wt % leads to the brittleness of the α' martensitic structure. Critical oxygen content for α and β structure is 0.4 wt % [25]. Oxygen concentration above 0.25 wt % leads to change in the typical microstructure, which causes a sharp decrease in ductility of Ti6Al4V [26].

Hydrogen content in the powder used under 550 °C exceeds the approved ASTM B348 limit value of 0.0125 wt % and its content rose from 0.002 to 0.0168 wt %. The diffusion rate of the hydrogen is rapidly increasing at the elevated temperatures [23]. The origin of the hydrogen element is most probably from powder moisture which was kept below 10%. Hydrogen in titanium alloys causes a phenomenon known as hydrogen embrittlement and could lead to part failure [27,28].

It was shown that the critical issues with processing the titanium alloy by SLM at high temperatures are connected with chemical composition changes in the unused powder, although the material was processed under argon atmosphere with oxygen concentration of 0.05% and powder humidity kept below 10%. The measured concentration of oxygen and hydrogen was beyond ASTM B348 requirement for Grade 5 titanium. Therefore, the used powder cannot be used for mechanical stressed parts.

5. Conclusions

Effects of hatch laser power, hatch laser velocity, border laser velocity, preheating temperature and delay time on residual stress and relative density on SLM processed Ti6Al4V samples have been investigated. In addition, the impact of preheating temperature up to 550 °C on Ti6Al4V powder degradation has been discussed. The main findings are the following:

- The preheating temperature has the main effect on the distortion and residual stress out of all observed parameters. With a high preheating temperature of 550 °C, the distortions of the top surface decreased and the relative density increased. The linear contribution effect of preheating was 46.31% on the distortion and 2.88% on the relative density.
- Relative density mainly depends on the hatch laser power and hatch laser velocity.
- Higher energy density decreased the deformations of the BCM samples. The value of the top surface distortion α decreased from 0.363° to 0.098° with increased energy density from 65.5 to 83.3 J·mm⁻³.

- Longer delay time negatively influenced distortions, but improved relative density. The linear contribution effect of the delay time was 5.26% on the distortions and 1.58% on the relative density.
- Powder bed preheating to 550 °C led to fast powder degradation. The oxygen and hydrogen content rose beyond the ASTM B348 requirement for Grade 5 titanium after one build job.

Author Contributions: Conceptualization, M.M., D.K.; methodology, M.M., C.H and M.S.; validation, M.M., C.H., B.M., M.S., D.K., R.P., C.S. and D.P.; formal analysis, M.M.; investigation, M.M., B.M. and M.S.; resources, R.P., C.S., D.K. and D.P.; data curation, M.M.; writing—original draft preparation, M.M.; writing—review and editing, M.M., D.K. and M.S.; visualization, M.M.; supervision, M.S., C.H., D.K., R.P. and C.S.; project administration M.M.; funding acquisition, C.S., R.P, D.K. and D.P.

Funding: This research was funded by the ESIF, EU Operational Programme Research, Development and Education within the research project [Architected materials designed for additive manufacturing] grant number [CZ.02.1.01/0.0/0.0/16_025/0007304] and faculty specific research project FSI-S-17-4144.

Acknowledgments: The authors express their thanks to Philipp Schwemberger from the Institute of Production Engineering, Graz University of Technology, for his help with the samples preparation.

Conflicts of Interest: The authors declare no conflicts of interest. The funders had no role in the design of the study; in the collection, analyses, or interpretation of data; in the writing of the manuscript, or in the decision to publish the results.

References






1. Kruth, J.P.; Froyen, L.; Van Vaerenbergh, J.; Mercelis, P.; Rombouts, M.; Lauwers, B. Selective laser melting of iron-based powder. *J. Mater. Process. Technol.* **2004**, *149*, 616–622. [[CrossRef](#)]
2. Schleifenbaum, H.; Meiners, W.; Wissenbach, K.; Hinke, C. Individualized production by means of high power Selective Laser Melting. *CIRP J. Manuf. Sci. Technol.* **2010**, *2*, 161–169. [[CrossRef](#)]
3. Gu, D.D.; Meiners, W.; Wissenbach, K.; Poprawe, R. Laser additive manufacturing of metallic components: Materials, processes, and mechanisms. *Laser Addit. Manuf. Mater. Des. Technol. Appl.* **2012**, *6608*, 163–180. [[CrossRef](#)]
4. Withers, P.J.; Bhadeshia, H.K.D.H. Residual stress. Part 1—Measurement techniques. *Mater. Sci. Technol.* **2001**, *17*, 355–365. [[CrossRef](#)]
5. Kruth, J.P.; Deckers, J.; Yasa, E.; Wauthle, R. Assessing and comparing influencing factors of residual stresses in selective laser melting using a novel analysis method. *Proc. Inst. Mech. Eng. Part B-Journal Eng. Manuf.* **2012**, *226*, 980–991. [[CrossRef](#)]
6. Le Roux, S.; Salem, M.; Hor, A. Improvement of the bridge curvature method to assess residual stresses in selective laser melting. *Addit. Manuf.* **2018**, *22*, 320–329. [[CrossRef](#)]
7. Mishurova, T.; Cabeza, S.; Artzt, K.; Haubrich, J.; Klaus, M.; Genzel, C.; Requena, G.; Bruno, G. An assessment of subsurface residual stress analysis in SLM Ti-6Al-4V. *Materials* **2017**, *10*. [[CrossRef](#)]
8. Sillars, S.A.; Sutcliffe, C.J.; Philo, A.M.; Brown, S.G.R.; Sienz, J.; Lavery, N.P. The three-prong method: A novel assessment of residual stress in laser powder bed fusion. *Virtual Phys. Prototyp.* **2018**, *13*, 20–25. [[CrossRef](#)]
9. Ali, H.; Ghadbeigi, H.; Mumtaz, K. Processing Parameter effects on residual stress and mechanical properties of selective laser melted Ti6Al4V. *J. Mater. Eng. Perform.* **2018**, *27*, 4059–4068. [[CrossRef](#)]
10. Mugwagwa, L.; Dimitrov, D.; Matope, S.; Yadroitsev, I. Influence of process parameters on residual stress related distortions in selective laser melting. *Procedia Manuf.* **2018**, *21*, 92–99. [[CrossRef](#)]
11. Ali, H.; Ghadbeigi, H.; Mumtaz, K. Effect of scanning strategies on residual stress and mechanical properties of Selective Laser Melted Ti6Al4V. *Mater. Sci. Eng. A* **2018**, *712*, 175–187. [[CrossRef](#)]
12. Robinson, J.; Ashton, I.; Fox, P.; Jones, E.; Sutcliffe, C. Determination of the effect of scan strategy on residual stress in laser powder bed fusion additive manufacturing. *Addit. Manuf.* **2018**, *23*, 13–24. [[CrossRef](#)]
13. Buchbinder, D.; Meiners, W.; Pirch, N.; Wissenbach, K.; Schrage, J. Investigation on reducing distortion by preheating during manufacture of aluminum components using selective laser melting. *J. Laser Appl.* **2014**, *26*. [[CrossRef](#)]
14. Vora, P.; Mumtaz, K.; Todd, I.; Hopkinson, N. AlSi12 in-situ alloy formation and residual stress reduction using anchorless selective laser melting. *Addit. Manuf.* **2015**, *7*, 12–19. [[CrossRef](#)]

15. Ali, H.; Ma, L.; Ghadbeigi, H.; Mumtaz, K. In-situ residual stress reduction, martensitic decomposition and mechanical properties enhancement through high temperature powder bed pre-heating of Selective laser melted Ti6Al4V. *Mater. Sci. Eng. A* **2017**, *695*, 211–220. [[CrossRef](#)]
16. Mertens, R.; Vrancken, B.; Holmstock, N.; Kinds, Y.; Kruth, J.P.; Van Humbeeck, J. Influence of Powder Bed Preheating on Microstructure and Mechanical Properties of H13 tool steel SLM parts. In *Laser Assisted Net Shape Engineering 9 International Conference on Photonic Technologies Proceedings of the Lane, Fürth, Germany, 19–22 September 2016*; Schmidt, M., Vollertsen, F., Arnold, C.B., Eds.; Elsevier: Amsterdam, The Netherlands, 2016; Volume 83, pp. 882–890.
17. Koutny, D.; Palousek, D.; Pantelejev, L.; Hoeller, C.; Pichler, R.; Tesicky, L.; Kaiser, J. Influence of scanning strategies on processing of aluminum alloy EN AW 2618 using selective laser melting. *Materials* **2018**, *11*, 298. [[CrossRef](#)]
18. Mertens, R.; Dadbakhsh, S.; Van Humbeeck, J.; Kruth, J.-P. Application of base plate preheating during selective laser melting. *Procedia CIRP* **2018**, *74*, 5–11. [[CrossRef](#)]
19. Kempen, K.; Vrancken, B.; Buls, S.; Thijs, L.; Van Humbeeck, J.; Kruth, J.P. Selective Laser melting of crack-free high density M2 High speed steel parts by baseplate preheating. *J. Manuf. Sci. Eng. ASME* **2014**, *136*. [[CrossRef](#)]
20. Palousek, D.; Omasta, M.; Koutny, D.; Bednar, J.; Koutecky, T.; Dokoupil, F. Effect of matte coating on 3D optical measurement accuracy. *Opt. Mater. AMST* **2015**, *40*, 1–9. [[CrossRef](#)]
21. Ali, H.; Ghadbeigi, H.; Mumtaz, K. Residual stress development in selective laser-melted Ti6Al4V: A parametric thermal modelling approach. *Int. J. Adv. Manuf. Technol.* **2018**, *97*, 2621–2633. [[CrossRef](#)]
22. Xu, W.; Lui, E.W.; Pateras, A.; Qian, M.; Brandt, M. In situ tailoring microstructure in additively manufactured Ti-6Al-4V for superior mechanical performance. *Acta Mater.* **2017**, *125*, 390–400. [[CrossRef](#)]
23. Lutjering, G.; Williams, J.C. *Titanium*, 2nd ed.; Springer: Berlin, Germany, 2007; ISBN 978-3-540-71397-5.
24. Tang, H.P.; Qian, M.; Liu, N.; Zhang, X.Z.; Yang, G.Y.; Wang, J. Effect of powder reuse times on additive manufacturing of Ti-6Al-4V by Selective electron beam melting. *JOM* **2015**, *67*, 555–563. [[CrossRef](#)]
25. Yan, M.; Xu, W.; Dargusch, M.S.; Tang, H.P.; Brandt, M.; Qian, M. Review of effect of oxygen on room temperature ductility of titanium and titanium alloys. *Powder Metall.* **2014**, *57*, 251–257. [[CrossRef](#)]
26. Yan, M.; Dargusch, M.S.; Ebel, T.; Qian, M. A transmission electron microscopy and three-dimensional atom probe study of the oxygen-induced fine microstructural features in as-sintered Ti-6Al-4V and their impacts on ductility. *Acta Mater.* **2014**, *68*, 196–206. [[CrossRef](#)]
27. Silverstein, R.; Eliezer, D. Hydrogen trapping in 3D-printed (additive manufactured) Ti-6Al-4V. *Mater. Charact.* **2018**, *144*, 297–304. [[CrossRef](#)]
28. Tal-Gutelmacher, E.; Eliezer, D. High fugacity hydrogen effects at room temperature in titanium based alloys. *J. Alloys Compd.* **2005**, *404–406*, 613–616. [[CrossRef](#)]



Article

Effect of Preheating on the Residual Stress and Material Properties of Inconel 939 Processed by Laser Powder Bed Fusion

Martin Malý ^{1,*}, Klára Nopová ², Lenka Klakurková ³, Ondřej Adam ², Libor Pantělejev ²
and Daniel Koutný ¹

¹ Institute of Machine and Industrial Design, Faculty of Mechanical Engineering, Brno University of Technology, Technická 2896/2, 616 69 Brno, Czech Republic

² Institute of Materials Science and Engineering, Faculty of Mechanical Engineering, Brno University of Technology, Technická 2896/2, 616 69 Brno, Czech Republic

³ Central European Institute of Technology (CEITEC), Brno University of Technology, Purkyňova 656/123, 612 00 Brno, Czech Republic

* Correspondence: martin.maly2@vut.cz; Tel.: +420-541-143-259

Abstract: One of the main limitations of laser powder bed fusion technology is the residual stress (RS) introduced into the material by the local heating of the laser beam. RS restricts the processability of some materials and causes shape distortions in the process. Powder bed preheating is a commonly used technique for RS mitigation. Therefore, the objective of this study was to investigate the effect of powder bed preheating in the range of room temperature to 400 °C on RS, macrostructure, microstructure, mechanical properties, and properties of the unfused powder of the nickel-based superalloy Inconel 939. The effect of base plate preheating on RS was determined by an indirect method using deformation of the bridge-shaped specimens. Inconel 939 behaved differently than titanium and aluminum alloys when preheated at high temperatures. Preheating at high temperatures resulted in higher RS, higher 0.2% proof stress and ultimate strength, lower elongation at break, and higher material hardness. The increased RSs and the change in mechanical properties are attributed to changes in the microstructure. Preheating resulted in a larger melt pool, increased the width of columnar grains, and led to evolution of the carbide phase. The most significant microstructure change was in the increase of the size and occurrence of the carbide phase when higher preheating was applied. Furthermore, it was detected that the evolution of the carbide phase strongly corresponds to the build time when high-temperature preheating is applied. Rapid oxidation of the unfused powder was not detected by EDX or XRD analyses.

Keywords: laser powder bed fusion; selective laser melting; Inconel 939; preheating; residual stress



Citation: Malý, M.; Nopová, K.; Klakurková, L.; Adam, O.; Pantělejev, L.; Koutný, D. Effect of Preheating on the Residual Stress and Material Properties of Inconel 939 Processed by Laser Powder Bed Fusion. *Materials* **2022**, *15*, 6360. <https://doi.org/10.3390/ma15186360>

Academic Editor: Sergei Tarasov

Received: 27 July 2022

Accepted: 7 September 2022

Published: 13 September 2022

Publisher's Note: MDPI stays neutral with regard to jurisdictional claims in published maps and institutional affiliations.



Copyright: © 2022 by the authors. Licensee MDPI, Basel, Switzerland. This article is an open access article distributed under the terms and conditions of the Creative Commons Attribution (CC BY) license (<https://creativecommons.org/licenses/by/4.0/>).

1. Introduction

Additive manufacturing (AM) technologies have been known since the 1980s and since then have made a great leap toward the reliable production of near net shape components made from a wide range of materials [1,2]. The ability to produce complex geometries even from materials that are to be processed opens new possibilities for increasing machine efficiency and producing organically shaped components [3]. The last 20 years have led to rapid progress in metal AM technologies, where the most studied and used are powder bed fusion (PBF) technologies [4–6]. PBF uses for component production an energy source which selectively fuses layers of fine metal powder according to part geometry until the components are completely finished. A laser beam is more commonly used as an energy source than an electron beam. Laser powder bed fusion (LPBF) takes the largest share among research and industrial applications, with more than 80% compared to electron beam melting (EBM) due to lower machine and operating costs and better beam resolution [7]. Research initiatives have focused on the introduction of new materials, repeatability of the process, qualification standards, and the reduction of production costs,

which hinder the acceptance of the technology in many industries [8]. Currently, a wide range of materials can be processed, including aluminium alloys, stainless steel, titanium alloys, and nickel-based superalloys [4].

Nickel-based superalloys are used in the energy and aerospace sectors because of their excellent oxidation resistance and creep properties at high temperatures. Traditionally, a casting process has been used to produce near net shape components. However, processing by PBF offers greater complexity, making it a tempting manufacturing process for nickel-based superalloys [9]. Inconel 718 (IN718) is the most widely used and studied nickel-based superalloy in PBF and is suitable for applications in the temperature range up to 650 °C [10]. For applications at temperatures up to 850 °C, another alloy must be used, for example, Inconel 939 (IN939) [11]. IN939 is a high-chromium alloy that can be used at elevated temperatures for a long period of time due to the strengthening of gamma prime (γ' -Ni₃(Al, Ti, Nb)) precipitates and carbides [12].

Components produced by PBF have a fine microstructure and exhibit static mechanical properties comparable to or even higher than their conventionally produced counterparts [4]. However, to achieve high mechanical properties, the correct process parameters for fabrication must be set. A non-optimal process setting can lead to gas porosity, key hole porosity, or lack of fusion defects [13]. In addition, defects such as cracks and part deformations have also been found in LPBF as a result of inhomogeneous heating and large thermal gradients, which lead to the evolution of anisotropic residual stress (RS). RSs are stresses that remain in material when equilibrium with the surrounding environment is reached [14]. The three types of RSs can be distinguished according to the scale on which they act [14]. Type I of RSs operate on macroscopic scales, and when their magnitude exceeds the yield strength of the material, part deformations may occur. Type I RSs are the most studied and described in the literature because they directly affect the manufacturability of the geometry and can be influenced by process parameters [8,15]. Although heat treatment for stress relieve can be performed after the production run, RS evolution occurs even during production and causes failures such as warping. Therefore, parts must be attached to the build platform directly or via support structures that must be fabricated along with the parts. Support structures increase manufacturing time, material consumption, and post-processing costs. However, RSs of the type I can be beneficial when they are applied on the finished component surface; for example, by shoot peening, they can increase fatigue resistance [16]. Type II RSs operate on the individual grain scale as a result of the different thermal and elastic properties of the differently oriented grains [14]. Type III RSs are on the atomic scale as a result of crystallographic lattice disorders. Types II and III are difficult to measure and are less important in terms of their mechanical properties [17]. Therefore, only type I of RSs are discussed in the following text. The problem with RS is more common in LPBF than in EBM, which is due to the higher preheating temperatures of the build chamber (500–800) °C in EBM. Higher preheating temperature reduces the temperature gradients and cooling rate [18].

Many researchers have investigated the proper settings of process parameters in LPBF for RS mitigation and have attempted to find universal laws for RS reduction [15,19]. The formation of RS has also been studied as a function of material properties. Many studies have shown that materials with higher thermal diffusion and thermal conductivity have a higher RS [8]. The RSs were also higher in materials with higher ultimate strength, yield strength, and coefficient of thermal expansion. However, the magnitude of RS also depends on the used process parameters and each material requires an optimum setting for the production of homogeneous parts [20]. Therefore, such universal laws are not always valid and inconsistencies can be found in the literature [3,21]. Such inconsistencies are also observed in the preheating of the base plate, where a higher preheating temperature generally reduces the RS [22], but excessive heating can increase RS [23]. Therefore, the optimal setting must be determined for each material. Excessive preheating of the powder bed can also have a negative effect on the properties of unfused powder and limit its recycling [15,24]; thus, it needs to be checked.

As outlined here, the evolution of RS in LPBF limits the manufacturing freedom, dimensional accuracy, and increases post-processing costs. Therefore, it is important to investigate the possibilities of mitigating RS through in-process process parameters and to develop optimal conditions that maintain it at a minimum level. This study investigates the effect of high-temperature preheating of the base plate up to 400 °C on the evolution of RS in IN939 produced by the LPBF. Moreover, it contains complex analyses describing the preheating effect on the microstructure, tensile properties, hardness, and properties of the unused powder, thus providing comprehensive information about material behavior under high-temperature preheating conditions.

2. Materials and Methods

2.1. Powder Characterization

Gas atomized IN939 powder (SLM Solutions Group AG, Lübeck, Germany) was used in this study. The chemical composition delivered by the material supplier was verified by energy dispersive X-ray spectroscopy (EDX) performed on AZtec SW (Oxford Instruments plc, UK, Abingdon, UK) and LYRA3 XMH (TESCAN, Brno, Czech Republic) scanning electron microscope (SEM) accessories. EDX analysis performed on three specimens showed that the mean values of the chemical composition met the alloy composition requirements, except for Cr, whose composition was 2 wt. % below the standard (Table 1). SEM analysis detected mainly spherical powder particles (Figure 1a). The particle size distribution (Figure 1b) was checked using laser diffraction analyzer LA-960 (Horiba, Kyoto, Japan). The median size was 34.3 μm and the mean particle size was 35.8 μm . The diameter of 10% of the particles was smaller than 24.7 μm , while the diameter of 90% did not exceed 48.7 μm .

Table 1. Material supplier specification and EDX measurement of chemical composition of virgin IN939 powder in weight percentage (wt. %).

	Ni	Cr	Co	Ti	W	Al	Ta	Nb
Material supplier	balance	22.20	18.86	3.65	2.04	1.92	1.43	1.00
EDX measurement	51.57 \pm 0.75	20.00 \pm 0.40	18.23 \pm 0.90	3.83 \pm 0.45	1.83 \pm 0.15	1.63 \pm 0.15	1.60 \pm 0.10	0.83 \pm 0.15

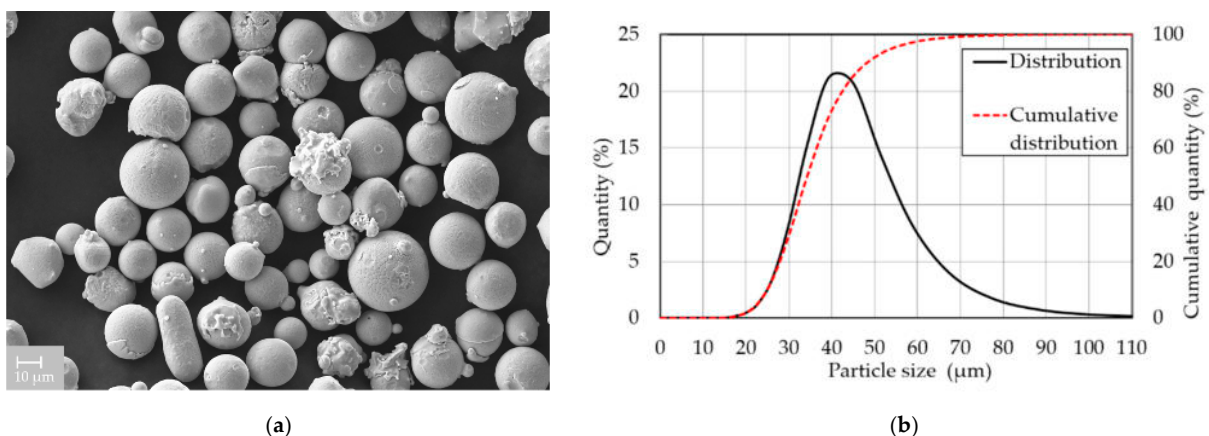


Figure 1. IN939 powder characterization: (a) SEM image showing mostly spherical particles; (b) particle size distribution.

X-ray diffraction (XRD) was performed on a SmartLab diffractometer (Rigaku, Austin, TX, USA) using CuK α radiation. The device operated with voltage $V = 40$ kV and current $A = 30$ mA. Continuous scanning was performed for 2θ from 35° to 120° with a step size of 0.02°. D-Tex with a β -filter in the secondary beam was chosen as the detector. PANAnalytical High Score Plus was used for qualitative and quantitative analyses using the pdf2 and ICSD databases. Quantitative analysis was performed using the Rietveld method with the external standard SI. Method error ± 1 wt. %. The limit of detection was 2 wt. %.

2.2. Specimen Fabrication and Characterization

An SLM 280HL 3D printer (SLM Solutions Group AG, Lübeck, Germany), equipped with a 400 W ytterbium fiber laser YLR-400-WC-Y11 (IPG Photonics, Oxford, MS, USA) with a focus diameter of 82 μm and a Gaussian shape power distribution, was used to fabricate the specimens. An in-house manufactured heating device was used to preheat the stainless-steel base plate. The heating device uses resistive heating elements and the temperature is controlled by a PID regulator and thermocouples. The accuracy of the temperature on the base plate is ± 20 $^{\circ}\text{C}$. The base plate preheating cannot ensure homogeneous preheating for high specimens, and the surface temperature gradually decreases within the specimen height. However, for specimens up to 10 mm, the preheating temperature should not decrease more than 15 $^{\circ}\text{C}$ [25]. Argon was used as the protective gas. The O_2 content was kept below 1000 ppm during the production run. The powder moisture content, which was checked using Hytelog (B + B Thermo-Technik GmbH, Donaueschingen, Germany) before each production run, was $3 \pm 2\%$. The fabricated specimens were analysed in the as built state.

The amount of RS was estimated using the bridge curvature method (BCM), in which one of the two pillars of the bridge-shaped specimens was cut out by electro-discharge machining, and the deflection of the top surface was measured (Figure 2a). The BCM is widely used in PBF and allows a qualitative asses process parameters and their direct effect on RS through deformation of the part [26,27]. The BCM specimens were produced directly on the build platform in the transverse (90°) and longitudinal (0°) directions corresponding to the direction of the powder recoating (Figure 2b). The geometry of the top surface was measured in each state using an optical 3D scanner Atos TripleScan 8M (GOM GmbH, Braunschweig, Germany). Data of the top surface deformation were determined as a mean value of the three virtual sections at a distance of 2.5 mm from each other. The virtual sections are shown in Figure 2b as red dotted lines on the top surface of one specimen.

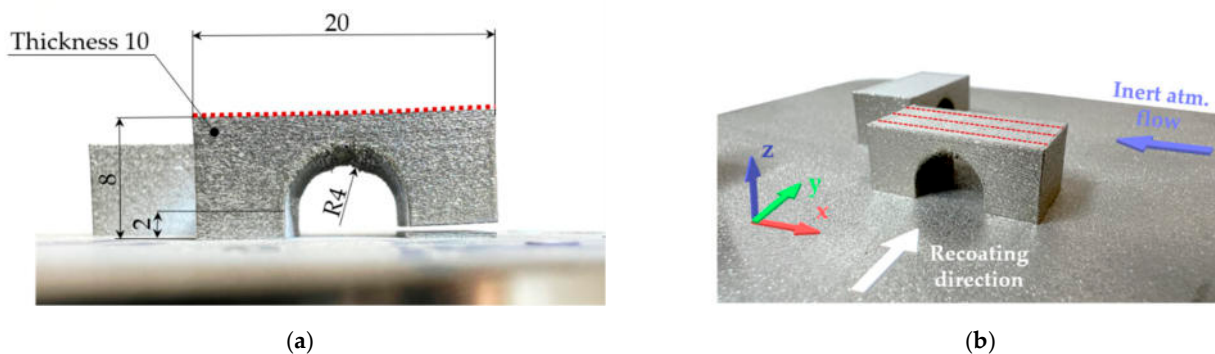


Figure 2. Bridge-shaped specimens: (a) specimen in the cut state with dimensions and marked top surface (red dotted line); (b) layout on the platform in the as built state with marked virtual section for measuring top surface distortion.

The distortion of the top surface, relative density, macrostructure, microstructure, and hardness were determined on the BCM specimens. Two horizontal tensile test specimens were produced for each preheating temperature according to the DIN 50125 B 30×6 mm standard. Cylindrical shape specimens with a gauge length of 30 mm and diameter of 7.2 mm were fabricated using LPBF and their surfaces were turned to a standard diameter of 6 mm before tensile testing. The tensile test at room temperature was carried out on Zwick/Roell Z250 equipped with extensometer MultiXtens (Zwick Roell Group, Ulm, Germany). The strain rate was set to 0.00007 s^{-1} until the 0.2% proof stress was reached, then the strain rate was 0.001 s^{-1} .

The BCM and tensile specimens were fabricated at room temperature (RT) and base plate preheating temperatures of 200 $^{\circ}\text{C}$ and 400 $^{\circ}\text{C}$. The preheating temperature of 400 $^{\circ}\text{C}$

is the maximum reachable temperature of the heating device. The meander scanning strategy was used and other process parameters were set for 0.05 mm layer thickness according to the powder supplier's recommendation.

For material analyses, the BCM specimens that were aligned with gas flow were cut in the middle along the Z-axis, and the XZ and XY planes were analysed. The orientation of the specimens on the platform and the XYZ axis are shown in Figure 2b. The cut specimens were hot-pressed into a polymer resin, ground, with SiC abrasive papers up to 4000 grit size, and subsequently polished by 3 μm and 1 μm diamond paste. For SEM analysis, the specimens were additionally mechanochemically polished using Struers OP-S suspension. To evaluate relative density, overview images of the XZ planes were taken in two different specimen planes at least 1 mm apart using the 3D digital microscope Keyence VHX-6000 (Keyence, Mechelen, Belgium). ImageJ software was used to analyze the relative density using an automatic threshold. The resulting value of the relative density is the average of the two different XZ planes of the specimen.

The macrostructure and microstructure were examined in an etched state (Kalling's: 2 g— CuCl_2 , 40 mL— HCl , and 60 mL—methanol) using an Olympus GX51 light microscope (Olympus, Tokyo, Japan) for macrostructure evaluation and SEM ZEISS Ultra Plus (Carl Zeiss AG, Oberkochen, Germany) and Tescan LYRA3 XMH (TESCAN ORSAY HOLDING, Brno, Czech Republic) for microstructure observation using backscattered electrons.

The width of the melt pool was determined in the XZ planes using a linear method in which the length of the lines used was divided by the number of intersecting melt pools. Furthermore, the mean columnar grain width was measured in the SEM images using linear method and ImageJ software. The mean values of the width of the melt pool and the columnar grain width are composed of at least 10 linear measurements. Moreover, the mean carbide size and occurrence per area were measured on SEM images using ImageJ software. The mean value of carbide size is made of a minimally 50 measurements. The value of occurrence per area was measured as the number of carbides in at least six areas with a size of 20 μm^2 .

A Vickers hardness test was performed to observe potential changes in the BCM specimen. The Vickers hardness test was performed in the XZ plane of the polished BCM specimens using a Qness testing machine Q10A (ATM Qness GmbH, Golling an der Salzach, Austria) with a test load of 9.807 N (HV 1) and holding time of 10 s, according to the ASTM E92-17 standard. The hardness on the XZ plane was measured in three lines along the Z-axis. On each line was measured 20 indentions homogeneously spread over the entire height of the sample.

3. Results

The results presented in this chapter show the effect of base plate preheating on the BCM specimens fabricated using LPBF. First, the effect on the deformation of the BCM specimens in the cut state is shown, followed by the macrostructure and microstructure evaluation. Changes in the macrostructure and microstructure of the material led to changes in the tensile properties and hardness properties, which are confirmed by the measured data presented in this chapter. The IN939 powder was exposed to elevated preheating temperatures. Therefore, the chemical and phase composition were verified by EDX and XRD analysis to evaluate its reusability.

3.1. Effect of Powder Bed Preheating on Residual Stress

Powder bed preheating usually leads to a lower RS and therefore less part distortion [15,22,28]. In the case of the IN939 BCM specimens, higher preheating temperatures caused a greater deflection of the top surface (Figure 3). The top surface distortion did not change significantly when RT and preheating at 200 °C were applied. The maximum distortion of 0.24 mm was measured at RT, while at 200 °C, the maximum top surface distortion was 0.25 mm, which is an increase of 4.2%. However, preheating to 400 °C resulted in an increase in distortion of 16.2% compared to RT and the maximum measured distortion was

0.28 mm. The deflection data in Figure 3 are the mean values of two specimens built at 0° and 90° according to the recoating direction.

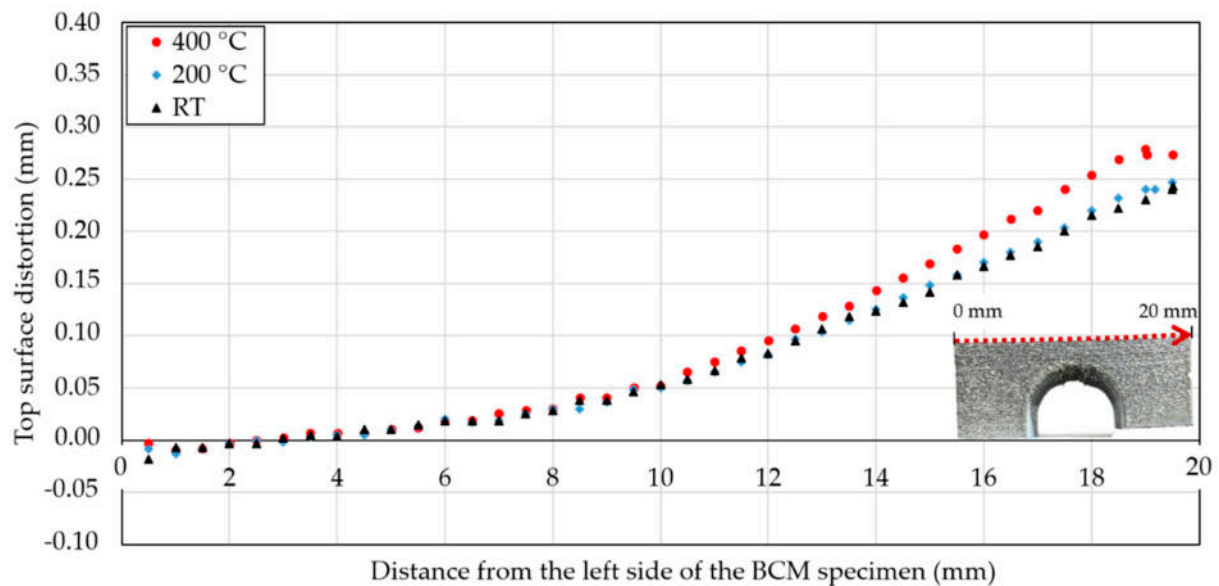


Figure 3. The mean values of 0° and 90° top surface deflection of BCM specimens according to base plate preheating temperature.

The orientation of the specimen on the build platform significantly affected the distortion of the top surface. Maximum distortion values on the top surface were always measured in the longitudinal (0°) direction according to the recoating of the powder (Figure 2a). The maximum deformation of the top surface of the longitudinal specimens was 0.1 mm greater (Table 2).

Table 2. Maximum value of the deformation of the top surface as a function of the orientation of the specimen on the build platform.

	90° (mm)	0° (mm)
RT	0.19	0.29
Base plate preheating of 200 °C	0.20	0.30
Base plate preheating of 400 °C	0.23	0.33

3.2. Effect of Powder Bed Preheating on Macrostructure and Microstructure

The influence of the base plate preheating temperature on the relative density was not significant. In all cases, the relative density was close to 100%. The relative density of the RT specimen was 99.9%, for specimens with a preheating at 200 °C (or 400 °C) the relative density was 99.9% (or 99.8%). The character and distribution of the pores were similar for all levels of the specimens and the studied planes. The observed pores had a spherical shape with diameters between 15 and 65 µm and were predominantly located near the surface of the specimens. No macrocracks and microcracks were observed in either case.

Light microscopy images in the XZ plane showed arch-shaped lines resulting from a uniformly shaped melt pools during the process (Figure 4a) as well as visible laser trajectories in the XY plane (Figure 4b). This macrostructure is typical for alloys produced by LPBF [29]. The mean width of the melt pool on the etched specimens was measured as part of the macrostructural evaluation. The mean width of the melt pool was determined to be 88.5 µm for the RT specimen, 101.7 µm for 200 °C, and 123.4 µm for the specimen preheated at 400 °C. Figure 5a,b shows the details of the microstructure of the RT and specimens preheated at 400 °C in the XZ plane. The observed microstructure was characterised by a very fine cellular/dendritic structure with columnar grains in several melt pools

elongated along the build direction. Some melt pools showed the presence of columnar grains growing in the direction of the thermal gradient (parallel to the build direction). Several columnar grains pass through a few melt pools (Figure 5b), which leads to strong bonding between the individual layers [11].

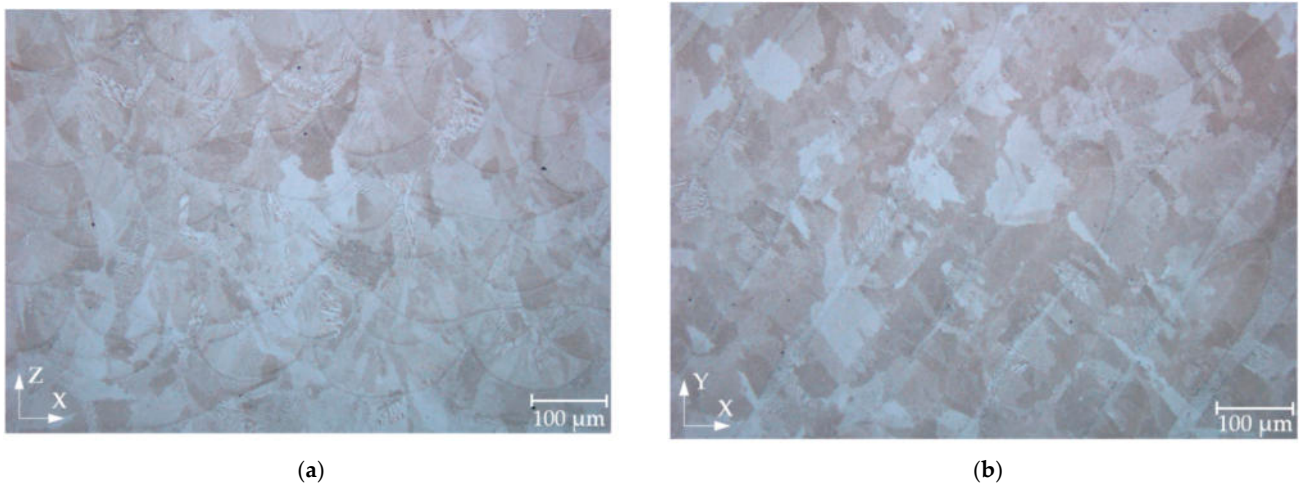


Figure 4. Light microscopy images of LPBF processed specimens fabricated using base plate preheating at 400 °C. (a) XZ plane. (b) XY plane.

Figure 5 contains enlarged microstructure images that were used to measure the width of columnar grains. The columnar grain width is also shown in Figure 6b. Enlarged SEM images were taken near the upper and bottom surfaces of the etched BCM specimens. No clear differences were detected in the upper and bottom locations. Therefore, the mean values were used. Measured data showed that the preheating temperature leads to wider columnar grains. The mean columnar width increased from $0.71 \pm 0.15 \mu\text{m}$ when RT was used as a preheating temperature to $0.75 \pm 0.11 \mu\text{m}$ for 200 °C and to $0.82 \pm 0.07 \mu\text{m}$ for 400 °C (Figure 7b).

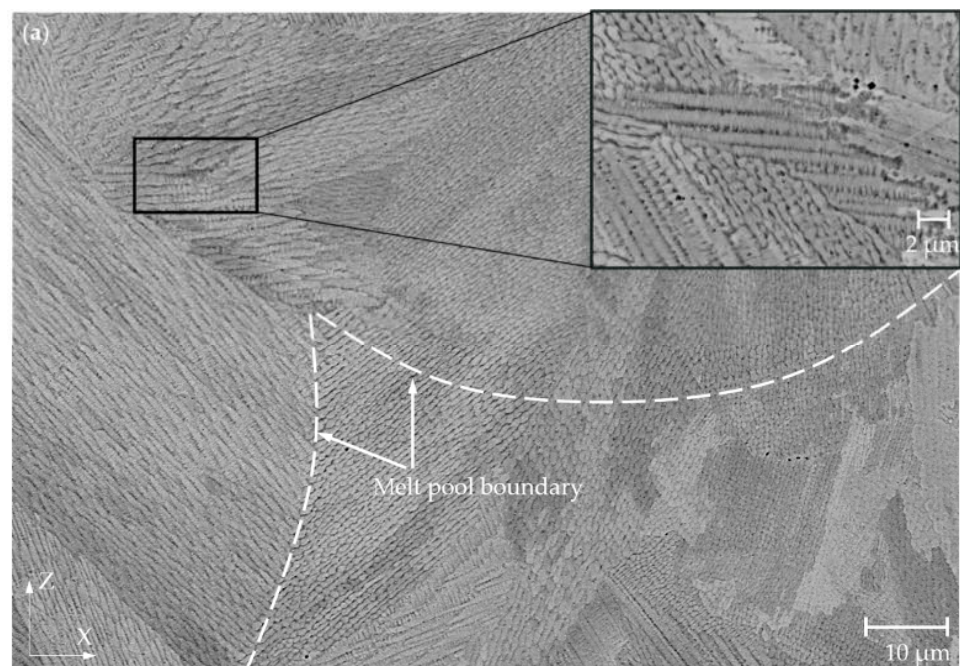


Figure 5. Cont.

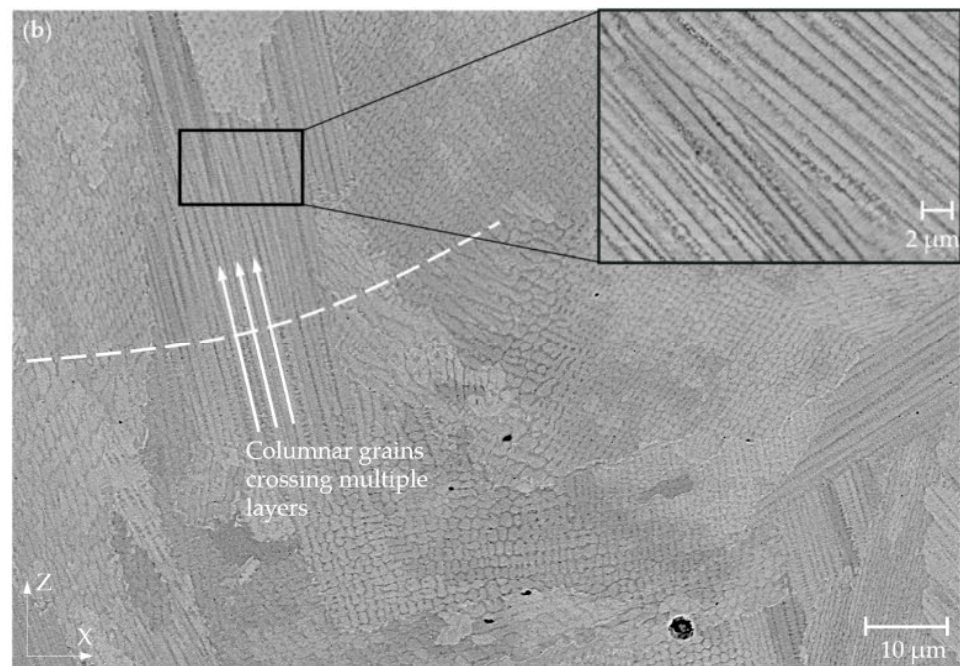


Figure 5. SEM-BSE microstructure of IN939 specimens fabricated at different preheating temperatures. (a) XZ plane of the RT specimen and (b) XZ plane of the specimen with a base plate preheated at 400 °C.

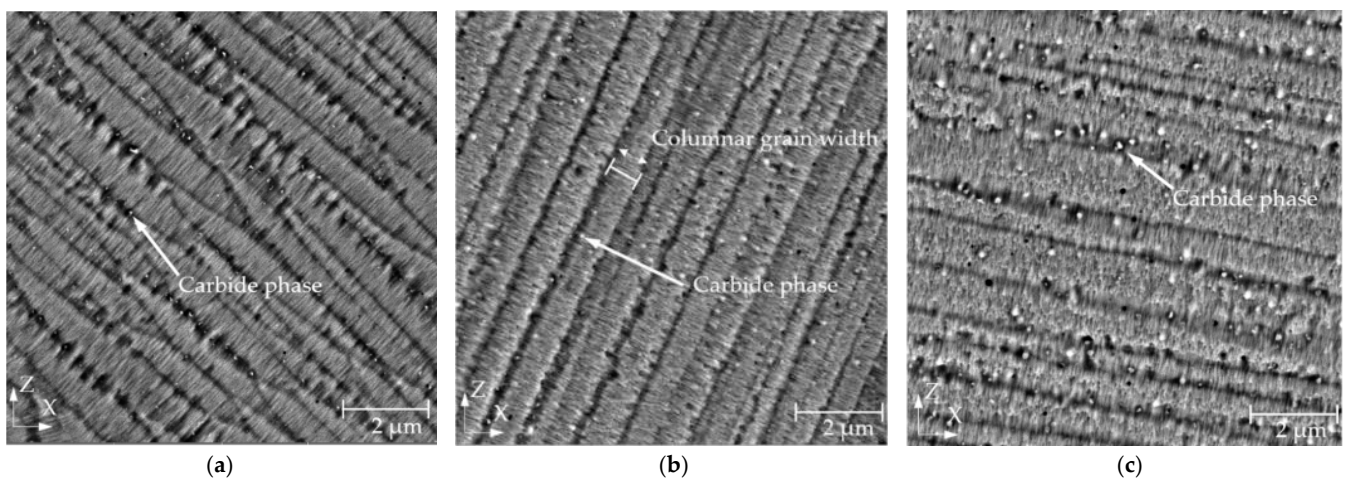


Figure 6. SEM-BSE microstructure of IN939 specimens fabricated at different preheating temperatures showing a gradual increase of the size and amount of the carbide phase (white dots). (a) XZ plane of the RT specimen; (b) XZ plane of the specimen with a base plate preheated at 200 °C; (c) XZ plane of the specimen with a base plate preheated at 400 °C.

The results of the metallographic analysis of the specimens fabricated under different preheating conditions showed significant differences in the amount and size of the carbide phase present (Figure 6).

For all specimens, the most frequent occurrence of the carbide phase was observed near the base plate (Figure 7a). Its amount and size continuously decreased toward the surface of the specimens. The most significant decrease in the occurrence of the carbide phase per area was in the specimen fabricated using 400 °C preheating, where it decreased from $1.87 \pm 0.68 \mu\text{m}^{-2}$ at the bottom to $1.17 \pm 0.20 \mu\text{m}^{-2}$ at the top. That is, a decrease of about 37.8%. At preheating at 200 °C the occurrence of the carbide phase per area decreased from $1.22 \pm 0.31 \mu\text{m}^{-2}$ about 18.1% to $1.00 \pm 0.08 \mu\text{m}^{-2}$ at the top, while when RT was

used for fabrication, the drop was 10.0% from $1.29 \pm 0.40 \mu\text{m}^{-2}$ at the bottom part of the BCM specimen to $1.16 \pm 0.39 \mu\text{m}^{-2}$ at the top.

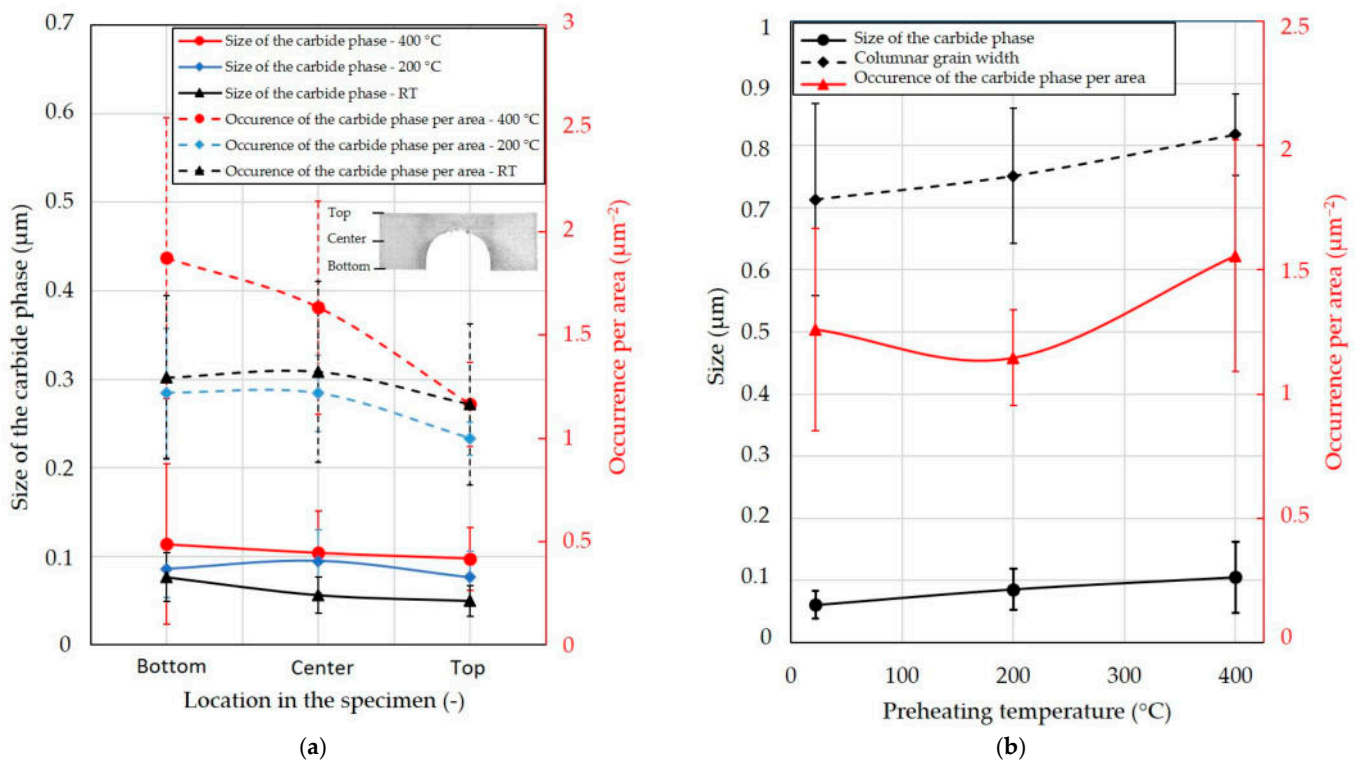


Figure 7. The effect of location in the specimen and preheating temperature on microstructure properties of IN939 fabricated at different preheating temperatures. (a) Effect of location in the specimen on the size and occurrence per area of carbide phase. (b) Effect of preheating temperature on the columnar grain width, size, and occurrence per area of the carbide phase.

The size of the carbide phase decreased in the case of preheating at $400\text{ }^{\circ}\text{C}$ from $0.114 \pm 0.091 \mu\text{m}$ at the bottom to $0.097 \pm 0.035 \mu\text{m}$ at the top, which is a decrease of 14.6% . In case of preheating at $200\text{ }^{\circ}\text{C}$, the size of the carbide phase decreased from $0.086 \pm 0.033 \mu\text{m}$ at the bottom to $0.077 \pm 0.030 \mu\text{m}$ at the top, which is a decrease of 11.0% . The largest decrease in the size of the carbide phase was observed at RT. In that case, the decrease was about 35.2% from $0.077 \pm 0.027 \mu\text{m}$ at the bottom to $0.050 \pm 0.017 \mu\text{m}$ at the top.

The preheating led to an increase in the mean size and occurrence of the carbide phase (Figure 7b). The mean size of the carbide phase increased from $0.061 \pm 0.022 \mu\text{m}$ at RT to $0.086 \pm 0.033 \mu\text{m}$ at preheating at $200\text{ }^{\circ}\text{C}$ and $0.105 \pm 0.058 \mu\text{m}$ at preheating at $400\text{ }^{\circ}\text{C}$.

The occurrence of the carbide phase also increased with the preheating temperature of $400\text{ }^{\circ}\text{C}$ to $1.56 \pm 0.47 \mu\text{m}^{-2}$ compare to RT (Figure 7b). However, at preheating at $200\text{ }^{\circ}\text{C}$, the occurrence of the carbide phase first dropped to $1.15 \pm 0.19 \mu\text{m}^{-2}$ compared to RT, where $1.26 \pm 0.41 \mu\text{m}^{-2}$ was measured.

3.3. Mechanical Properties

Figure 8 shows tensile properties of IN939 specimens as a function of the preheating temperature. The tensile properties did not change significantly compared to the RT and $200\text{ }^{\circ}\text{C}$. At RT the measured ultimate tensile strength, 0.2% proof stress, and elongation at break were $1074 \pm 23 \text{ MPa}$, $821 \pm 9 \text{ MPa}$, and $29.4 \pm 2.6\%$, respectively, while at $200\text{ }^{\circ}\text{C}$, the properties were $1062 \pm 21 \text{ MPa}$, $810 \pm 12 \text{ MPa}$, and $33.4 \pm 2.2\%$, respectively. However, when preheating was applied at $400\text{ }^{\circ}\text{C}$, the ultimate tensile strength and 0.2% proof stress increased significantly to $1341 \pm 2 \text{ MPa}$ and $1035 \pm 1 \text{ MPa}$, while elongation at break dropped to $15.1 \pm 0.9\%$. The preheating temperature of $400\text{ }^{\circ}\text{C}$ compared to RT led to an

increase in the ultimate tensile strength and 0.2% proof stress by 25% and 26%, respectively, while the elongation at break was reduced by 48.8%.

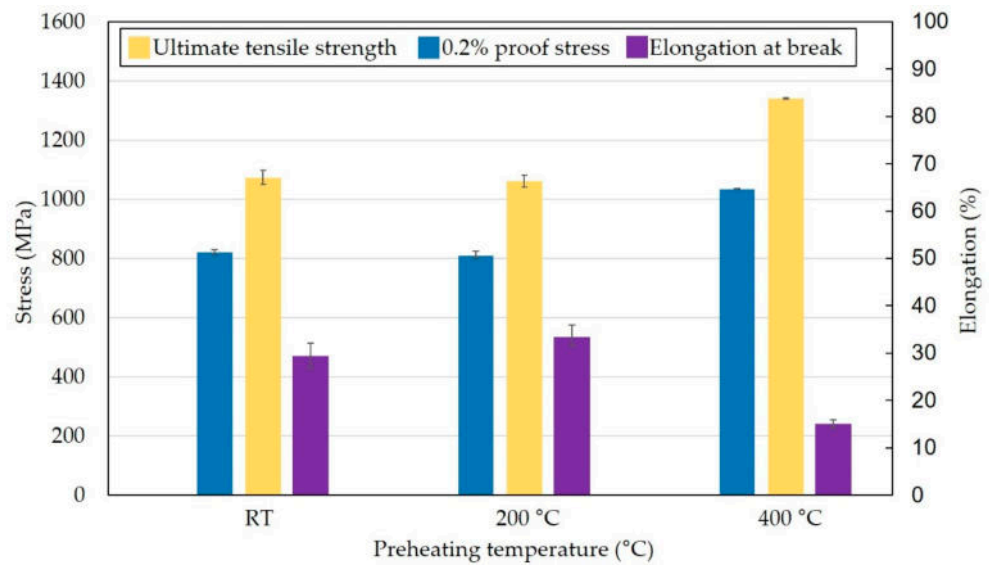


Figure 8. IN939 tensile properties of the specimens produced using RT and base plate preheating at 200 °C and 400 °C.

Figure 9 shows the mean of measured hardness values in the three lines in the direction of the Z-axis on the BCM specimens. Specimens that were fabricated at RT and preheated to 200 °C showed very similar hardness values that in the mean value was 321 ± 26 HV 1 and 326 ± 19 HV 1. The specimen with the base plate preheated at 400 °C had a significantly higher mean hardness value of 359 ± 22.5 HV 1 that is an increase of 11.8% compared to RT. The hardness values had an approximately constant character measured on the Z-axis (building direction). However, the hardness near the top surface increased for all BCM specimens.

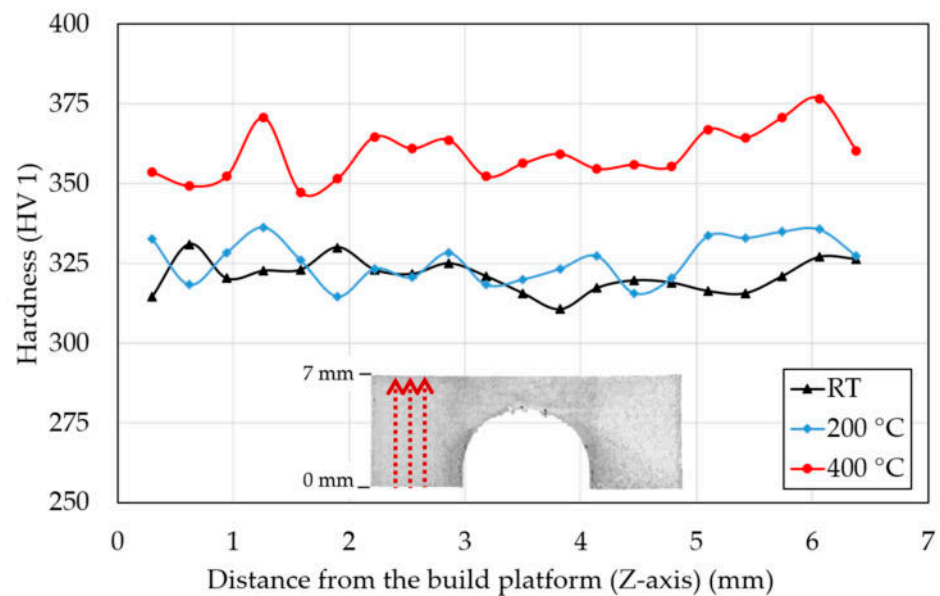


Figure 9. IN939 hardness of the BCM specimens produced using RT and base plate preheating at 200 °C and 400 °C.

3.4. Effect of Powder Bed Preheating on Unfused Powder

The EDX and XRD were used to determine the influence of high-temperature preheating on the unfused powder. Powder specimens were taken directly from the base plate after each production run. The EDX analysis of the unfused powder revealed that the effect of base plate preheating on the main elements of the chemical composition was negligible (Tables 1 and 3). However, the intensity peaks showed an increased amount of oxygen in the unfused powder within the production run using 400 °C base plate preheating (Figure 10b) compared to the virgin powder (Figure 10a). The EDX analysis was performed with the same settings for detection figures as a comparative method between the two powder conditions and, in this case, cannot be expressed qualitatively. Furthermore, no oxides were detected in the unfused powder during the XRD analysis (Figure 11). Therefore, it can be assumed that preheating the base plate to 400 °C led to increased oxidation of the unfused powder, but the quantity of oxides did not exceed the XRD detection limit of 2 wt. %. No powder agglomerations were detected in the SEM images.

Table 3. Chemical composition of IN939 unfused powder used at 200 °C and 400 °C preheating temperatures measured using EDX in weight percentage (wt. %).

	Ni	Cr	Co	Ti	W	Al	Ta	Nb
Base plate preheating of 200 °C	52.03 ± 0.30	19.60 ± 0.25	18.40 ± 0.55	3.80 ± 0.20	1.83 ± 0.20	1.53 ± 0.15	1.43 ± 0.15	0.93 ± 0.15
Base plate preheating of 400 °C	51.77 ± 1.00	19.67 ± 0.40	17.93 ± 0.60	3.73 ± 0.10	1.97 ± 0.10	1.67 ± 0.10	1.47 ± 0.15	0.83 ± 0.20

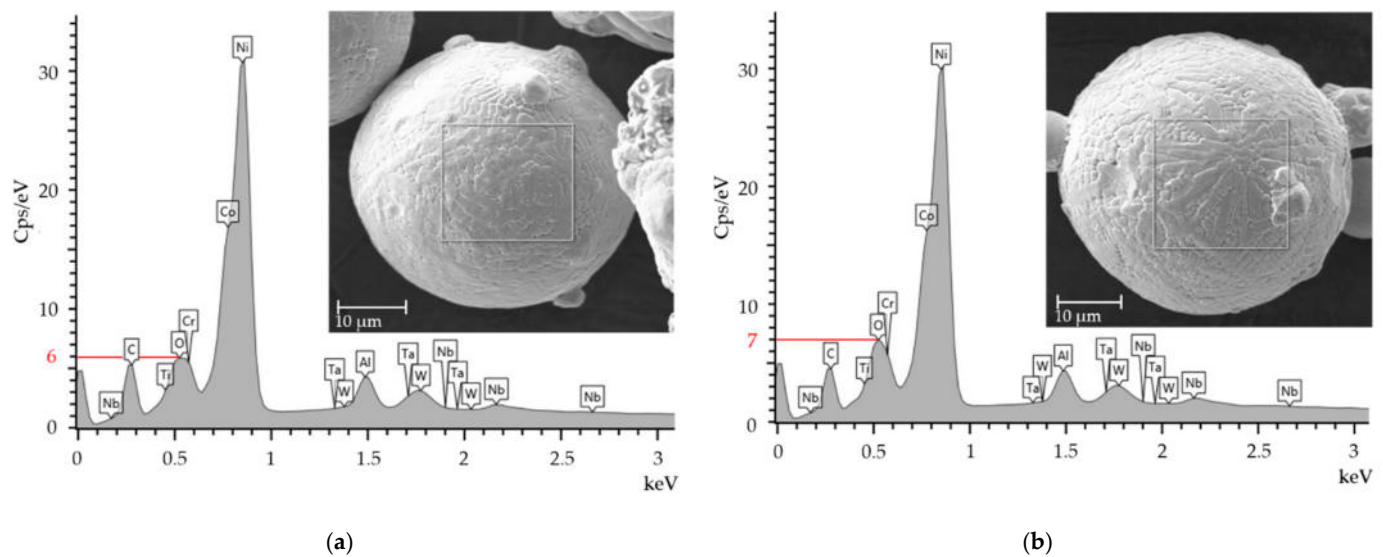


Figure 10. EDX analysis of the IN939 powder before and after using at high-temperature preheating. The white rectangle on powder grains symbolise the measured area. (a) Unused virgin powder; (b) used powder with the base plate preheated at 400 °C for 2 h.

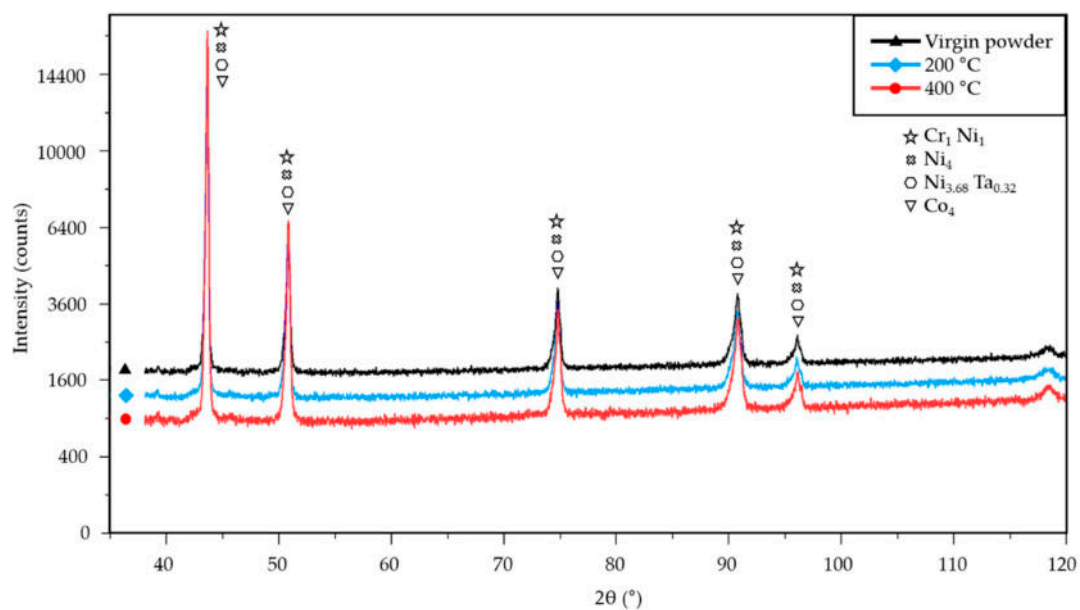


Figure 11. XRD analysis of the IN939 unfused powder in the three conditions: unused virgin powder, powder used at 200 °C, and powder used at 400 °C.

4. Discussion

The deformation results introduced in the previous section showed that a higher preheating temperature resulted in a higher deformation of the BCM specimens. Maximum deformations increased compared to RT and preheating of 200 °C and 400 °C to 0.01 mm and 0.04 mm, respectively, which are increases of 4.2% and 16.2% (Figure 3). The results showed that higher preheating temperatures led to higher deformations. It should be noted that the deformation results for each preheating temperature are composed of two specimens fabricated in the 0° and 90° directions according to the recoating direction of the powder. Specimens in both directions had a similar behavior (Table 2). The difference in the top surface distortion of the specimens produced in the 0° and 90° directions was 0.1 mm. This is a significant value and is attributed to the rotation of the meander scanning strategy. The limitation window parameter set in the scanning strategy caused the vectors along the gas flow direction to be skipped, resulting in an overall reduction in the length of the vectors on specimens oriented in the transverse direction (90°). Therefore, the measured distortions were lower.

The values of the top surface distortions are in contradiction with the results for materials such as titanium and aluminum alloys [15,22]. RSs of nickel-based alloy IN718 were studied under preheating conditions in the range of (50–150) °C [30]. The results showed that the higher preheating temperature led to decrease of σ_z residual stresses by 22%. However, the σ_x stresses increased from 68 MPa to 77 MPa, which is an increase of 13%. Mirkoohi et al. [23] experimentally validated that RS of IN718 gradually decreases when preheating up to 200 °C is applied [23]. However, he also predicted through simulation that preheating temperatures in the range of (250–500) °C will increase RS. The increase in RS in the study [23] was explained as a consequence of the reduced yield strength due to the coarsening of the grains. The specimens in study [23] and also in this paper were produced with the same laser-related process parameters, and powder bed preheating was the only parameter that was changed. Therefore, it can be assumed that excess heat accumulated in the manufactured specimens.

The impact of base plate preheating on relative density was not detected and all specimens showed relative density close to 100%. The width of the melt pool increased by 35 μm when comparing the RT and the preheated specimens at temperature of 400 °C. These results correspond to the study of IN718, which showed that a larger width of the melt pool and a larger melt volume can be expected with a higher preheating temperature [23].

The microstructure studied in the etched state consists of a typical microstructure of melt pools observed in LPBF processed specimens [11,28]. The SEM analysis showed a very fine cellular/dendritic microstructure with columnar grains in all cases. The very fine cellular structure is the result of the high solidification rate due to the rapid scanning of the laser beam [29]. Columnar grains (elongated along the build direction) grew during crystallisation of the material. Several columnar grains passed through a few melt pools, leading to a stronger bond between the layers [31,32]. The frequency of occurrence of the columnar grains decreased with increasing preheating temperature. The specimens with higher preheating had a lower occurrence of columnar grains, which may be due to the reduction of the thermal gradient. The IN718 study showed that preheating at 150 °C reduces the thermal gradients, thus affecting the orientation of fine grains. The grains, checked using electron backscatter diffraction analysis, were also more randomly oriented and smaller by 19 µm under preheating temperature of 150 °C compared to 50 °C [30]. The decrease in the thermal gradient can also contribute to the columnar-to-equiaxial transition [33]. Thus, the occurrence of columnar grains in this study of IN939 decreased. However, reduced thermal gradients lead to a slower cooling rate and can increase cell spacing [34]. The mean columnar grain width of IN939 increased by 16% compared to the RT and the preheating temperature of 400 °C (Figure 7b). Variation in microstructure directly affects the mechanical properties of the material [35,36]. However, the mechanical properties of the IN939 are also influenced by evolution of the carbide phase.

The tensile test showed an increase in 0.2% proof stress and ultimate tensile strength by 26% and 25%, respectively, while elongation at break was reduced by 48.8% when comparing RT and preheating at 400 °C (Figure 8). However, the tensile properties were studied in specimens fabricated in horizontal direction. Vertically fabricated specimens can exhibit different behavior when mechanical properties depend on microstructure, which in LPBF technology is strongly influenced by building direction.

The trend of mean hardness values corresponds to the distortion and mechanical properties of the measured specimens. RT and preheating at 200 °C did not cause significant change. However, preheating at 400 °C increased the mean hardness of the BCM specimens to 359 ± 22.5 HV 1, which is higher by 11.8% compared to RT. The hardness was measured in the building direction through the whole BCM, which showed a nearly constant character. However, the values near the top surface increased. Hardness measurement is affected by RS [37]. In additively manufactured IN718 and 316 L stainless steel, RS was detected to be higher near the top of the specimens [23,38] due to the absence of reheating from the fuse of the upper layers. This zone is called the transition area between the outer and inner surfaces [38]. Therefore, the increase in hardness values near the top surface can be explained by the increase in RS [23].

The mechanism that plays a significant role in the mechanical properties of nickel-based alloys is its strengthening, which is usually acquired by precipitation-hardening heat treatment. A higher preheating temperature leads to a longer solidification time of the material [39]. It can be assumed that with a longer crystallization time, the percentage of γ' hardening precipitates and carbides, which affect mechanical properties, increases [30,40,41]. Precipitates influence the mechanical properties of the IN939 alloy [11], and high-temperature preheating can lead to its evolution during fabrication. The precipitates were detected by SEM-BSE images where they appeared as white dots formed mainly between grains (Figure 6). Based on location, contrast, and size, they should be composed of MC-type carbides [12,42], which was in additively manufactured IN939 confirmed by transmission electron microscopy [41]. Their size and occurrence gradually increased together with preheating. The average carbide size and its occurrence per area increased by 72.4% and 23.6%, respectively, when comparing RT and preheating at 400 °C (Figure 7b). Furthermore, a significant effect of location on the specimens on the carbide phase was detected. As the distance from the building plate increased, the size and occurrence of the carbide phase decreased for all preheating temperatures. The most significant effect was observed when preheating at 400 °C was used. The average grain size and occurrence per

area decreased by 14.6% and 37.8% compared to the bottom and upper part of the specimen. This result shows that the build time had a significant effect on the microstructure of the material and, thus, the mechanical properties.

The resulting specimens exhibit higher hardness, ultimate tensile strength, and 0.2% proof stress but lower elongation at break. The different amounts and sizes of the carbide phase in the individual specimens fully correspond to the results of the hardness, tensile test, and deformations caused by the RS. The different temperature gradient in samples with different heights of preheating of the build plate resulted in different kinetics of the precipitation processes associated with the formation of a completely different crystallographic lattice of the carbide phase. Subsequently, precipitate formation is the cause of the increase in the internal RS level of the material.

EDX and XRD analyses showed that a higher preheating led to a slight increase in the quantity of oxides in the unfused powder. However, the oxide content did not exceed the minimum detectable value of 2 wt. % of the XRD method. The oxidation of the unfused powder does not directly affect the oxide content in the bulk material [24].

5. Conclusions

In this study, the effects of high-temperature preheating on deformation and indirectly on the residual stress, macrostructure, microstructure, mechanical properties, and properties of the unfused powder of Inconel 939 were investigated. The main conclusions are as follows:

- Higher preheating of the base plate led to an increase in the deformation of the top surface of the bridge curvature method specimens and thus to a higher residual stress. The increase in internal residual stress corresponds to the intensity of the precipitation process in the carbide phase.
- The higher temperature of the base plate resulted in a larger melt pool, increased columnar grain width, and increased the amount and size of the carbide phase.
- The use of higher preheating temperatures led to an increase in the hardness, ultimate tensile strength, and 0.2% proof stress but decreased the elongation at break due to an increase in the amount and size of the carbide phase.
- The build time had a significant effect on the formation of precipitates when high-temperature preheating was used.
- Rapid oxidation of unfused powder was not detected with the EDX and XRD methods.

Author Contributions: Conceptualization, M.M.; data curation, M.M., K.N., L.K. and O.A.; formal analysis, M.M.; funding acquisition, L.P. and D.K.; investigation, M.M., K.N., L.K. and O.A.; methodology, M.M. and K.N.; supervision, L.K., L.P. and D.K.; validation, L.K., L.P. and D.K.; visualization, M.M. and K.N.; writing—original draft, M.M. and K.N.; writing—review and editing, L.K., O.A. and D.K. All authors have read and agreed to the published version of the manuscript.

Funding: This research was supported by Brno University of Technology Faculty of Mechanical Engineering Specific research projects [No. FSI-S-20-6296 and FSI-S-20-6290].

Institutional Review Board Statement: Not applicable.

Informed Consent Statement: Not applicable.

Conflicts of Interest: The authors declare no conflict of interest.

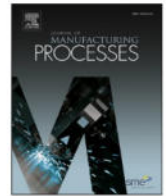
Abbreviations

AM—additive manufacturing; BCM—bridge curvature method; EBM—electron beam melting; EDX—energy-dispersive X-ray spectroscopy; IN939—Inconel 939; IN718—Inconel 718; LPBF—laser powder bed fusion; PBF—powder bed fusion; RS—residual stress; RT—room temperature; SEM—scanning electron microscope; XRD—X-ray diffraction.

References

1. Beaman, J.J.; Deckard, C.R. Selective Laser Sintering with Assisted Powder Handling. U.S. Patent 4,938,816, 3 July 1990.
2. Kruth, J.P.; Froyen, L.; van Vaerenbergh, J.; Mercelis, P.; Rombouts, M.; Lauwers, B. Selective Laser Melting of Iron-Based Powder. *J. Mater. Process Technol.* **2004**, *149*, 616–622. [[CrossRef](#)]
3. Gu, D.D.; Meiners, W.; Wissenbach, K.; Poprawe, R. Laser Additive Manufacturing of Metallic Components: Materials, Processes and Mechanisms. *Int. Mater. Rev.* **2012**, *57*, 133–164. [[CrossRef](#)]
4. DebRoy, T.; Wei, H.L.; Zuback, J.S.; Mukherjee, T.; Elmer, J.W.; Milewski, J.O.; Beese, A.M.; Wilson-Heid, A.; De, A.; Zhang, W. Additive Manufacturing of Metallic Components—Process, Structure and Properties. *Prog. Mater. Sci.* **2018**, *92*, 112–224. [[CrossRef](#)]
5. Zhuang, J.-R.; Lee, Y.-T.; Hsieh, W.-H.; Yang, A.-S. Determination of melt pool dimensions using DOE-FEM and RSM with process window during SLM of Ti6Al4V powder. *Opt. Laser Technol.* **2018**, *103*, 59–76. [[CrossRef](#)]
6. Schleifenbaum, J.H.; Meiners, W.; Wissenbach, K.; Hinke, C. Individualized production by means of high power Selective Laser Melting. *CIRP J. Manuf. Sci. Technol.* **2010**, *2*, 161–169. [[CrossRef](#)]
7. Campbell, I.; Diegel, O.; Kowen, J.; Wohlers, T. *Wohlers Report 2018: 3D Printing and Additive Manufacturing State of the Industry: Annual Worldwide Progress Report*; Wohlers Associates: Collins, CO, USA, 2018; ISBN 0991333241.
8. Bartlett, J.L.; Li, X. An overview of residual stresses in metal powder bed fusion. *Addit. Manuf.* **2019**, *27*, 131–149. [[CrossRef](#)]
9. Sanchez, S.; Smith, P.; Xu, Z.; Gaspard, G.; Hyde, C.J.; Wits, W.W.; Ashcroft, I.A.; Chen, H.; Clare, A.T. Powder Bed Fusion of nickel-based superalloys: A review. *Int. J. Mach. Tools Manuf.* **2021**, *165*, 103729. [[CrossRef](#)]
10. Warren, J.; Wei, D.Y. The cyclic fatigue behavior of direct age 718 at 149, 315, 454 and 538 °C. *Mater. Sci. Eng. A* **2006**, *428*, 106–115. [[CrossRef](#)]
11. Kanagarajah, P.; Brenne, F.; Niendorf, T.; Maier, H.J. Inconel 939 processed by selective laser melting: Effect of microstructure and temperature on the mechanical properties under static and cyclic loading. *Mater. Sci. Eng. A* **2013**, *588*, 188–195. [[CrossRef](#)]
12. Donachie, M.J.; Donachie, S.J. *Superalloys: A Technical Guide*, 2nd ed.; ASM International: Materials Park, OH, USA, 2002; ISBN 978-0871707499.
13. Zhang, B.; Li, Y.; Bai, Q. Defect Formation Mechanisms in Selective Laser Melting: A Review. *Chin. J. Mech. Eng. Engl. Ed.* **2017**, *30*, 515–527. [[CrossRef](#)]
14. Withers, P.J.; Bhadeshia, H.K.D.H. Residual Stress. Part 1—Measurement Techniques. *Mater. Sci. Technol.* **2001**, *17*, 355–365. [[CrossRef](#)]
15. Malý, M.; Höller, C.; Skalon, M.; Meier, B.; Koutný, D.; Pichler, R.; Sommitsch, C.; Paloušek, D. Effect of Process Parameters and High-Temperature Preheating on Residual Stress and Relative Density of Ti6Al4V Processed by Selective Laser Melting. *Materials* **2019**, *12*, 930. [[CrossRef](#)] [[PubMed](#)]
16. Benedetti, M.; Torresani, E.; Leoni, M.; Fontanari, V.; Bandini, M.; Pederzoli, C.; Potrich, C. The effect of post-sintering treatments on the fatigue and biological behavior of Ti-6Al-4V ELI parts made by selective laser melting. *J. Mech. Behav. Biomed. Mater.* **2017**, *71*, 295–306. [[CrossRef](#)] [[PubMed](#)]
17. Li, C.; Liu, Z.Y.; Fang, X.Y.; Guo, Y.B. Residual Stress in Metal Additive Manufacturing. *Procedia CIRP* **2018**, *71*, 348–353. [[CrossRef](#)]
18. Sochalski-Kolbus, L.M.; Payzant, E.A.; Cornwell, P.A.; Watkins, T.R.; Babu, S.S.; Dehoff, R.R.; Lorenz, M.; Ovchinnikova, O.; Duty, C. Comparison of Residual Stresses in Inconel 718 Simple Parts Made by Electron Beam Melting and Direct Laser Metal Sintering. *Met. Mater. Trans. A* **2015**, *46*, 1419–1432. [[CrossRef](#)]
19. Ali, H.; Ghadbeigi, H.; Mumtaz, K. Residual Stress Development in Selective Laser-Melted Ti6Al4V: A Parametric Thermal Modelling Approach. *Int. J. Adv. Manuf. Technol.* **2018**, *97*, 2621–2633. [[CrossRef](#)]
20. Vrancken, B.; Wauthle, R.; Kruth, J.-P.; van Humbeeck, J. Study of the Influence of Material Properties on Residual Stress in Selective Laser Melting. In Proceedings of the 24th International Solid Freeform Fabrication Symposium, Austin, TX, USA, 12–14 August 2013; pp. 393–407. [[CrossRef](#)]
21. Denlinger, E.R.; Heigel, J.C.; Michaleris, P.; Palmer, T.A. Effect of inter-layer dwell time on distortion and residual stress in additive manufacturing of titanium and nickel alloys. *J. Mater. Process. Technol.* **2015**, *215*, 123–131. [[CrossRef](#)]
22. Ali, H.; Ma, L.; Ghadbeigi, H.; Mumtaz, K. In-situ residual stress reduction, martensitic decomposition and mechanical properties enhancement through high temperature powder bed pre-heating of Selective Laser Melted Ti6Al4V. *Mater. Sci. Eng. A* **2017**, *695*, 211–220. [[CrossRef](#)]
23. Mirkoohi, E.; Liang, S.Y.; Tran, H.C.; Lo, Y.L.; Chang, Y.C.; Lin, H.Y. Mechanics Modeling of Residual Stress Considering Effect of Preheating in Laser Powder Bed Fusion. *J. Manuf. Mater. Processing* **2021**, *5*, 46. [[CrossRef](#)]
24. Malý, M.; Koutný, D.; Pantělejev, L.; Pambaguian, L.; Paloušek, D. Effect of high-temperature preheating on pure copper thick-walled samples processed by laser powder bed fusion. *J. Manuf. Process.* **2022**, *73*, 924–938. [[CrossRef](#)]
25. Körperich, J.P.; Merkel, M. Thermographic Analysis of the Building Height Impact on the Properties of Tool Steel in Selective Laser Beam Melting. *Materwiss Werksttech* **2018**, *49*, 689–695. [[CrossRef](#)]
26. Kruth, J.P.; Deckers, J.; Yasa, E.; Wauthle, R. Assessing and Comparing Influencing Factors of Residual Stresses in Selective Laser Melting Using a Novel Analysis Method. *Proc. Inst. Mech. Eng. Part B J. Eng. Manuf.* **2012**, *226*, 980–991. [[CrossRef](#)]
27. Le Roux, S.; Salem, M.; Hor, A. Improvement of the bridge curvature method to assess residual stresses in selective laser melting. *Addit. Manuf.* **2018**, *22*, 320–329. [[CrossRef](#)]

28. Buchbinder, D.; Meiners, W.; Pirch, N.; Wissenbach, K.; Schrage, J. Investigation on reducing distortion by preheating during manufacture of aluminum components using selective laser melting. *J. Laser Appl.* **2014**, *26*, 012004. [[CrossRef](#)]
29. Lee, J.; Terner, M.; Jun, S.; Hong, H.-U.; Copin, E.; Lours, P. Heat treatments design for superior high-temperature tensile properties of Alloy 625 produced by selective laser melting. *Mater. Sci. Eng. A* **2020**, *790*, 139720. [[CrossRef](#)]
30. Park, J.-H.; Bang, G.B.; Lee, K.-A.; Son, Y.; Song, Y.H.; Lee, B.-S.; Kim, W.R.; Kim, H.G. Effect of Preheating Temperature on Microstructural and Mechanical Properties of Inconel 718 Fabricated by Selective Laser Melting. *Met. Mater. Int.* **2022**, 1–13. [[CrossRef](#)]
31. Liu, F.; Lin, X.; Huang, C.; Song, M.; Yang, G.; Chen, J.; Huang, W. The effect of laser scanning path on microstructures and mechanical properties of laser solid formed nickel-base superalloy Inconel 718. *J. Alloy. Compd.* **2011**, *509*, 4505–4509. [[CrossRef](#)]
32. Vilaro, T.; Colin, C.; Bartout, J.D.; Nazé, L.; Sennour, M. Microstructural and Mechanical Approaches of the Selective Laser Melting Process Applied to a Nickel-Base Superalloy. *Mater. Sci. Eng. A* **2012**, *534*, 446–451. [[CrossRef](#)]
33. Xu, J.; Lin, X.; Guo, P.; Hu, Y.; Wen, X.; Xue, L.; Liu, J.; Huang, W. The Effect of Preheating on Microstructure and Mechanical Properties of Laser Solid Forming IN-738LC Alloy. *Mater. Sci. Eng. A* **2017**, *691*, 71–80. [[CrossRef](#)]
34. Yadroitsev, I.; Krakhmalev, P.; Yadroitsava, I.; Johansson, S.; Smurov, I. Energy input effect on morphology and microstructure of selective laser melting single track from metallic powder. *J. Mater. Process. Technol.* **2013**, *213*, 606–613. [[CrossRef](#)]
35. Kunze, K.; Etter, T.; Grässlin, J.; Shklover, V. Texture, anisotropy in microstructure and mechanical properties of IN738LC alloy processed by selective laser melting (SLM). *Mater. Sci. Eng. A* **2015**, *620*, 213–222. [[CrossRef](#)]
36. Popovich, A.A.; Sufiarirov, V.S.; Polozov, I.A.; Borisov, E.V. Microstructure and Mechanical Properties of Inconel 718 Produced by SLM and Subsequent Heat Treatment. In *Proceedings of the Key Engineering Materials*; Trans Tech Publications Ltd.: Stafa-Zurich, Switzerland, 2015; Volume 651–653, pp. 665–670.
37. Huber, N.; Heerens, J. On the effect of a general residual stress state on indentation and hardness testing. *Acta Mater.* **2008**, *56*, 6205–6213. [[CrossRef](#)]
38. Simson, T.; Emmel, A.; Dwars, A.; Böhm, J. Residual stress measurements on AISI 316L samples manufactured by selective laser melting. *Addit. Manuf.* **2017**, *17*, 183–189. [[CrossRef](#)]
39. Zhou, X.; Liu, X.; Zhang, D.; Shen, Z.; Liu, W. Balling phenomena in selective laser melted tungsten. *J. Mater. Process. Technol.* **2015**, *222*, 33–42. [[CrossRef](#)]
40. Li, Y.; Liang, X.; Yu, Y.; Li, H.; Kan, W.; Lin, F. Microstructures and mechanical properties evolution of IN939 alloy during electron beam selective melting process. *J. Alloy. Compd.* **2021**, *883*, 160934. [[CrossRef](#)]
41. Philpott, W.; Jepson, M.A.E.; Thomson, R.C. Comparison of the Effects of a Conventional Heat Treatment between Cast and Selective Laser Melted IN939 Alloy. In *Advances in Materials Technology for Fossil Power Plants—Proceedings from the 8th International Conference*; ASM International: Materials Park, OH, USA, 2016; pp. 735–746.
42. Hagedorn, Y.C.; Risse, J.; Meiners, W.; Pirch, N.; Wissenbach, K.; Poprawe, R. Processing of Nickel Based Superalloy MAR M-247 by Means of High Temperature - Selective Laser Melting (HT-SLM). In *High Value Manufacturing: Advanced Research in Virtual and Rapid Prototyping*; CRC Press: Boca Raton, FL, USA, 2014; pp. 291–295.



Effect of high-temperature preheating on pure copper thick-walled samples processed by laser powder bed fusion

Martin Malý^{a,*}, Daniel Koutný^a, Libor Pantělejev^b, Laurent Pambaguian^c, David Paloušek^a

^a Brno University of Technology, Faculty of Mechanical Engineering, Institute of Machine and Industrial Design, Technická 2896/2, 616 69 Brno, Czech Republic

^b Brno University of Technology, Faculty of Mechanical Engineering, Institute of Materials Science and Engineering, Technická 2896/2, 616 69 Brno, Czech Republic

^c European Space Agency, ESTEC, Keplerlaan 1, PO Box 299, NL-2200 AG Noordwijk, the Netherlands

ARTICLE INFO

Keywords:

Laser powder bed fusion
Selective laser melting
Copper
Preheating
Relative density

ABSTRACT

The Laser Powder Bed Fusion (LPBF) also called Selective Laser Melting technology uses for the layer-based part fabrication laser beam as the main energy source for melting a powdered material. The processing of pure copper by LPBF technology is a challenge due to its high laser beam reflectivity, thermal conductivity and affinity to oxygen. Thus, for reaching homogeneous sample in an acceptable quality a high power Nd: YAG fibre laser sources are used. In this study, the effect of Nd: YAG fibre laser with a maximum power of 400 W and 400 °C high-temperature base plate preheating as another heat source on the relative density of pure copper thin-walled and thick-walled samples was investigated. Moreover, the effect of layer thickness, laser speed, laser velocity, hatch distance, sample width, scanning and remelting strategy was studied. Further on, the effect of powder bed preheating on the copper powder melting, laser beam reflectivity, wetting and solidification conditions and powder and part oxidation was discussed. Using the statistical methods for experimental planning the behaviour of each observed process parameter was revealed and the proper combination of process parameters was stated. It was found that for reaching relative density over 99% the process parameters should be set from observed range as following: layer thickness 0.03 mm, laser power 400 W, laser velocity 505 mm·s⁻¹, hatch distance 0.06 mm and powder bed preheating of 400 °C. Despite the high value of relative density, the issues connected with layer and track bonding attributed to thin oxide layers were not successfully eliminated.

1. Introduction

Rapid progress in additive manufacturing technologies established methods for reliable production of complex components. Thus, additive technologies were spread to the many new industrial branches which caused a higher demand for new materials development. Laser Powder Bed Fusion (LPBF) is a popular technology for production of nearly full density metallic parts. This manufacturing process is using a laser beam for the formation of near net shape parts from powdered material. The layer-based production of the 3D object is realized by laser melting of the powder in the individual cross-sections. The manufactured components are composed of stacked and fully connected layers. The process takes place in an inert atmosphere. The finalized parts have, thanks to

the fully melting, mechanical properties comparable to the ones produced by conventional techniques. [1–3]

Copper is a metallic material with excellent thermal and electrical conductivity properties. Thus, it is desired material for heat exchangers, induction heat coils or radiofrequency cathodes [4]. Connecting the excellent copper properties with the new manufacturing opportunities, offered by the LPBF technology, will lead to the production of even more complex and efficient parts. However, the processing of pure copper by laser-based additive manufacturing is a challenge. Issues are connected with the high laser beam reflectivity, thermal conductivity and copper affinity to the oxygen [5–8]. Theoretical laser absorptivity for copper bulk material is around 2–6% for the fibre lasers with a wavelength of around 1064 nm [9]. However, measured laser absorptivity of copper

Abbreviations: LPBF, Laser Powder Bed Fusion; LP, laser power; LV, laser velocity; HD, hatch distance; LT, layer thickness; SW, sample width; RD, relative density; SEM, Scanning Electron Microscope; SRD, Surface Response Design; FFD, Fractional Factorial Design; EDS, Energy-dispersive X-ray spectroscopy; XRD, X-ray diffraction.

* Corresponding author.

E-mail addresses: Martin.Maly2@vut.cz (M. Malý), Daniel.Koutny@vut.cz (D. Koutný), Pantelejev@fme.vutbr.cz (L. Pantělejev), Laurent.pambaguian@esa.int (L. Pambaguian), David.Palousek@vut.cz (D. Paloušek).

<https://doi.org/10.1016/j.jmapro.2021.11.035>

Received 22 June 2021; Received in revised form 16 November 2021; Accepted 16 November 2021

Available online 8 December 2021

1526-6125/© 2021 The Society of Manufacturing Engineers. Published by Elsevier Ltd. All rights reserved.

powder used in Jadhav et al. study was 29% [10] because of a multi incident beam interactions [11,12]. High thermal conductivity causing rapid heat dissipation from the melt pool and decreasing solidification time. In combination with the relatively long time required for the melt pool spreading it may result in the balling phenomenon [13]. Further on, rapid heat dissipation from the melt pool leads to high temperature gradient in the molten pool and differences in the heat expansion resulting in the formation of cracks [14].

Processing of pure copper via LPBF was studied by many authors which at the beginning used low power fibre lasers and reached highly porous structures with a relative density lower than 90% [7,15–18]. Constantin et al. [19], using 400 W fibre laser, have found a very narrow span of process parameters leading to the relative density of 95%. Less than 5% porosity of pure copper parts offer some industrial companies [20,21].

As an effort to overcome the issue with high reflectivity and thermal conductivity researchers used high power laser beams up to 1 kW. Ike-shoji et al. [22] reached the relative density of 96.6% using laser power of 800 W. Colopi et al. [23] observed a full range of the main process parameters (laser power, laser velocity and layer thickness) and established process window for a stable process with no evident defects. Maximum relative density was 97.8%. Jadhav et al. [24] reported relative density higher than 98% with an energy density of 740–1120 J·mm⁻³. However, a combination of high laser power of 600 W and 800 W and highly reflective copper led to a breakage of the dielectric coating on the optical mirror.

To increase energy consumption delivered from the laser source, green lasers with a lower wavelength of 515 nm were used [25]. Green or blue lasers introduced for copper welding have much higher laser energy absorption [26–28] and could lead to increased production ability of pure copper parts by powder bed fusion. Hori et al. [29] using 200 W blue diode laser processed samples with the relative density of 99.1%.

Laser energy absorption could be increased by alloying pure copper. Paloušek et al. [30] reached relative density higher than 99% with alloy Cu7.2Ni1.8Si1Cr, reporting that the processing window starts from laser power of 250 W. Nevertheless, alloying of copper may lead to a sharp decrease in the thermal and electrical conductivity [10,31]. Another approach for improving laser absorptivity was proposed by Jadhav et al. [10]. By mixing the pure copper powder with 0.1% of carbon nanoparticles increased the optical absorption from 29% to 67%. With this technique, the necessary energy density was lowered to (200–500) J·mm⁻³ for reaching relative density above 98%. Nevertheless, the author used laser power above 725 W and internal cracks and low mechanical properties were detected. Jadhav et al. [32] modified the surface of CuCr1 alloy by the outward diffusion of chromium in a nitrogen atmosphere, which resulted in two times higher laser absorptivity and 20% less energy required, compared to the CuCr1 virgin powder, for forming dense parts with the relative density of 99.1%.

From the presented overview it is clear that the reflectivity of the laser energy is the main barrier for copper processing using LPBF. The researchers, so far, were mainly focused on optimizing and increasing laser power or modification of the powder composition for reaching highly homogeneous samples with high relative density. The energy necessary for the proper melting process could be also delivered by a powder bed preheating [33–36]. The preheating of the powder before the melting process should decrease the energy required from the laser source and allow to use a less powerful laser source. High-temperature preheating of copper and other materials also leads to decrease their laser reflectivity [37–39] and amount of induced residual stresses [36,40,41].

Thus, this study is mainly devoted to assessing the influence of the high-temperature powder bed preheating for reaching low porosity thick-walled samples made of pure copper. The preheating was combined with variable laser power (LP), laser velocity (LV), hatch distance (HD), layer thickness (LT), sample width (SW), remelting strategies and

Table 1

Chemical composition of pure copper delivered by the supplier.

Cu (wt %)	As (ppm)	Bi (ppm)	S (ppm)	Sb (ppm)	Ag (ppm)	Mg (ppm)	P (ppm)
Bal.	<20	<20	<20	<15	<10	<10	<10
Pb (ppm)	Si (ppm)	Sn (ppm)	Zn (ppm)	Al (ppm)	Cd (ppm)	Co (ppm)	Cr (ppm)
<10	<10	<10	<10	<5	<5	<5	<5
Fe (ppm)			Mn (ppm)		Ni (ppm)		
<5			<5		<5		

laser scanning strategies. The main goal was to find the process parameters for reaching maximum relative density (RD).

2. Materials and methods

2.1. Powder characterization

A copper powder of 99.95% purity (Safina a.s., Vestec, Czech Republic) was used in this study. The purity of copper was checked by an ICP-OES method, where the maximum measured amount of impurities was 90 ppm in total (Table 1). The used gas atomization manufacturing method produced powder with mostly spherical particles (Fig. 1a). Particles shape were analyzed by Scanning Electron Microscope (SEM) Ultra-Plus 50 (Carl Zeiss AG, Oberkochen, Germany). The particle size distribution analysis was performed by laser diffraction analyser LA-960 (Horiba, Kyoto, Japan). The mean particle size was 25.9 µm and median size 25.7 µm. The particles up to 22.8 µm represented 10% of particle distribution while particles up to 29.4 µm represented 90% (Fig. 1b).

2.2. Experimental procedure

All LPBF experiments were conducted in the SLM 280^{HL} (SLM Solutions Group AG, Lübeck, Germany) 3D printer equipped with 400 W ytterbium fibre laser YLR-400-WC-Y11 (IPG Photonics, Oxford, USA) with a focus diameter of 82 µm and a Gaussian shape power distribution. Nitrogen was used as a protective gas. The O₂ content of the inert atmosphere was kept below 0.2%. The powder humidity, measured before each experiment by the hydro thermometer Hytelog (B + B Thermo-Technik GmbH, Donaueschingen, Germany), was 5 ± 2%. The powder bed preheating up to 200 °C was realized by a heating system build-in the SLM machine. For the preheating to temperatures higher than 200 °C, an in-house manufactured heating device was used. The resistive heating elements in this heating device can preheat a top surface of the building platform up to 600 ± 10 °C. The temperature is controlled by a PID regulator and by a thermocouple placed below the base plate. The temperature of a printed component may be slightly lower than the measured temperature. Especially high components could have a lower temperature on the build surface [42] but in this study was printed components with maximum 10 mm in height and copper has high thermal conductivity. Therefore, the temperature field should be relatively homogeneous. The device was calibrated before the start of the printing process by measuring the build surface temperature and its dependency on the set temperature on the PID regulator. The samples were printed on a base plate made of copper of commercial purity and removed using wire electro-discharge machining. No additional post-processing was used.

Five production runs have been produced. Fig. 2 shows the schema of each production run sorted by chronology, sample type and process conditions.

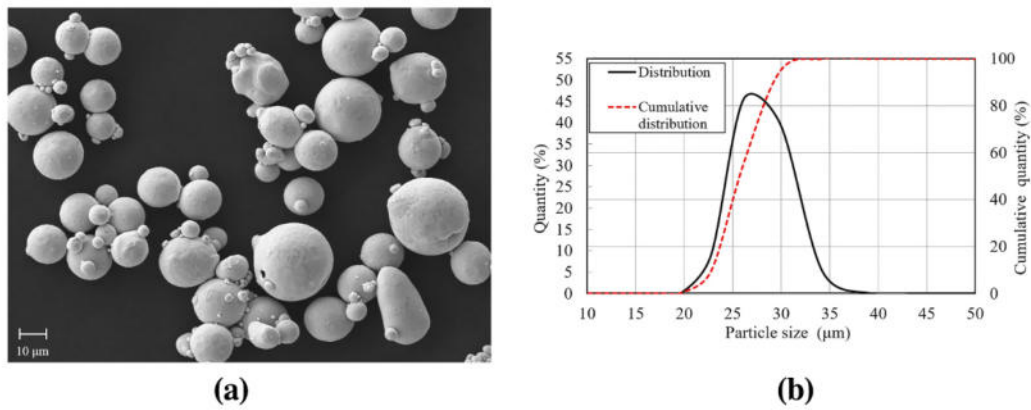


Fig. 1. Pure copper powder characterization: (a) SEM image; (b) particle size distribution.

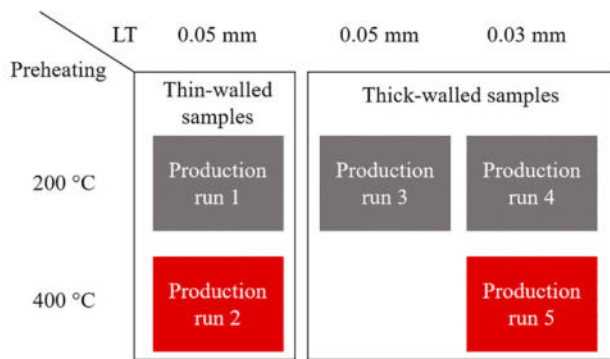


Fig. 2. The schema of production runs sorted by chronology, sample type, and process conditions.

2.2.1. Thin-walled samples

Single lined thin-walled specimens are samples for testing the ability to produce 3D object composed from single tracks stacked on each other. Laser path in each layer had a rectangular shape with a constant length of 10 mm and a width of 2 mm (Fig. 3b). The samples were placed on the sides of the build platform for avoiding laser back reflection (Fig. 3a). The effect of LP, LV and the preheating temperature was observed. The weld tracks interlayer connection and wall width were evaluated.

The energy density range of observed parameters, calculated as $LP \cdot (LV \cdot LT)^{-1}$, where LP is laser power (W); LV is laser velocity ($mm \cdot s^{-1}$) and LT is layer thickness (mm), started from 8.5 to 15 $J \cdot mm^{-2}$. The LP varied from 325 to 400 W, LV from 433 to 941 $mm \cdot s^{-1}$ and LT was set to a constant value of 0.05 mm. The two sets of samples were made with

the same laser parameters but different preheating temperatures 200 °C and 400 °C. In total, 112 thin-walled samples were produced.

The weld tracks connection was observed visually from cross-section images and the non-uniform wall width was evaluated by script created in a Matlab R2019b (The MathWorks Inc., Natick, USA). The script is capable to measure wall thickness on thousands of places across the sample height (green lines) and calculate the mean thickness and standard deviation (Fig. 4). The resulted data are the mean value of the two walls made with the same process parameters but once along and next against inert atmosphere flow.

2.2.2. Thick-walled samples

The thick-walled samples are volumetric parts intended for assessing the feasibility of producing copper parts made of walls by LPBF technology, for example for coolers. The rectangular thick-walled samples were produced with a length of 10 mm and variable sample width (SW) in the range of 0.5 to 1.7 mm (Fig. 5a). The effect of LT and preheating temperature as parameters influencing a whole production run was assessed on the produced samples. The effect of LT was tested with values of 0.05 and 0.03 mm and a preheating temperature with values of 200 °C and 400 °C. In particular production runs, the samples had variable LP, LV, HD, SW, laser scanning strategy and remelting strategy. The experiments aimed at finding the optimal parameters for producing thick-walled components with maximum RD.

2.2.2.1. Laser scanning strategies. Most of the samples were produced with a border scanning strategy (Fig. 5b₁). This strategy was introduced as more suitable for thin components [43]. The laser tracks in the border scanning strategy are composed of offset tracks following the sample edges. The scans are offset about HD.

Border scanning strategy with standard print order was also

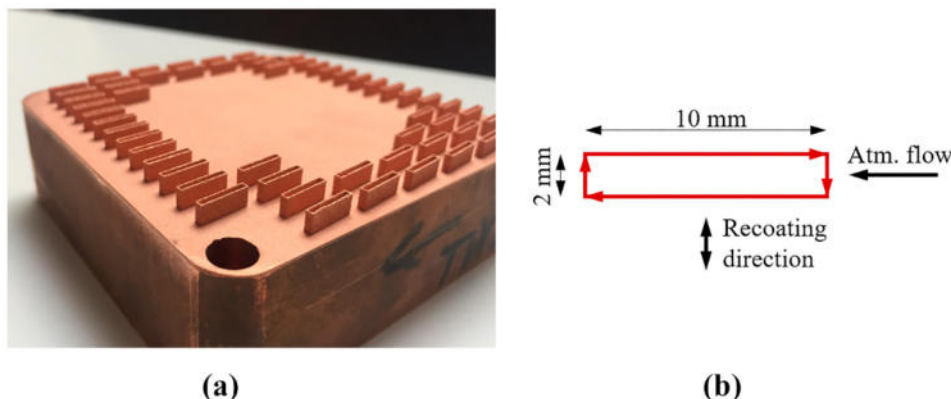


Fig. 3. Thin-walled samples made of pure copper: (a) Thin-walled samples on the copper platform; (b) Geometry and laser strategy of the thin-walls.

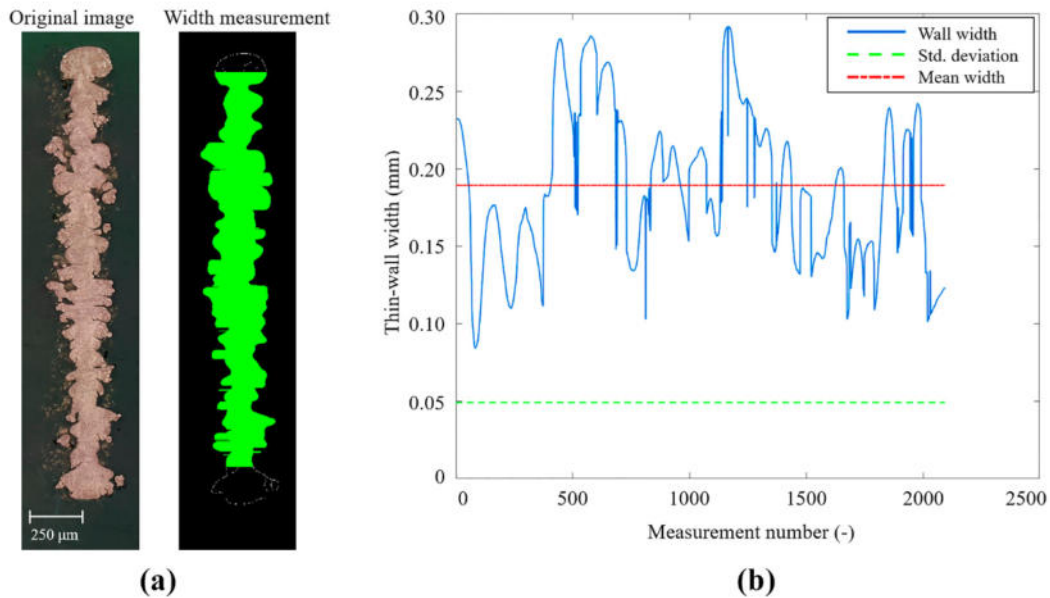


Fig. 4. Thin-wall width measurement by the Matlab script: (a) Original and processed image with the width measurement (green horizontal lines); (b) The results of thin-wall width measurement. (For interpretation of the references to colour in this figure legend, the reader is referred to the web version of this article.)

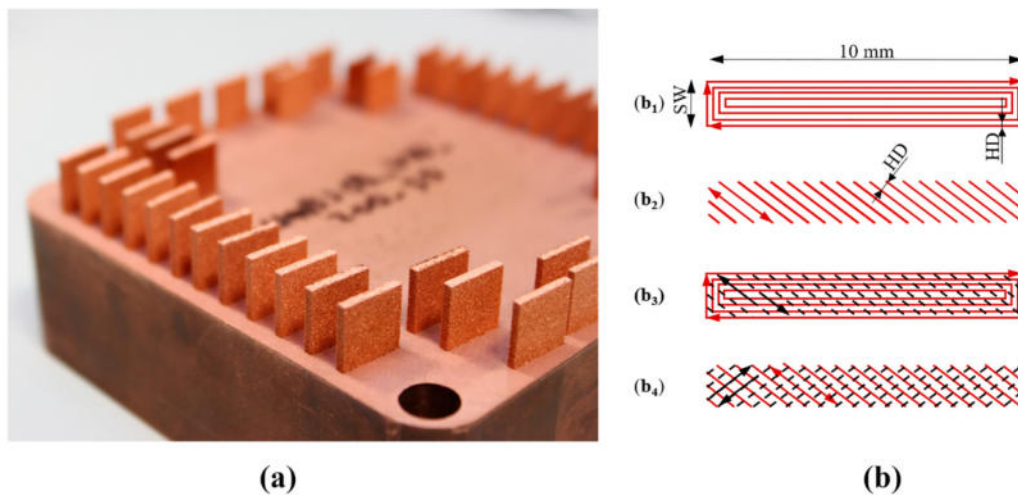


Fig. 5. Thick-walled samples: (a) Thick-walled samples on the copper platform; (b) Scanning strategies: (b₁) Border strategy; (b₂) Meander strategy; (b₃) Border strategy with meander remelting; (b₄) Meander strategy with meander remelting.

compared with a meander scanning strategy with 67° rotation in the following layer (Fig. 5b₂).

2.2.2.2. Remelting strategies. The remelting as another optional parameter was tested. Meander remelting strategy was applied with constant process parameters. The LP was set to 325 W, LV 400 mm·s⁻¹, HD 0.1 mm and a rotation of 67° in the following layer was used. This meander remelting strategy was applied on the selected border scanning strategy and meander scanning strategy samples (Fig. 5b_{3,4}).

2.2.2.3. Data acquisition and evaluation. The tremendous number of possible parameter combination was lowered by using statistical methods for experimental planning, e.g. Surface Response Design (SRD) and Fractional Factorial Design (FFD) method. Data were evaluated with 95% confidence level for all intervals and with backward elimination 0.05 of insignificant terms. For evaluation, was used Minitab (Minitab Inc., State College, USA).

The RD was evaluated from the polished (1 μm polishing suspension)

parallel to build cross-section by an optical method in the ImageJ v. 1.52 k (National Institutes of Health, USA). The RD was determined in the inner area of the sample cross-section image converted to 8-bit type and set an automatic threshold. The images for RD and microstructure evaluation were taken by Keyence – 3D Digital Microscope (VHX-6000, Mechelen, Belgium). The resulted RD is the mean value of two different cross-sections of one sample with a minimum distance of 1 mm. For the microstructure revelation, the etching solution of 2 g of K₂Cr₂O₇, 8 ml of H₂SO₄, 4 ml of saturated NaCl solution and 100 ml of distilled water was used.

SEM analysis and energy-dispersive X-ray spectroscopy (EDS) were made by SEM Zeiss Ultra-Plus 50 (Carl Zeiss AG, Oberkochen, Germany) equipped with EDX analyser Oxford (Oxford Instruments, High Wycombe, United Kingdom).

X-ray diffraction (XRD) was measured at Panalytical X'Pert (Malvern Panalytical Ltd., Malvern, United Kingdom). Diffractometer was set up in Bragg-Brentano geometry using Cu Kα radiation (λ = 1.54 Å) equipped by 1D-detector XCelerator. Cu lamp operated at current 30 mA and

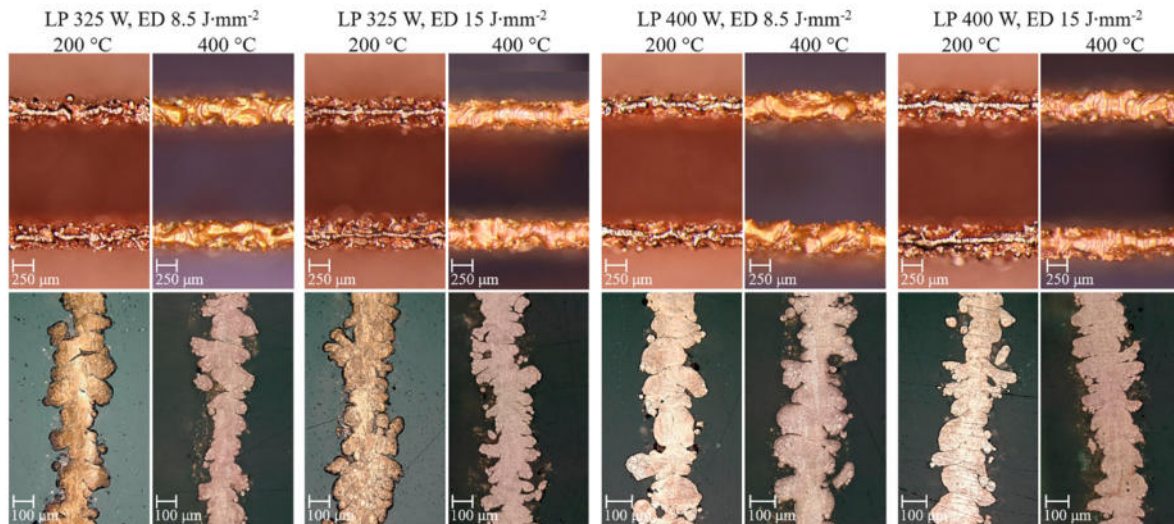


Fig. 6. The top-view and parallel to build cross-section images of selected thin-walled samples, comparison of the preheating temperature.

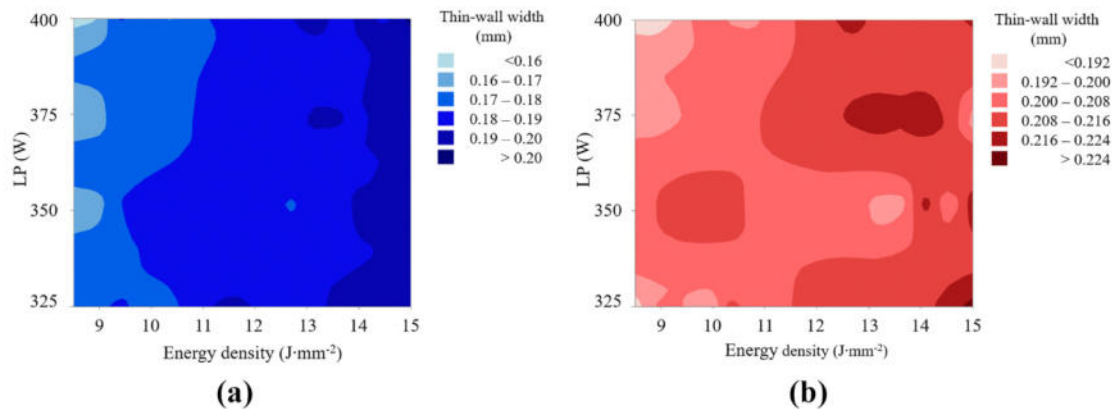


Fig. 7. Influence of the preheating temperature and the energy density on the width of thin-walled samples: (a) Countour plot for the preheating temperature of 200 °C; (b) Countour plot for the preheating temperature of 400 °C.

voltage 40 kV.

Phase analysis was performed based on chemical composition using databases PDF2 and ICSD. Qualitative phase analysis was calculated by Rietveld refinement from measured powder diffraction data with use of external Si standard.

3. Results

3.1. Thin-walled samples

The single lined thin-walled samples made with preheating of 200 °C and 400 °C in the energy density range from 8.5 to 15 J·mm⁻² showed that preheating temperature mainly increased wall-width (Figs. 6, 7). The build surface images (Fig. 6) showed non-consistent top-tracks in the whole energy range. The mean wall-width, measured by the Matlab script, increased from 0.183 mm to 0.207 mm. The difference between tracks made along or against the inner atmosphere flow was not detected. It is also shown (Fig. 7) that a higher energy density led to a higher thickness. Process parameters with the same energy density achieved almost the same wall thickness for the preheating temperature of 200 °C (Fig. 7a). The different laser power did not lead to a significant change in the wall-width. The standard deviation in thickness has almost a constant value for all the energies and preheating temperatures. Cross-section images showed issues with layer connection and non-uniform walls, which was also confirmed by the high mean standard deviation

of the wall-width of 0.044 mm, which corresponds to 23.8% and 21.2% of mean wall-width of samples produced with 200 °C and 400 °C preheating temperature. The complete list of the process parameters and thin-wall results can be found in the supplementary data (Table S1).

3.2. Thick-walled samples

3.2.1. Influence of layer thickness

The influence of LT was evaluated on the thirty-one samples tailored for SRD evaluation once printed with 0.05 mm, and then with 0.03 mm. Just by decreasing the LT, the energy density range increased from a range of 68–389 to 113 to 648 J·mm⁻³. The energy density was calculated as $LP \cdot (LV \cdot HD \cdot LT)^{-1}$. The LP and LV were studied in the range of 300–400 W respectively 200–1000 mm·s⁻¹, HD in the range of 0.03–0.15 mm, SW in the range of 0.5 to 1.7 mm and the border scanning strategy was used (Table 2).

The maximum value of RD using LT of 0.05 mm was 88.9% and 95.9% using 0.03 mm (Table 2). By decreasing the LT, the RD was improved in a mean value of about 7% (Fig. 8).

Analysis of variance (ANOVA) created within LT 0.03 mm samples identified LP and LV as significant parameters (Table 3). The HD and SW parameters were found as non-significant process parameters with unpredictable behaviour and terms were eliminated from the regression model by backward elimination. The origin of the high contribution of error, associated with unpredictable HD behaviour, is explained in the

Table 2
List of thin-walled samples process parameters and wall-width results.

Sample number ^a	LP (W)	LV (mm·s ⁻¹)	HD (mm)	SW (mm)	LT (mm)	Energy density [LT 0.03 mm] (J·mm ⁻³)	Relative density [LT 0.05 mm] (%)	Relative density [LT 0.03 mm] (%)
1, 32	325	400	0.06	0.8	0.05, 0.03	451	86.6	91.2
2, 33	375	400	0.06	0.8	0.05, 0.03	521	88.1	92.2
3, 34	325	800	0.06	0.8	0.05, 0.03	226	86.1	88.7
4, 35	375	800	0.06	0.8	0.05, 0.03	260	85.4	91.6
5, 36	325	400	0.12	0.8	0.05, 0.03	226	87.4	91.9
6, 37	375	400	0.12	0.8	0.05, 0.03	260	87.4	91.5
7, 38	325	800	0.12	0.8	0.05, 0.03	113	82.9	88.9
8, 39	375	800	0.12	0.8	0.05, 0.03	130	84.2	92.1
9, 40	325	400	0.06	1.4	0.05, 0.03	451	85.0	92.5
10, 41	375	400	0.06	1.4	0.05, 0.03	521	86.2	94.7
11, 42	325	800	0.06	1.4	0.05, 0.03	226	84.5	89.4
12, 43	375	800	0.06	1.4	0.05, 0.03	260	86.0	92.2
13, 44	325	400	0.12	1.4	0.05, 0.03	226	86.4	91.9
14, 45	375	400	0.12	1.4	0.05, 0.03	260	87.7	92.3
15, 46	325	800	0.12	1.4	0.05, 0.03	113	83.0	89.7
16, 47	375	800	0.12	1.4	0.05, 0.03	130	87.1	94.3
17, 48	300	600	0.09	1.1	0.05, 0.03	185	84.7	92.7
18, 49	400	600	0.09	1.1	0.05, 0.03	247	87.4	95.1
19, 50	350	200	0.09	1.1	0.05, 0.03	648	88.9	94.0
20, 51	350	1000	0.09	1.1	0.05, 0.03	130	83.8	92.2
21, 52	350	600	0.03	1.1	0.05, 0.03	648	83.9	94.8
22, 53	350	600	0.15	1.1	0.05, 0.03	130	85.5	94.0
23, 54	350	600	0.09	0.5	0.05, 0.03	216	86.4	93.6
24, 55	350	600	0.09	1.7	0.05, 0.03	216	86.9	95.9
25, 56	350	600	0.09	1.1	0.05, 0.03	216	85.4	94.3
26, 57	350	600	0.09	1.1	0.05, 0.03	216	85.8	94.7
27, 58	350	600	0.09	1.1	0.05, 0.03	216	85.2	94.7
28, 59	350	600	0.09	1.1	0.05, 0.03	216	84.9	94.6
29, 60	350	600	0.09	1.1	0.05, 0.03	216	84.5	94.6
30, 61	350	600	0.09	1.1	0.05, 0.03	216	84.4	93.5
31, 62	350	600	0.09	1.1	0.05, 0.03	216	86.3	95.2

^a Samples 1–31 produced using LT 0.05 mm, samples 32–62 produced using LT 0.03 mm.

following chapters. Fig. 9 shows a 3D representation of the influence of LP and LV on the RD. The SRD model predicted process parameters for reaching the highest RD in the observed range as LP 400 W, LV 505 mm·s⁻¹ and 0.03 mm LT.

3.2.2. Influence of preheating temperature

The influence of preheating temperature was assessed on the samples manufactured using the same process parameters once with 200 °C

(samples 32–47, Table 2) and next with 400 °C (samples 63–78, Table 4). The sample process parameters were also designed for FFD evaluation. The LP was set in the range of 325 to 375 W, LV from 400 to 800 mm·s⁻¹, HD from 0.06 to 0.12 mm and SW from 0.8 to 1.4 mm. The LT was set to 0.03 mm and the border scanning strategy was applied.

The higher preheating temperature improved RD in the mean value of about 4.4% from 91.6% to 96% (Fig. 10). The maximum measured RD of 99.4% was reached with preheating of 400 °C, LP 375 W, LV 400

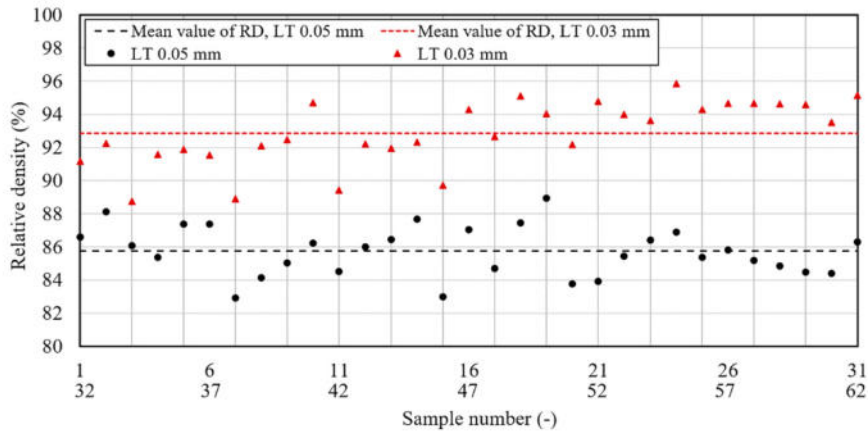


Fig. 8. The influence of LT on the RD of the thick-walled samples.

Table 3
SRD analysis of variance (ANOVA) for LT 0.03 mm.

Source	Contribution (%)	P-Value (-)
Model	36.7	0.006
LP	17.4	0.011
LV	8.4	0.070
LV•LV	10.9	0.040
Error	63.3	
Model Summary		
Standard deviation		Coefficient of determination
1.617		36.7%

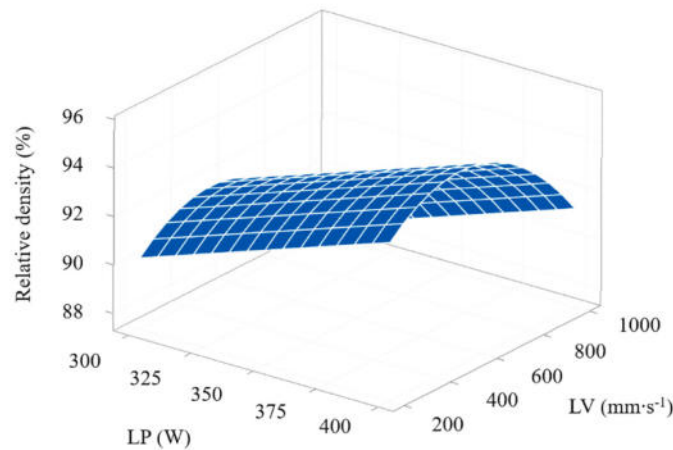


Fig. 9. 3D representation of the effect of LP and LV on RD of thick-walled samples.

mm•s⁻¹, HD 0.06 mm and SW 0.8 mm (sample 64). The RD was in case of preheating improved by a smoother build surface which resulted in more stable fusion conditions and as a consequence in lower voids between tracks (Fig. 11c,f). The surface smoothness is a necessary and intuitive condition for judging process parameters for reaching high RD [14,19]. Despite reached high RD with 400 °C preheating, the scan tracks were not fully connected indicating that low mechanical properties can be expected (Fig. 11b,e).

The FFD model was composed of samples 33, 34, 36, 39, 40, 43, 45, and 46 created with 200 °C (Table 2) and samples 63, 66, 68, 69, 72, 73, 75 and 78 made with 400 °C preheating. The ANOVA confirmed a highly positive impact of preheating on the RD (Table 5, Fig. 12). Further on, the HD parameter with a *p*-value of 0.019 is significant as well as in combination with preheating and SW parameter with a low *p*-value of

Table 4
Process parameters of samples used for evaluation of the base plate preheating.

Sample number	LP (W)	HD (mm)	SW (mm)	Energy density (J•mm ⁻³)	RD (%)
63	325	0.06	0.8	451	96.2
64	375	0.06	0.8	521	99.4
65	325	0.06	0.8	226	97.5
66	375	0.06	0.8	260	96.7
67	325	0.12	0.8	226	95.6
68	375	0.12	0.8	260	94.8
69	325	0.12	0.8	113	94.2
70	375	0.12	0.8	130	96.3
71	325	0.06	1.4	451	96.7
72	375	0.06	1.4	521	98.6
73	325	0.06	1.4	226	94.3
74	375	0.06	1.4	260	99.1
75	325	0.12	1.4	226	93.5
76	375	0.12	1.4	260	95.2
77	325	0.12	1.4	113	94.8
78	375	0.12	1.4	130	92.9

0.014 and 0.043 respectively.

The high temperature preheating caused powder and part surface oxidation (Fig. 13). Even though, the building process was maintained in the inert atmosphere of nitrogen with less than 0.2% O₂ concentration. The oxidation colour corresponds to the time for how long were the sample and powder exposed to the high temperatures (Fig. 13b) [44].

XRD and EDS analyses were performed on the virgin powder and samples 33 and 64 to compare the crystalline and phase changes and appearance of oxygen. The diffraction peaks at 2θ are attributed to the planes of the face-centered copper (Fig. 14). Peaks of other crystalline phases were detected neither in the virgin powder nor in the produced samples.

The EDS analysis performed on polished samples 33 and 64 did not show a significant change in the measured oxygen concentration inside the samples produced under different preheating temperatures (Fig. 15). The measured oxygen concentrations were 0.3 and 0.2 wt% in sample 33 and sample 64, respectively.

The oxidized unfused powder used within 400 °C preheating created agglomerates and the surfaces of the particles were covered by an oxide layer (Fig. 16a). The thickness of the oxide layer was from 1 to 3 μm (Fig. 16b). The EDS analysis confirmed the appearance of 10.46 ± 0.12 wt% of oxygen in area 1 and 14.15 ± 0.13 wt% in area 2 (Fig. 16a). For comparison, the oxygen content was evaluated on virgin powder, the average value (determined from ten measurements) was 0.46 ± 0.07 wt%. The increased amount of oxygen in the unfused powder is confirmed also by the increased intensity in the EDS point spectra graph (Fig. 17).

The EDS analysis cannot be interpreted as a quantitative analysis for

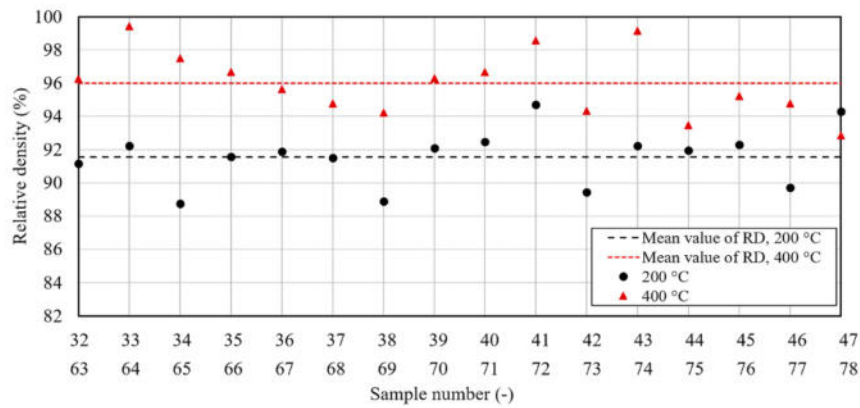


Fig. 10. The influence of base plate preheating temperature on the RD of the thick-walled samples.

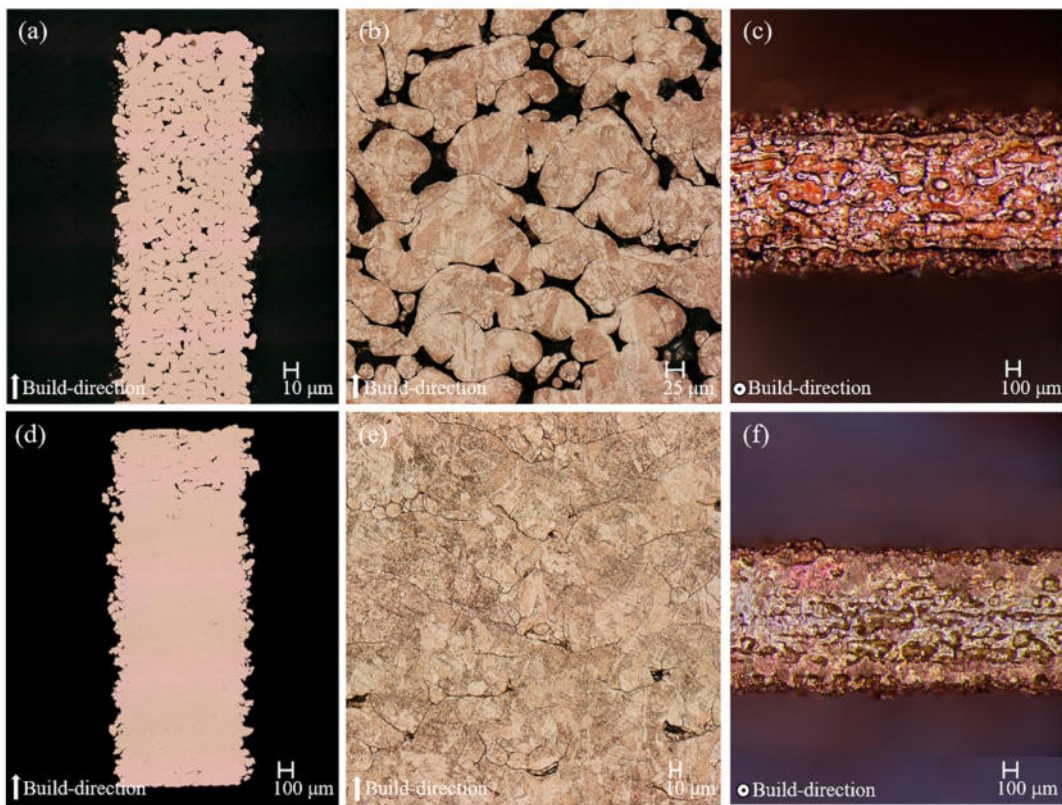


Fig. 11. The effect of base plate preheating temperature on RD of the thick-walled samples number 33 and 64; (a-c) Cross-section, microstructure and the build surface of the sample 33 produced using 200 °C, RD 92.2%; (d-f) Cross-section, microstructure and the build surface of the sample 64 produced using 400 °C, RD 99.4%.

oxygen concentration determination, due to its nature. Nevertheless, in combination with the performed XRD analysis, it can be assumed that high temperature preheating did not lead to an increased amount of oxygen inside the produced samples, although it caused oxidation of the unfused powder.

3.2.3. Influence of energy density

For ED range extension the extreme energy density samples were manufactured to check the influence of higher energy density input on the RD. The high energy density was reached by lowering LV since the maximum LP of used LPBF machine is limited to 400 W. The range of observed ED was from 243 to 2222 $\text{J}\cdot\text{mm}^{-3}$. The LP was set in the range of 350 to 400 W, the LV from 100 to 400 $\text{mm}\cdot\text{s}^{-1}$, HD 0.06 to 0.12 mm and SW from 0.8 to 1.4 mm. The LT was set to 0.03 mm and the samples

were once printed with preheating of 200 °C, and then with 400 °C (Table 6).

The maximum RD within extreme energy samples of 98.3% was reached using 400 °C preheating and the ED of 556 $\text{J}\cdot\text{mm}^{-3}$ (Table 6). The sample number 84 and 92 with maximum energy density 2222 $\text{J}\cdot\text{mm}^{-3}$ reached RD 95.8% using 200 °C and 94.8% using 400 °C.

Fig. 18 shows summarized data of all thick-walled samples created using LT of 0.03 mm sorted by ED and preheating temperatures. Using 200 °C preheating the maximum measured RD was in the range of 94% to 96%. Using 400 °C preheating the RD reached over 99% on samples using ED of around 250 and 500 $\text{J}\cdot\text{mm}^{-3}$. Overall, samples with ED higher than 600 $\text{J}\cdot\text{mm}^{-3}$ do not show clear uptrend relating to the RD improvement. The higher ED was maintained by lower LV and as Fig. 15 indicates that lower LV does not lead to higher RD.

Table 5
ANOVA table for evaluation of base plate preheating.

Source	Contribution (%)	P-Value
Model	93.6	0.000
LP	7.7	0.014
LV	8.2	0.012
HD	6.9	0.019
SW	0.1	0.771
Preheating	58.3	0.000
HD•SW	4.6	0.043
HD•Preheating	7.8	0.014
Error	6.0	
Model Summary		
Standard deviation	Coefficient of determination	
0.863	93.6%	

3.2.4. Scanning strategy

Most of the samples have been built with border scanning strategy. To confirm the suitability of this strategy for parts made of copper walls the meander scanning strategy was applied on one set of samples (Table 7). The samples were printed under 400 °C preheating temperature and with 0.03 mm LT. The results of RD showed slightly better performance of meander scanning strategy for processing volume walls of pure copper. The mean RD of samples using the same process parameters and border scanning strategy (samples number 63, 66, 68, 69, 72, 73, 75 and 78) was 95.1% and 96.2% using meander scanning strategy.

3.2.5. Remelting strategy

The meander remelting strategy was tested to increase RD. The effect of the meander remelting was assessed by comparison of eight samples created with variable LP, LV, HD and SW (Table 8) and samples created without remelting (sample numbers 32, 35, 37, 38, 41, 42, 44 and 47).

The meander remelting strategy proved a positive influence on RD which was increased by 2.8% from 91.5% to 94.3%.

3.2.6. Process parameters for the maximum relative density

All the above-presented results showed that for reaching the highest RD should be applied the 0.03 mm LT and 400 °C base plate preheating as global process conditions. Particular process parameters predicted from SRD model should be set as LP 400 W, LV 505 mm•s⁻¹. The HD parameter did not show a clear impact on RD within 200 °C preheating. This situation was changed using 400 °C where HD parameter in combination with preheating proved a significant impact and the optimum predicted value was 0.06 mm. Further on, using the meander scanning strategy with meander remelting can lead to superior RD. For confirmation of those conclusions, additional samples (Table 9) were created.

The sample 119 with Border scanning strategy reached RD of 99.7%, but Meander remelting did not lead to higher RD. Meander scanning strategy led to RD of 99.8% and by the Meander remelting the RD was improved to 99.9% (Fig. 19e). Despite RD of 99.9%, the issues with layer bonding marked by red rectangles persisted (Fig. 19e,f).

4. Discussion

4.1. Influence of layer thickness

The results introduced in the previous chapters showed the process parameters leading to producing a 3D object of pure copper with RD higher than 99% by using 400 W fibre laser. The LT was indicated as the most influencing parameter. In the mean value, calculated from the samples made with variable LP, LV, HD and SW, the RD increased of about 7% just by decreasing LT from 0.05 to 0.03 mm. The results indicating that further decreasing of the LT could lead to even higher RD.

4.2. Process parameters variations

From the observed range of process parameters, the LP 400 W and LV 505 mm•s⁻¹ were identified by SRD as the most suitable laser-related

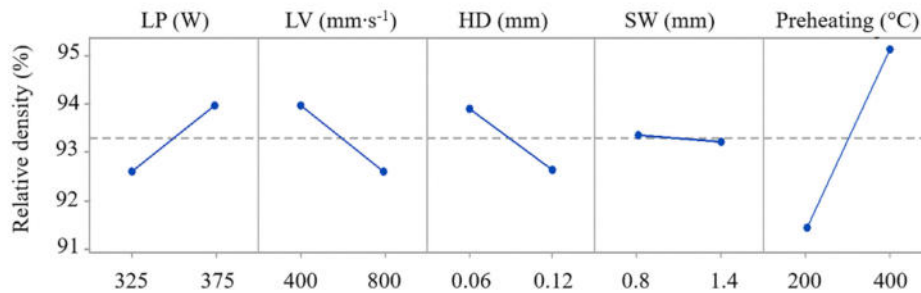


Fig. 12. The effect of process parameters and preheating on RD of the thick-walled samples.

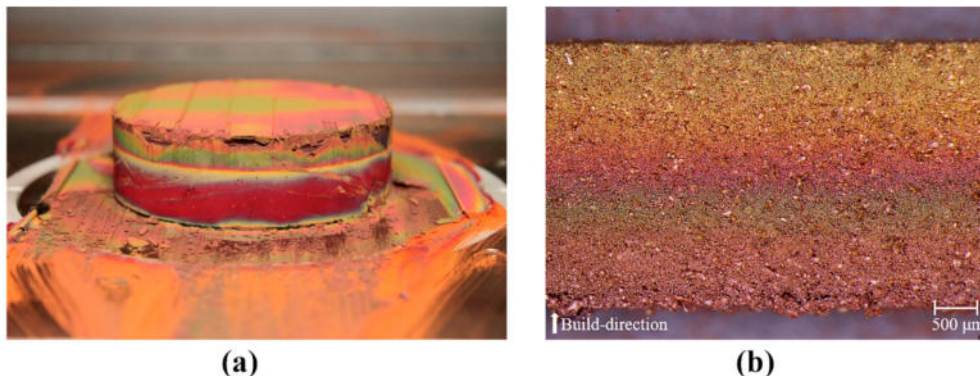


Fig. 13. Thick-walled samples, powder and sample surface oxidation caused by high temperature preheating: (a) Oxidized and agglomerated powder in the building chamber; (b) Side view on the oxidized sample surface.

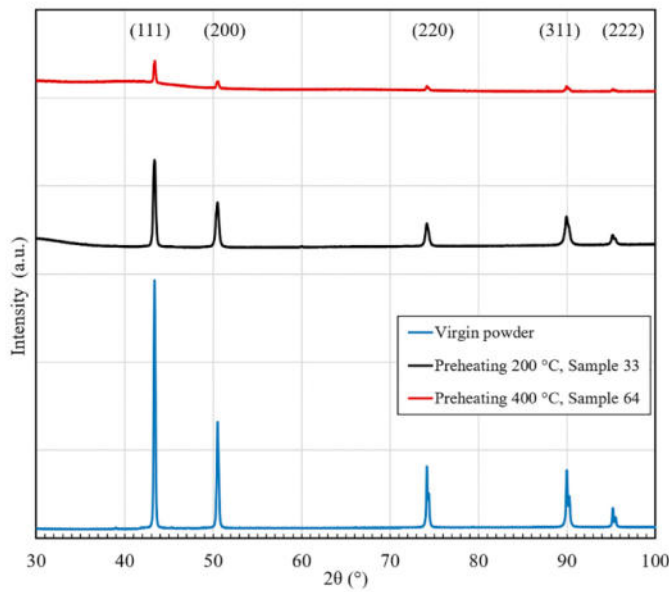


Fig. 14. X-ray diffraction spectra for the virgin powder and fused samples under preheating 200 °C (Sample 33) and 400 °C (Sample 64).

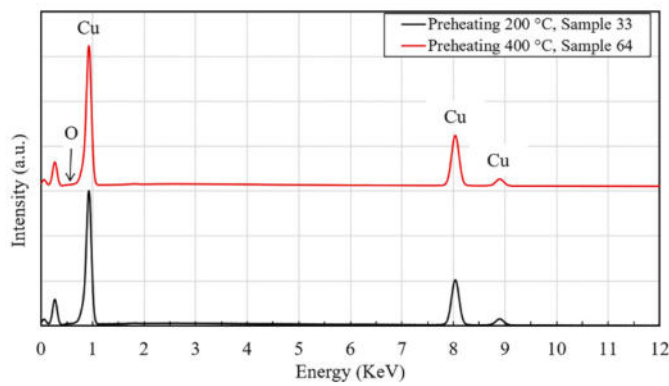


Fig. 15. EDS point spectra intensity graph of sample 33 and sample 64.

setting for preheating 200 °C and LT 0.03 mm. The SRD model despite high error caused by unpredictable HD parameter behaviour identified similar laser-related process parameters as Constantin [19], who without any preheating have found a narrow range of process parameters leading to RD up to 95%.

The LP was tested in the range of 300 to 400 W, where all results indicated that higher LP would lead to superior RD. The LV was tested in the range of 100 to 1000 mm·s⁻¹ and even lower LV did not lead to lower porosity (Fig. 18). Thus, it could be deduced that LP cannot be equivalently replaced by lowering LV even though the energy density (calculated as $LP \cdot (LV \cdot HD \cdot LT)^{-1}$) could reach the same value. This conclusion corresponds with previous research using Al–12Si material [45] and copper [19]. Authors [14,19] studied fusion of copper powder by laser beam attribute decreased RD by using low LV to increased surface roughness of previously solidified layer. The increased surface roughness is caused by different velocity of laser beam and melt pool flow resulting in bumps at the pool borders. As opposite, high LV causes insufficient powder fusion and slow molten pool flow leading to fluctuations resulting in balling and large pores formation. Those

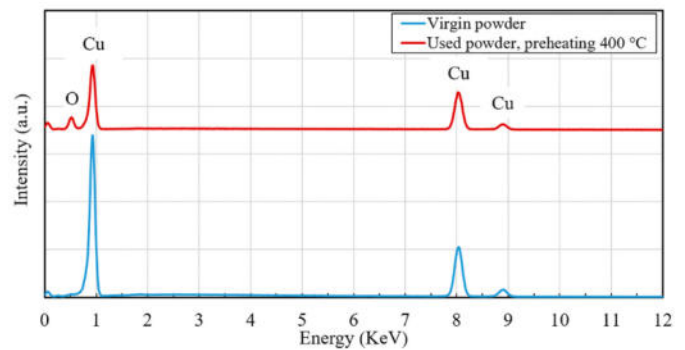


Fig. 17. EDS point spectra intensity graph of the virgin copper powder and the unfused powder used under 400 °C preheating temperature.

Table 6

Process parameters of extreme energy samples.

Sample number ^a	LP (W)	HD (mm)	SW (mm)	Energy density (J·mm ⁻³)	RD [200 °C preheating] (%)	RD [400 °C preheating] (%)
79, 87	350	0.06	0.8	1944	94.5	–
80, 88	350	0.12	0.8	243	94.0	95.6
81, 89	400	0.12	0.8	1111	93.8	96.7
82, 90	400	0.06	0.8	556	95.0	98.3
83, 91	400	0.12	1.4	278	94.4	95.0
84, 92	400	0.06	1.4	2222	95.8	94.8
85, 93	350	0.12	1.4	972	93.8	95.3
86, 94	350	0.06	1.4	486	95.6	97.5

^a Samples 79–86 produced using 200 °C preheating, samples 87–94 produced using 400 °C preheating.

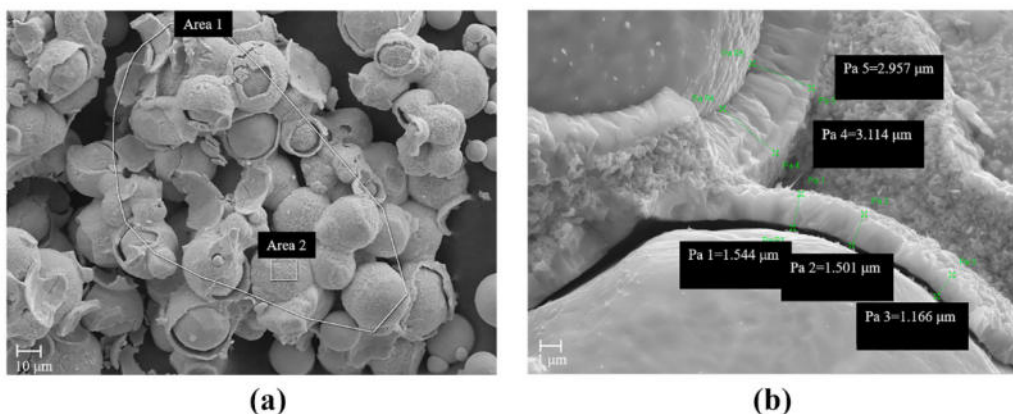


Fig. 16. Powder oxidation caused by 400 °C preheating: (a) Oxidized and agglomerated powder with marked areas for EDS analysis; (b) Magnified image of oxide layers and oxide thickness measurement.

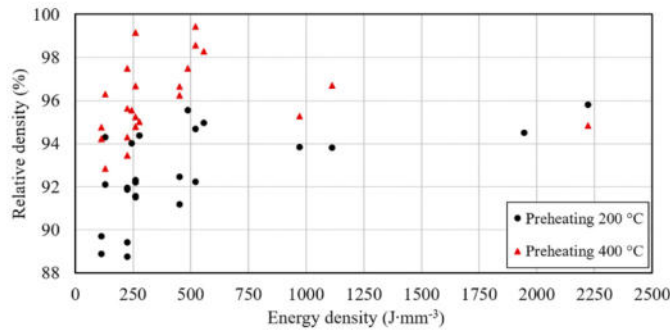


Fig. 18. The effect of energy density and base plate preheating on the RD of the thick-walled samples.

Table 7
Process parameters of samples using meander scanning strategy.

Sample number	LP (W)	LV (mm·s ⁻¹)	HD (mm)	SW (mm)	Scanning strategy	RD (%)
95	325	400	0.06	0.8	Meander	94.7
96	375	800	0.06	0.8	Meander	95.8
97	375	400	0.12	0.8	Meander	96.9
98	325	800	0.12	0.8	Meander	96.1
99	375	400	0.06	1.4	Meander	98.1
100	325	800	0.06	1.4	Meander	94.6
101	325	400	0.12	1.4	Meander	95.8
102	375	800	0.12	1.4	Meander	97.8

Table 8
Process parameters of remelting samples.

Sample number	LP (W)	LV (mm·s ⁻¹)	HD (mm)	SW (mm)	Remelting strategy	RD (%)
103	325	400	0.06	0.8	Meander remelting	92.4
104	375	800	0.06	0.8	Meander remelting	93.8
105	375	400	0.12	0.8	Meander remelting	94.5
106	325	800	0.12	0.8	Meander remelting	92.3
107	375	400	0.06	1.4	Meander remelting	96.2
108	325	800	0.06	1.4	Meander remelting	93.6
109	325	400	0.12	1.4	Meander remelting	95.3
110	375	800	0.12	1.4	Meander remelting	96.3

conclusions fit to the observed behaviour of copper in this study. Using relatively low or extreme high energy density lead to melt pool fluctuations and as a consequence a rough build surface which resulted in low RD (Fig. 20). The highest RD was reached on samples with relatively smooth build surfaces (Figs. 11, 19).

The SW of the thick-walled samples observed in the range of 0.5 to 1.7 mm did not show a significant impact on the RD neither using 200 °C nor 400 °C preheating temperature. Thus, it can be considered that in

Table 9
Process parameters of samples for maximum RD.

Sample number	LT (mm)	Preheating (°C)	LP (W)	LV (mm·s ⁻¹)	HD (mm)	SW (mm)	Scanning strategy	Remelting strategy	RD (%)
119	0.03	400	400	505	0.06	1.7	Border	–	99.7
120	0.03	400	400	505	0.06	1.7	Border	Meander remelting	99.7
121	0.03	400	400	505	0.06	1.7	Meander	–	99.8
122	0.03	400	400	505	0.06	1.7	Meander	Meander remelting	99.9

the observed range the SW does not influence the RD.

4.3. Influence of preheating temperature

Thin-walled samples within 200 °C preheating indicated non-homogeneous tracks, layer bonding issues and the balling effect was detected in the whole range of tested process parameters. By applying the 400 °C base plate preheating temperature the thin-walled samples were wider in the mean value of about 24 µm and layer bonding was improved. This effect could have also affected the behaviour of the HD parameter within thick-walled samples processed under high temperature preheating of 400 °C where optimum HD was identified by FFD evaluation as 0.06 mm.

The higher preheating temperature of 400 °C increased track width and led to a smoother surface which resulted in lower porosity within thick-walled samples. The RD was in mean value increased by 4.4% in comparison with 200 °C preheating temperature.

The positive preheating effect to the weld track could be explained by three main factors which higher temperature causes. The first one is decreasing the energy necessary to melt the powder. The second one is increasing of copper laser absorptivity and the third one is changing wetting conditions and prolonging the solidification time of melted material.

The energy necessary for melting the material could be calculated by eq. $Q = \rho C_p(T_f - T_i) + \rho L_f$ [34]. By using bulk density ρ 8960 kg·m⁻³, specific heat C_p 383 J·kg⁻¹·K⁻¹, latent heat of fusion L_f 204,000 J·kg⁻¹ and fusion temperature T_f 1356 K could be calculated that by increasing preheating temperature from 200 °C to 400 °C the energy necessary for melting the powder is lowered by 12.5%.

The second effect of preheating is in increasing laser absorptivity. For the used laser in this study, the theoretical laser absorptivity of copper could be increased by about 5% [37] by increasing the preheating temperature from 200 °C to 400 °C.

The preheating temperature is beneficial for improving wetting conditions in the LPBF process. The LPBF can be compared to a homologous wetting of liquid droplet on the bulk material of the same kind. In the case of LPBF, the spreading of liquid is driven by the capillarity and resisted by the inertia forces [13,46]. In the non-isothermal case, the spreading of a droplet is arrested by freezing when advancing contact angle reach angle of solidifying front. The liquid is arrested at apparent contact angle θ^* which in homologous wetting depend only on Stefan number $S = c_{pl}(T_f - T_i)/L_f$, $\theta^* \approx f(S)$ [47], where c_{pl} is the specific heat of the liquid, T_f is the temperature of fusion, T_i is target temperature and L_f is the latent heat of fusion. The spreading of droplet radius R on a bulk solid surface is controlled by eq. $R/a = 2.4 (1 - \exp(0.9 t(\rho_m a^3 \sigma^{-1})^{-1/2}))$ [46], where a is droplet radius (in case of LPBF $a \approx 100$ µm [13]), ρ_m is liquid density, σ is liquid surface tension. In the non-isothermal case, the radius is arrested at R^* which for given material depends only on S , $R^* \approx f(S)$ [47]. The high values of S (low target temperature T_i) lead to low droplet base radius R^* and high apparent contact angle θ^* resulting in wetting issues. Thus, the higher target temperature (preheating temperature) is beneficial for melt pool spreading. Further on, the preheating temperature increased the droplet solidification and cooling timescale [48], which in combination with better wetting conditions resulted in wider thin-walled samples and smoother build surface of thick-walled samples when suitable laser-related process parameters were applied.

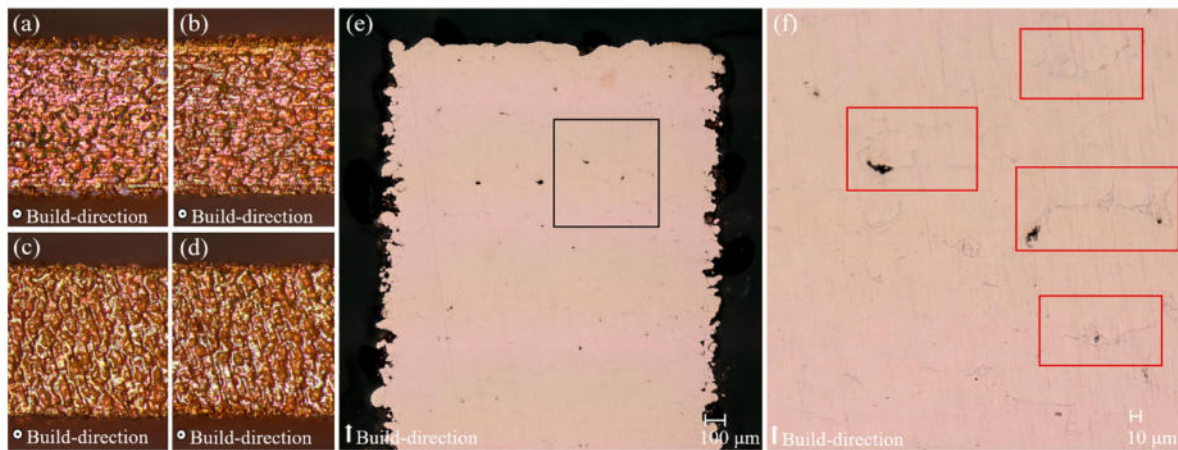


Fig. 19. Samples for maximum RD: (a-d) Images of the top surfaces of the 119–122 samples; (e) Cross-section of sample 122 processed using LP 400 W, LV 505 $\text{mm}\cdot\text{s}^{-1}$, HD 0.06, SW 1.7 mm, LT 0.03 mm, 400 °C preheating temperature, meander scanning strategy and meander remelting strategy (LP 325 W, LV 400 $\text{mm}\cdot\text{s}^{-1}$ and HD 0.1 mm); (f) The magnified area marked in image e. The red rectangles show unconnected areas. (For interpretation of the references to colour in this figure legend, the reader is referred to the web version of this article.)

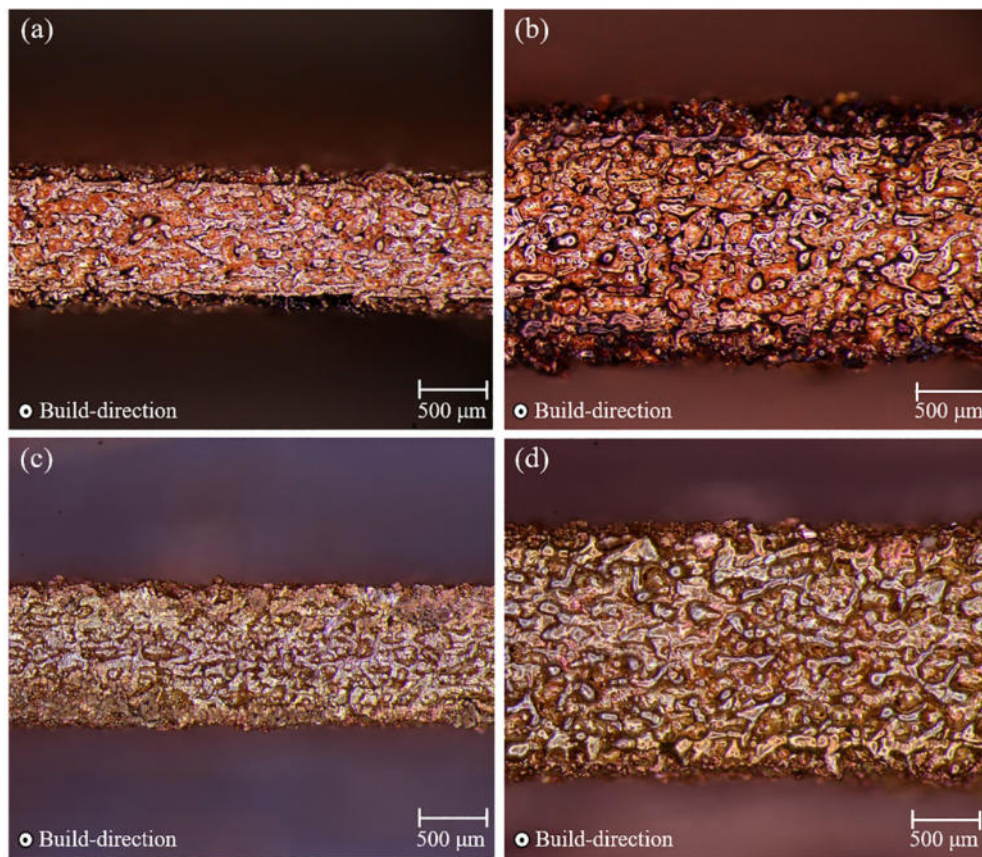


Fig. 20. Influence of ED on the sample build surface texture; (a) Sample 34 preheating 200 °C, ED 226 $\text{J}\cdot\text{mm}^{-3}$, RD 86.1%; (b) Sample 84 preheating 200 °C, ED 2222 $\text{J}\cdot\text{mm}^{-3}$, RD 95.8%; (c) Sample 65 preheating 400 °C, ED 226 $\text{J}\cdot\text{mm}^{-3}$, RD 97.1% (d) Sample 92 preheating 400 °C, ED 2222 $\text{J}\cdot\text{mm}^{-3}$, RD 94.8%.

Further on, the preheating temperature reduced the copper thermal conductivity and decreased temperature gradient. Thermal conductivity of copper drops about 4.3% when preheating is increased from 200 to 400 °C [49]. Thus, the cooling rate of highly conductive copper was slowed and the temperature differences in the molten pool reduced. The low temperature gradient in the molten pool reduces the effect of heat expansion and contraction, which directly affect the formation of cracks in copper parts processed by LPBF [14]. The cracks were not observed in

this study where all parts were produced using at least preheating of 200 °C. On the contrary, the formation of cracks was reported when pure copper was processed without any preheating [19].

4.4. Oxidation of copper during LPBF

Despite the reached RD higher than 99%, the layers and tracks were not sufficiently connected which could indicate low mechanical and

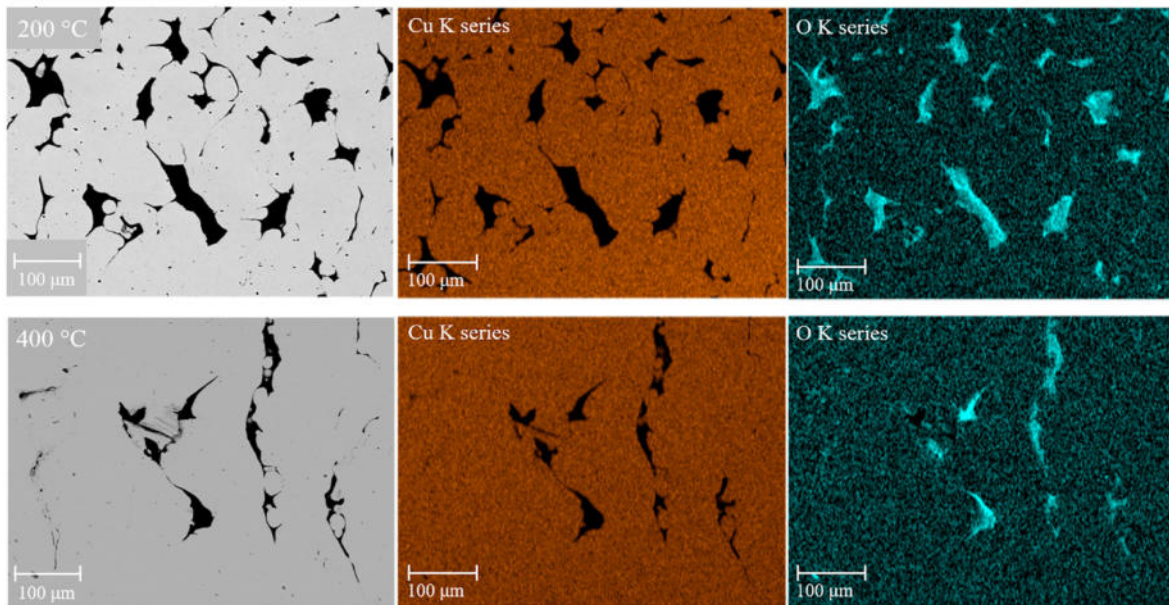


Fig. 21. EDS oxygen and copper element mapping of sample 33 and 64 produced using LP 375 W, LV 400 mm·s⁻¹, HD 0.06 mm and border scanning strategy: Comparison of the sample produced using 200 °C (top images) and 400 °C (bottom images) preheating temperature.

thermal conductivity properties [31]. The process was maintained under the inert nitrogen atmosphere with a maximum oxygen concentration of 0.2%, which did not prevent the oxidation of unfused powder preheated to high temperatures. Copper has a high affinity to oxygen and tendency to create surface oxides which affect wetting conditions and acts as a physical barrier for wetting and reduce flowability [7]. The measured oxygen concentration in the unfused powder by EDS was over 10 wt%. On the contrary, the virgin powder contained 0.46 wt% of oxide while the measured concentrations in the produced parts were 0.3 and 0.2 wt % using preheating 200 °C and 400 °C, respectively. The EDS cannot exactly quantify the oxygen concentration (obtained values in wt% are indicative only) but with respect to gained EDS spectra (Figs. 15, 17) and XRD data (Fig. 14) it can be assumed that no other phases except pure copper were present in the processed material. It indicates that high temperature preheating does not lead to an increased amount of oxygen in the produced samples. Further on, the laser fusion process leads to a decreasing amount of oxygen originated in the virgin powder which corresponds to Constantin [19]. The new powder layer is after spreading immediately fused by laser onto a build surface which decreases the surface of a material and can hinder oxidation of the solid part volume. On the contrary, the unfused powder with a high surface area and the surfaces of the solid samples (Fig. 13b) are exposed to elevated temperatures for the whole build-time which led to oxidation and high differences in oxygen concentration between the fused solid material and unfused powder.

The copper oxides have a higher melting point CuO ($T_m = 1336$ °C), Cu₂O ($T_m = 1230$ °C) than pure copper ($T_m = 1083$ °C) and are less stable at elevated temperatures [7]. Thus, the high temperature preheating has a positive effect on dissolving oxides in the bulk material because it is increasing the temperature of the bulk part and prolonging the time when oxides can disassociate. The similar effect has remelting which can also prolong the time necessary for oxide dissolving [7]. The meander remelting in this study confirmed the positive influence on RD which was increased by 2.8%, despite just one strategy with one process parameter set was tested. The more suitable remelting strategy could lead to even higher RD. The increased RD by preheating and remelting was mainly attributed to the smoother build surface (Fig. 19), however, reduced oxides lead to superior wetting conditions which contribute to further RD improvement. Nevertheless, the issues with layer bonding persisted.

The location of oxygen was checked by EDS element mapping which confirms the theory about their presence in the voids between unconnected tracks and layers. The EDS mapping was conducted on samples created with preheating of 200 °C and 400 °C with constant other process parameters (Fig. 21).

5. Conclusions

In the presented study, the effect of layer thickness, laser power, laser velocity, hatch distance, sample width, powder bed preheating temperature, scanning and remelting strategies on the relative density of copper thin-walled samples processed by LPBF technology was studied. The main conclusions are the following:

- The relative density of copper thin-walled specimens over 99% can be achieved using 400 W fibre laser with a wavelength of 1064 nm.
- Process parameters leading to relative density over 99% are: layer thickness 0.03 mm, laser power 400 W, laser velocity 505 mm·s⁻¹, hatch distance 0.06 mm, powder bed preheating 400 °C.
- The layer thickness was detected as the main influencing parameter for the relative density. By lowering its value may be reached even higher relative density.
- The laser power was detected as a highly significant parameter and from the observed range 300–400 W it was indicated that even higher laser power should lead to lower porosity.
- The laser velocity was tested in the range of 100–1000 mm·s⁻¹ and the optimum set was found as 505 mm·s⁻¹. It was observed that by lowering the laser velocity cannot be equivalently replaced energy delivered from laser power even though the energy density has the same value.
- The most suitable hatch distance of 0.06 mm was detected in combination with 400 °C powder bed preheating. The powder bed preheating to lower temperature of 200 °C caused an unpredictable relation between hatch distance parameter and relative density.
- The powder bed preheating tested in the two levels 400 °C and 200 °C revealed a highly positive influence on the relative density. The relative density over 99% was achieved only when 400 °C powder bed preheating was applied. On the other hand, the preheating to high temperatures caused unfused powder oxidation and

agglomeration which restricts powder reusability, but increased oxidation in fused solid material was not detected.

- Despite high relative density over 99%, the issues with layer bonding were detected. Issues with weld connection could be attributed to thin oxide layers which hinder wettability. Thus, the oxygen concentration within the process and virgin material should be strictly controlled.
- The meander scanning strategy showed better performance for relative density than the border scanning strategy in case of copper thin-walled parts.
- The meander remelting strategy led to a higher relative density.

Funding

This work was supported by ESA Express Procurement Plus – EXPRO+ within the research project Additive Design for Aerospace Applications Capabilities (ADAAC), [AO/1-9018/17/NL/GLC/hh], ESIF, EU Operational Programme Research, Development and Education within the research project (Architected materials designed for additive manufacturing) [Grant no. CZ.02.1.01/0.0/0.0/16_025/0007304] and faculty specific research projects [No. FSI-S-20-6296 and FSI-S-20-6290].

CRediT authorship contribution statement

Martin Malý: Conceptualization, Methodology, Formal analysis, Investigation, Data curation, Writing – original draft, Writing – review & editing, Visualization. **Daniel Koutný:** Conceptualization, Methodology, Validation, Resources, Writing – review & editing, Supervision, Project administration, Funding acquisition. **Libor Pantělejev:** Validation, Investigation, Resources, Writing – review & editing, Funding acquisition. **Laurent Pambaguian:** Validation, Resources, Writing – review & editing, Project administration, Funding acquisition. **David Paloušek:** Validation, Resources, Writing – review & editing, Supervision, Project administration, Funding acquisition.

Declaration of competing interest

The authors declare that they have no known competing financial interests or personal relationships that could have appeared to influence the work reported in this paper.

Appendix A. Supplementary data

Supplementary data to this article can be found online at <https://doi.org/10.1016/j.jmapro.2021.11.035>.

References

- [1] Kruth JP, Froyen L, Van Vaerenbergh J, Mercelis P, Rombouts M, Lauwers B. Selective laser melting of iron-based powder. *J Mater Process Technol* 2004;149: 616–22. <https://doi.org/10.1016/j.jmatprotec.2003.11.051>.
- [2] Schleifenbaum H, Meiners W, Wissenbach K, Hinke C. Individualized production by means of high power selective laser melting. *CIRP J Manuf Sci Technol* 2010;2: 161–9. <https://doi.org/10.1016/j.cirpj.2010.03.005>.
- [3] Gu DD, Meiners W, K. Wissenbach R.P.. Laser additive manufacturing of metallic components: materials, processes, and mechanisms. *Laser Addit Manuf Mater Des Technol Appl* 2012;6608:163–80. <https://doi.org/10.1179/1743280411Y.0000000014>.
- [4] Tran TQ, Chinnappan A, Lee JKY, Loc NH, Tran LT, Wang G, et al. 3D printing of highly pure copper. *Metals (Basel)* 2019;9:12–20. <https://doi.org/10.3390/met9070756>.
- [5] Frigola P, Harrysson O, Horn T, West H, Aman R, Rigsbee J, et al. Fabricating copper components with electron beam melting. *Adv Mater Process* 2014;172: 20–4.
- [6] El-Wardany TI, She Y, Jagdale VN, Garofano JK, Liou JJ, Schmidt WR. Challenges in three-dimensional printing of high-conductivity copper. *J Electron Packag Trans ASME* 2018;140:1–12. <https://doi.org/10.1115/1.4039974>.
- [7] Pogson SR, Fox P, Sutcliffe CJ, O'Neill W. The production of copper parts using DMLR. *Rapid Prototyp J* 2003;9:334–43. <https://doi.org/10.1108/13552540310502239>.
- [8] Lodes MA, Guschlbauer R, Körner C. Process development for the manufacturing of 99.94% pure copper via selective electron beam melting. *Mater Lett* 2015;143: 298–301. <https://doi.org/10.1016/j.matlet.2014.12.105>.
- [9] Bergström D. The absorption of laser light by rough metal surfaces. 2008.
- [10] Jadhav SD, Dadbakhsh S, Vleugels J, Hofkens J, Van Puyvelde P, Yang S, et al. Influence of carbon nanoparticle addition (and impurities) on selective laser melting of pure copper. *Materials (Basel)* 2019;12. <https://doi.org/10.3390/ma12152469>.
- [11] Wang H, Kawahito Y, Yoshida R, Nakashima Y, Shiokawa K. A model to calculate the laser absorption property of actual surface. *Int J Heat Mass Transf* 2018;118: 562–9. <https://doi.org/10.1016/j.ijheatmasstransfer.2017.11.023>.
- [12] Zhang J, Gu D, Yang Y, Zhang H, Chen H, Dai D, et al. Influence of particle size on laser absorption and scanning track formation mechanisms of pure tungsten powder during selective laser melting. *Engineering* 2019;5:736–45. <https://doi.org/10.1016/j.eng.2019.07.003>.
- [13] Zhou X, Liu X, Zhang D, Shen Z, Liu W. Balling phenomena in selective laser melted tungsten. *J Mater Process Technol* 2015;222:33–42. <https://doi.org/10.1016/j.jmatprotec.2015.02.032>.
- [14] Lingqin X, Guang C, Luyu Z, Pan L. Explore the feasibility of fabricating pure copper parts with low-laser energy by selective laser melting. *Mater Res Express* 2020;7. <https://doi.org/10.1088/2053-1591/abbd08>.
- [15] Lykov PA, Safonov EV, Akhmedjanov AM. Selective laser melting of copper. *Mater Sci Forum* 2016;843:284–8. <https://doi.org/10.4028/www.scientific.net/MSF.843.284>.
- [16] Kaden L, Matthäus G, Ullsperger T, Engelhardt H, Rettenmayr M, Tünnermann A, et al. Selective laser melting of copper using ultrashort laser pulses. *Appl Phys A* 2017;123:596. <https://doi.org/10.1007/s00339-017-1189-6>.
- [17] Trevistano F, Calignano F, Lorusso M, Lombardi M, Manfredi D, Fino P. Selective laser melting of chemical pure copper powders. In: *Euro PM 2017*; 2017.
- [18] Guan J, Zhang X, Jiang Y, Yan Y. Insights into fabrication mechanism of pure copper thin wall components by selective infrared laser melting. *Rapid Prototyp J* 2019;25:1388–97. <https://doi.org/10.1108/RPJ-06-2018-0143>.
- [19] Constantin L, Wu Z, Li N, Fan L, Silvain JF, Lu YF. Laser 3D printing of complex copper structures. *Addit Manuf* 2020;35:101268. <https://doi.org/10.1016/j.addma.2020.101268>.
- [20] EOS. EOS Copper Cu for EOS M 290 EOS Copper Cu. 2019. <https://www.eos.in fo/en/additive-manufacturing/3d-printing-metal/dmls-metal-materials/copper>.
- [21] Elementum. Copper (AMCopper-100). 2020. <https://www.elementum3d.com/copper-data-sheet>.
- [22] Ikeshoji T-T, Nakamura K, Yonehara M, Imai K, Kyogoku H. Selective laser melting of pure copper. *JOM* 2018;70:396–400. <https://doi.org/10.1007/s11837-017-2695-x>.
- [23] Colopi M, Caprio L, Demir AG, Previtali B. Selective laser melting of pure Cu with a 1 kW single mode fiber laser. *Procedia CIRP* 2018;74:59–63. <https://doi.org/10.1016/j.procir.2018.08.030>.
- [24] Jadhav SD, Dadbakhsh S, Goossens L, Kruth J-P, Van Humbeeck J, Vanmeensel K. Influence of selective laser melting process parameters on texture evolution in pure copper. *J Mater Process Technol* 2019;270:47–58. <https://doi.org/10.1016/j.jmatprotec.2019.02.022>.
- [25] Heussen D. Press release: green light for new 3D printing process. Fraunhofer ILT; 2017. <https://www.ilt.fraunhofer.de/en/press/press-releases/press-release-2017/press-release-2017-08-30.html>. [Accessed 20 July 2020].
- [26] Engler S, Ramsayer R, Poprawe R. Process studies on laser welding of copper with brilliant green and infrared lasers. *Phys Procedia* 2011;12:339–46. <https://doi.org/10.1016/j.phpro.2011.03.142>.
- [27] Haubold M, Ganser A, Eder T, Zäh MF. Laser welding of copper using a high power disc laser at green wavelength. *Procedia CIRP* 2018;74:446–9. <https://doi.org/10.1016/j.procir.2018.08.161>.
- [28] Pelaprat J-M, Finuf M, Fritz R, Zediker M. Seeing things in a new light high power blue lasers for metal processing Jean-Michel. *Laser Tech J* 2018;15:39–41. <https://doi.org/10.1002/latj.201800028>.
- [29] Hori E, Sato Y, Shibata T, Tojo K, Tsukamoto M. Development of SLM process using 200 W blue diode laser for pure copper additive manufacturing of high density structure. *J Laser Appl* 2021;33:012008. <https://doi.org/10.2351/7.0000311>.
- [30] Paloušek D, Kocica M, Pantelejev L, Klakurkova L, Celko L, Koutný D, et al. SLM process parameters development of Cu-alloy Cu7.2Ni1.8Si1Cr. *Rapid Prototyp J* 2019;25:266–76. <https://doi.org/10.1108/RPJ-06-2017-0116>.
- [31] Ott J, Burghardt A, Britz D, Mücklich F. Influence of porosity and impurities on the thermal conductivity of pressure-less sintered Cu powder green bodies. *Powder Metall* 2021;1–12. <https://doi.org/10.1080/00325899.2021.1871806>.
- [32] Jadhav SD, Dhekne PP, Dadbakhsh S, Kruth JP, Van Humbeeck J, Vanmeensel K. Surface modified copper alloy powder for reliable laser-based additive manufacturing. *Addit Manuf* 2020;35:101418. <https://doi.org/10.1016/j.addma.2020.101418>.
- [33] Kempen K, Vrancken B, Buls S, Thijs L, Van Humbeeck J, Kruth JP. Selective laser melting of crack-free high density m2 high speed steel parts by baseplate preheating. *J Manuf Sci Eng ASME* 2014;136. <https://doi.org/10.1115/1.4028513>.
- [34] Steen WM, Mazumder J. *Laser Materials Processing*. 2010. <https://doi.org/10.1007/978-1-84996-062-5>.
- [35] Yadroitsev I, Krakhmalev P, Yadroitseva I, Johansson S, Smurov I. Energy input effect on morphology and microstructure of selective laser melting single track from metallic powder. *J Mater Process Technol* 2013;213:606–13. <https://doi.org/10.1016/j.jmatprotec.2012.11.014>.
- [36] Koutný D, Paloušek D, Pantelejev L, Hoeller C, Pichler R, Tesicky L, et al. Influence of scanning strategies on processing of aluminum alloy EN AW 2618 using selective

- laser melting. *Materials* (Basel) 2018;11:298. <https://doi.org/10.3390/ma11020298>.
- [37] Ujihara K. Reflectivity of metals at high temperatures. *J Appl Phys* 1971;43: 2376–83. <https://doi.org/10.1063/1.1661506>.
- [38] Sainte-Catherine C, Jeadin M, Kechemair D, Ricaud J-P, Sebatier L. Study of dynamic absorptivity at 10.6 μm (CO₂) and 1.06 μm (Nd-YAG) wavelengths as a function of temperature. *Le J Phys IV* 1991;01:151–7. <https://doi.org/10.1051/jp4:1991741>.
- [39] Khaskin VY, Korzhik VN, Chizhskaya TG, Sidorets VN, Zie L. Effect of laser radiation absorption on efficiency of laser welding of copper and its alloys. *Pat Weld J* 2016;2016:31–5. <https://doi.org/10.15407/tpwj2016.11.05>.
- [40] Malý M, Höller C, Skalon M, Meier B, Koutný D, Pichler R, et al. Effect of process parameters and high-temperature preheating on residual stress and relative density of Ti6Al4V processed by selective laser melting. *Materials* (Basel) 2019;12:930. <https://doi.org/10.3390/ma12060930>.
- [41] Ali H, Ma L, Ghadbeigi H, Mumtaz K. In-situ residual stress reduction, martensitic decomposition and mechanical properties enhancement through high temperature powder bed pre-heating of selective laser melted Ti6Al4V. *Mater Sci Eng A* 2017; 695:211–20. <https://doi.org/10.1016/j.msea.2017.04.033>.
- [42] Körperich JP, Merkel M. Thermographic analysis of the building height impact on the properties of tool steel in selective laser beam melting. *Materwiss Werksttech* 2018;49:689–95. <https://doi.org/10.1002/mawe.201800010>.
- [43] Vrána R, Koutný D, Paloušek D, Pantělejev L, Jaroš J, Zikmund T, et al. Selective laser melting strategy for fabrication of thin struts usable in lattice structures. *Materials* (Basel) 2018;11. <https://doi.org/10.3390/ma11091763>.
- [44] Walkowicz M, Osuch P, Smyrak B, Knych T, Rudnik E, Cieniek Ł, et al. Impact of oxidation of copper and its alloys in laboratory-simulated conditions on their antimicrobial efficiency. *Corros Sci* 2018;140:321–32. <https://doi.org/10.1016/j.corsci.2018.05.033>.
- [45] Prashanth KG, Scudino S, Maity T, Das J, Eckert J. Is the energy density a reliable parameter for materials synthesis by selective laser melting? *Mater Res Lett* 2017; 5:386–90. <https://doi.org/10.1080/21663831.2017.1299808>.
- [46] Schiaffino S, Sonin AA. Molten droplet deposition and solidification at low Weber numbers. *Phys Fluids* 1997;9:3172–87. <https://doi.org/10.1063/1.869434>.
- [47] Schiaffino S, Sonin AA. Motion and arrest of a molten contact line on a cold surface: an experimental study. *Phys Fluids* 1997;9:2217–26. <https://doi.org/10.1063/1.869344>.
- [48] Gao F, Sonin AA. Precise deposition of molten microdrops: the physics of digital microfabrication. *Proc Math Phys Sci* 1994;444:533–54.
- [49] Sidles PH, Danielson GC. Thermal conductivity of metals at high temperatures. *J Franklin Inst* 1910;169:412. [https://doi.org/10.1016/s0016-0032\(10\)90144-0](https://doi.org/10.1016/s0016-0032(10)90144-0).

7 CONCLUSIONS

This dissertation thesis deals with the application of preheating in LPBF technology. The thesis is divided into two research areas which deal with the application of preheating to decrease the residual stresses and processing of hard-to-process materials. Those two topics were identified, based on the review of the literature, as issues that hinder further technology utilization. The residual stresses limit the processing ability of some materials by LPBF and are the main cause of distortions, warping, and cracks. Thus, parts must be strongly fixed on the build platforms by support structures. However, the support structures prolong the build time, material waste, and post-process requirements. Thus, reduction of residual stresses, and consequently support structures, can lead to lower production costs. For that reason, it is important to study the techniques for their reduction. The main objective of the first topic was to experimentally analyse the influence of preheating on the Ti6Al4V and IN939 alloys.

The second topic identified as a perspective for the usage of preheating in LPBF was the processing of reflective materials. The preheating has an ability to decrease energy delivered from laser thus, it can be perspective for copper fabrication and materials with similar behaviour. Copper has excellent thermal and electrical properties, which in combination with design possibilities allowed by LPBF can lead to fabrication of unique components. However, the fabrication of fully homogeneous copper by LPBF is a challenge, and so far, fully homogeneous specimens from pure copper have not been produced. Thus, the main goal was to experimentally identify the appropriate combination of process parameters for the production of copper specimens with high relative density and to investigate the effect of high-temperature preheating.

The thesis contains original results that expand the knowledge of high-temperature preheating in LPBF. The results were confronted with studies of other research groups, and the possible usage and its limitations were stated. The main contribution of the thesis can be summarized into the following points:

- The application of preheating at 550 °C on the Ti6Al4V alloy can significantly reduce internal residual stress and increase relative density. However, even in combination with other process parameter, residual stresses were not fully eliminated.
- The application of preheating at 550 °C led to fast degradation of the unfused Ti6Al4V powder. The concentration of oxygen and hydrogen exceeds the ASTM B348 requirement limit for grade 5 titanium after one production run.
- In contrast, preheating of 400 °C led to increased deformations of IN939 specimens, thus, higher residual stresses.

- The hardness, tensile strength, and 0.2% proof stress of IN939 increased and the elongation at break decreased due to the application of preheating.
- High preheating temperature had a significant effect on the size and occurrence of the carbide phase of IN939. The occurrence and size of the carbide phase correspond to the results of increased residual stresses and mechanical properties.
- The build time had a significant effect on the evolution of the carbide phase of IN939. Longer build time resulted in larger size and the occurrence of the carbide phase. This effect was more significant in combination with higher preheating temperature.
- Rapid oxidation of the unfused IN939 powder due to the preheating temperature of 400 °C was not detected using the EDX and XRD methods.
- Copper can be fabricated with a relative density greater than 99% with an infrared fiber laser with a maximum laser power of 400 W and preheating of 400 °C .
- The relative density of copper over 99% was achieved just with application of preheating at 400 °C. Preheating at 200 °C led to maximum relative density of 96%.
- However, preheating to 400 °C caused rapid oxidation of the unfused copper powder. Thus, restricted its reusability. The increased oxidation of the fused material was not detected by EDX or XRD methods.

Regarding the scientific questions, the obtained knowledge can be summarized in the following remarks:

- Q1. No combination of process parameters and preheating up to 550 °C that would lead to the elimination of residual stresses of the Ti6Al4V alloy was found. Residual stresses decreased significantly when preheating at 550 °C was applied and the results indicated that even a higher energy density delivered by the laser would lead to further reduction of residual stress. However, preheating to 550 °C led to rapid degradation of the unfused powder. Therefore, this technique is not cost effective for the elimination of residual stresses. Thus, the hypothesis was **falsified**.
- Q2. Preheating of 400 °C, as a single changed process parameter, led to an increase in residual stresses of IN939 specimens. The increase of residual stresses was attributed to the evolution of the carbide phase. Therefore, the hypothesis that preheating can decrease residual stresses of IN939 was **falsified**.

- Q3. The preheating at 400 °C caused an increase of the relative density of copper processed by LPBF. The fabricated component reached a relative density greater than 99% while preheating was used at 400 °C. Compared to 200 °C preheating, the maximum measured relative density was 96%. Therefore, the hypothesis that the application of high-temperature preheating can lead to fabrication of copper specimens with a high relative density was **confirmed**.

8 LIST OF PUBLICATIONS

8.1 Papers published in journals with impact factor

MALÝ, Martin, Christian HÖLLER, Mateusz SKALON, Benjamin MEIER, Daniel KOUTNÝ, Rudolf PICHLER, Christof SOMMITSCH a David PALOUŠEK. Effect of Process Parameters and High-Temperature Preheating on Residual Stress and Relative Density of Ti6Al4V Processed by Selective Laser Melting. *Materials* [online]. 2019, **12**(6), 930. ISSN 1996-1944. Available at: doi:10.3390/ma12060930

MALÝ, Martin, Klára NOPOVÁ, Lenka KLAKURKOVÁ, Ondřej ADAM, Libor PANTĚLEJEV a Daniel KOUTNÝ. Effect of Preheating on the Residual Stress and Material Properties of Inconel 939 Processed by Laser Powder Bed Fusion. *Materials* [online]. 2022, **15**(18), 6360. ISSN 1996-1944. Available at: doi:10.3390/ma15186360

MALÝ, Martin, Daniel KOUTNÝ, Libor PANTĚLEJEV, Laurent PAMBAGUIAN a David PALOUŠEK. Effect of high-temperature preheating on pure copper thick-walled samples processed by laser powder bed fusion. *Journal of Manufacturing Processes* [online]. 2022, **73**, 924–938. ISSN 15266125. Available at: doi:10.1016/j.jmapro.2021.11.035

8.2 Papers in conference proceedings

HERNÁNDEZ-TAPIA, Laura, Azalia Mariel CARRANZA-TREJO, Adelia KASHIMBETOVA, Serhii TKACHENKO, Zuzana KOLEDOVÁ, Daniel KOUTNÝ, Martin MALÝ, Ladislav ČELKO a Edgar B. MONTUFAR. Microstructure of Selective Laser Melted Titanium Lattices and In Vitro Cell Behaviour. In: METAL 2021 - 30th Anniversary International Conference on Metallurgy and Materials, Conference Proceedings [online]. B.m.: TANGER Ltd., 2021, s. 1179–1185. ISBN 9788087294994. Available at: doi:10.37904/metal.2021.4259

.

9 LITERATURE

- [1] SCHLEIFENBAUM, H., W. MEINERS, K. WISSENBACH a C. HINKE. Individualized production by means of high power Selective Laser Melting. *CIRP Journal of Manufacturing Science and Technology* [online]. 2010, **2**(3), 161–169 [vid. 2016-03-12]. ISSN 17555817. Available at: doi:10.1016/j.cirpj.2010.03.005
- [2] KRUTH, J. P., L. FROYEN, J. VAN VAERENBERGH, P. MERCELIS, M. ROMBOUTS a B. LAUWERS. Selective laser melting of iron-based powder. *Journal of Materials Processing Technology* [online]. 2004, **149**(1–3), 616–622. ISSN 09240136. Available at: doi:10.1016/j.jmatprotec.2003.11.051
- [3] GU, D D, W MEINERS, K WISSENBACH a R POPRAWA. Laser additive manufacturing of metallic components: materials, processes and mechanisms. *International Materials Reviews* [online]. 2012, **57**(3), 133–164. ISSN 0950-6608. Available at: doi:10.1179/1743280411Y.0000000014
- [4] SLM SOLUTION. *SLM Solutions* [online]. [vid. 2018-01-25]. Available at: <https://slm-solutions.com/>
- [5] WITHERS, P.J. a H.K.D.H. BHADSHIA. Residual stress. Part 2 – Nature and origins. *Materials Science and Technology* [online]. 2001, **17**(4), 366–375. ISSN 0267-0836. Available at: doi:10.1179/026708301101510087
- [6] JOCHEN, Giedenbacher, Huskic AZIZ a Ognianov MILOSLAV. Investigation of microstructure and mechanical properties of gas atomized hot work tool steels manufactured by selective laser melting using powder bed preheating. In: ASMET, ed. *Metal Additive Manufacturing Conference 2018*. 2018, s. 124–134.
- [7] ALI, Haider, Hassan GHADBEIGI a Kamran MUMTAZ. Effect of scanning strategies on residual stress and mechanical properties of Selective Laser Melted Ti6Al4V. *Materials Science and Engineering A* [online]. 2018, **712**(November 2017), 175–187. ISSN 09215093. Available at: doi:10.1016/j.msea.2017.11.103
- [8] ALI, Haider, Le MA, Hassan GHADBEIGI a Kamran MUMTAZ. In-situ residual stress reduction, martensitic decomposition and mechanical properties enhancement through high temperature powder bed pre-heating of Selective Laser Melted Ti6Al4V. *Materials Science and Engineering: A* [online]. 2017, **695**, 211–220 [vid. 2017-08-17]. ISSN 09215093. Available at: doi:10.1016/j.msea.2017.04.033
- [9] ALI, Haider, Hassan GHADBEIGI a Kamran MUMTAZ. Residual stress development in selective laser-melted Ti6Al4V: a parametric thermal modelling approach. *International Journal of Advanced Manufacturing Technology* [online]. 2018, **97**(5–8), 2621–2633. ISSN 14333015. Available at: doi:10.1007/s00170-018-2104-9

- [10] SHIOMI, M., K. OSAKADA, K. NAKAMURA, T. YAMASHITA a F. ABE. Residual Stress within Metallic Model Made by Selective Laser Melting Process. *CIRP Annals - Manufacturing Technology* [online]. 2004, **53**(1), 195–198 [vid. 2015-11-18]. ISSN 00078506. Available at: doi:10.1016/S0007-8506(07)60677-5
- [11] WEIWEI, He, Jia WENPENG, Liu HAIYAN, Tang HUIPING, Kang XINTING a Huang YU. Research on Preheating of Titanium Alloy Powder in Electron Beam Melting Technology. *Rare Metal Materials and Engineering* [online]. 2011, **40**(12), 2072–2075 [vid. 2016-03-26]. ISSN 18755372. Available at: doi:10.1016/S1875-5372(12)60014-9
- [12] *Arcam EBM* [online]. Available at: <http://www.arcam.com>
- [13] CAMPBELL, I, Olaf DIEGEL, J KOWEN a T WOHLERS. *Wohlers report 2018: 3D printing and additive manufacturing state of the industry: annual worldwide progress report*. B.m.: Wohlers Associates, 2018. ISBN 0991333241.
- [14] DEBROY, T., H.L. WEI, J.S. ZUBACK, T. MUKHERJEE, J.W. ELMER, J.O. MILEWSKI, A.M. BEESE, A. WILSON-HEID, A. DE a W. ZHANG. Additive manufacturing of metallic components – Process, structure and properties. *Progress in Materials Science* [online]. 2018, **92**, 112–224. ISSN 00796425. Available at: doi:10.1016/j.pmatsci.2017.10.001
- [15] BARTLETT, Jamison L. a Xiaodong LI. An overview of residual stresses in metal powder bed fusion. *Additive Manufacturing* [online]. 2019, **27**(January), 131–149. ISSN 22148604. Available at: doi:10.1016/j.addma.2019.02.020
- [16] ZHANG, Bi, Yongtao LI a Qian BAI. Defect Formation Mechanisms in Selective Laser Melting: A Review. *Chinese Journal of Mechanical Engineering (English Edition)* [online]. 2017, **30**(3), 515–527. ISSN 21928258. Available at: doi:10.1007/s10033-017-0121-5
- [17] DOWLING, L., J. KENNEDY, S. O'SHAUGHNESSY a D. TRIMBLE. *A review of critical repeatability and reproducibility issues in powder bed fusion* [online]. B.m.: Elsevier Ltd. 15. leden 2020. ISSN 18734197. Available at: doi:10.1016/j.matdes.2019.108346
- [18] *Aconity3D* [online]. [vid. 2022-02-28]. Available at: <https://aconity3d.com/>
- [19] SOCHALSKI-KOLBUS, L. M., E. A. PAYZANT, P. A. CORNWELL, T. R. WATKINS, S. S. BABU, R. R. DEHOFF, M. LORENZ, O. OVCHINNIKOVA a C. DUTY. Comparison of Residual Stresses in Inconel 718 Simple Parts Made by Electron Beam Melting and Direct Laser Metal Sintering. *Metallurgical and Materials Transactions A: Physical Metallurgy and Materials Science* [online]. 2015, **46**(3), 1419–1432. ISSN 10735623. Available at: doi:10.1007/s11661-014-2722-2

- [20] STEEN, William M. a Jyotirmoy MAZUMDER. *Laser Material Processing* [online]. 2010. ISBN 978-1-84996-061-8. Available at: doi:10.1007/978-1-84996-062-5
- [21] UJIHARA, Kikuo. Reflectivity of metals at high temperatures. *Journal of Applied Physics* [online]. 1971, **43**(5), 2376–2383. ISSN 00218979. Available at: doi:10.1063/1.1661506
- [22] ZHOU, Xin, Xihe LIU, Dandan ZHANG, Zhijian SHEN a Wei LIU. Balling phenomena in selective laser melted tungsten. *Journal of Materials Processing Technology* [online]. 2015, **222**, 33–42. ISSN 09240136. Available at: doi:10.1016/j.jmatprotec.2015.02.032
- [23] SCHIAFFINO, Stefano a Ain A. SONIN. Motion and arrest of a molten contact line on a cold surface: An experimental study. *Physics of Fluids* [online]. 1997, **9**(8), 2217–2226. ISSN 10706631. Available at: doi:10.1063/1.869344
- [24] SCHIAFFINO, Stefano a Ain A. SONIN. Molten droplet deposition and solidification at low Weber numbers. *Physics of Fluids* [online]. 1997, **9**(11), 3172–3187. ISSN 10706631. Available at: doi:10.1063/1.869434
- [25] GAO, Fuquan a Ain A SONIN. Precise Deposition of Molten Microdrops: The Physics of Digital Microfabrication. *Proceedings: Mathematical and Physical Sciences* [online]. 1994, **444**(1922), 533–554. ISSN 09628444. Available at: <http://www.jstor.org/stable/52539>
- [26] LI, C., Z. Y. LIU, X. Y. FANG a Y. B. GUO. Residual Stress in Metal Additive Manufacturing. *Procedia CIRP* [online]. 2018, **71**, 348–353. ISSN 22128271. Available at: doi:10.1016/j.procir.2018.05.039
- [27] MERCELIS, Peter a Jean-Pierre KRUTH. Residual stresses in selective laser sintering and selective laser melting. *Rapid Prototyping Journal* [online]. 2006, **12**(5), 254–265. ISSN 1355-2546. Available at: doi:10.1108/13552540610707013
- [28] ALI, Haider, Hassan GHADBEIGI a Kamran MUMTAZ. Processing Parameter Effects on Residual Stress and Mechanical Properties of Selective Laser Melted Ti6Al4V. *Journal of Materials Engineering and Performance* [online]. 2018, **27**(8), 4059–4068. ISSN 15441024. Available at: doi:10.1007/s11665-018-3477-5
- [29] WANG, Di, Yongqiang YANG, Ziheng YI a Xubin SU. Research on the fabricating quality optimization of the overhanging surface in SLM process. *International Journal of Advanced Manufacturing Technology* [online]. 2013, **65**(9–12), 1471–1484. ISSN 02683768. Available at: doi:10.1007/s00170-012-4271-4

- [30] WANG, Di, Yongqiang YANG, Ruicheng LIU, Dongming XIAO a Jianfeng SUN. Study on the designing rules and processability of porous structure based on selective laser melting (SLM). *Journal of Materials Processing Technology* [online]. 2013, **213**(10), 1734–1742. ISSN 09240136. Available at: doi:10.1016/j.jmatprotec.2013.05.001
- [31] WEI, Lien Chin, Lili E. EHRLICH, Matthew J. POWELL-PALM, Colt MONTGOMERY, Jack BEUTH a Jonathan A. MALEN. Thermal conductivity of metal powders for powder bed additive manufacturing. *Additive Manufacturing* [online]. 2018, **21**(December 2017), 201–208. ISSN 22148604. Available at: doi:10.1016/j.addma.2018.02.002
- [32] WITHERS, P.J. a H.K.D.H. BHADSHIA. Residual stress. Part 1 – Measurement techniques. *Materials Science and Technology* [online]. 2001, **17**(4), 355–365. ISSN 0267-0836. Available at: doi:10.1179/026708301101509980
- [33] VRANCKEN, Bey, Victoria CAIN, Rob KNUTSEN a Jan VAN HUMBEECK. Residual stress via the contour method in compact tension specimens produced via selective laser melting. *Scripta Materialia* [online]. 2014, **87**, 29–32 [vid. 2016-01-14]. ISSN 13596462. Available at: doi:10.1016/j.scriptamat.2014.05.016
- [34] PATTERSON, Albert E., Sherri L. MESSIMER a Phillip A. FARRINGTON. Overhanging Features and the SLM/DMLS Residual Stresses Problem: Review and Future Research Need. *Technologies* [online]. 2017, **5**(2), 15. ISSN 2227-7080. Available at: doi:10.3390/technologies5020015
- [35] BUCHBINDER, Damien, Wilhelm MEINERS, Norbert PIRCH, Konrad WISSENBACH a Johannes SCHRAGE. Investigation on reducing distortion by preheating during manufacture of aluminum components using selective laser melting. *Journal of Laser Applications* [online]. 2014, **26**(1), 012004. ISSN 1042-346X. Available at: doi:10.2351/1.4828755
- [36] YADROITSEV, I., P. KRAKHMALOV, I. YADROITSAVA, S. JOHANSSON a I. SMUROV. Energy input effect on morphology and microstructure of selective laser melting single track from metallic powder. *Journal of Materials Processing Technology* [online]. 2013, **213**(4), 606–613 [vid. 2016-03-01]. ISSN 09240136. Available at: doi:10.1016/j.jmatprotec.2012.11.014
- [37] GUSSONE, J, Y C HAGEDORN, H GHEREKHLOO, G KASPEROVICH, T MERZOUK a J HAUSMANN. Microstructure of gamma-titanium aluminide processed by selective laser melting at elevated temperatures. *Intermetallics* [online]. 2015, **66**, 133–140. ISSN 0966-9795. Available at: doi:10.1016/j.intermet.2015.07.005

- [38] HEUSSEN, Daniel. Press Release: Green Light for New 3D Printing Process. *Fraunhofer ILT* [online]. 2017 [vid. 2020-07-20]. Available at: <https://www.ilt.fraunhofer.de/en/press/press-releases/press-release-2017/press-release-2017-08-30.html>
- [39] KEYENCE. *Laser Principles* [online]. 2017. Available at: www.keyence.com
- [40] KEMPEN, K, B VRANCKEN, S BULS, L THIJS, J VAN HUMBEECK a J P KRUTH. Selective Laser Melting of Crack-Free High Density M2 High Speed Steel Parts by Baseplate Preheating. *Journal of Manufacturing Science and Engineering-Transactions of the Asme* [online]. 2014, **136**(6). ISSN 1087-1357. Available at: [doi:10.1115/1.4028513](https://doi.org/10.1115/1.4028513)
- [41] KÖRPERICH, J.P. a M. MERKEL. Thermographic analysis of the building height impact on the properties of tool steel in selective laser beam melting. *Materialwissenschaft und Werkstofftechnik* [online]. 2018, **49**(5), 689–695. ISSN 09335137. Available at: [doi:10.1002/mawe.201800010](https://doi.org/10.1002/mawe.201800010)
- [42] BRUNHUBER AT AL. Device and method for additive manufacturing. US 2018/0297116 A1. 2018.
- [43] BAI, Y., M. QI a Y. YANG. A protective gas preheating device for 3D part. CN205888086U. 2017.
- [44] WILKES, Jan, Yves Christian HAGEDORN, Wilhelm MEINERS a Konrad WISSENBACH. Additive manufacturing of ZrO₂-Al₂O₃ ceramic components by selective laser melting. *Rapid Prototyping Journal* [online]. 2013, **19**(1), 51–57. ISSN 13552546. Available at: [doi:10.1108/13552541311292736](https://doi.org/10.1108/13552541311292736)
- [45] LIU, Qi, Yoann DANLOS, Bo SONG, Baicheng ZHANG, Shuo YIN a Hanlin LIAO. Effect of high-temperature preheating on the selective laser melting of yttria-stabilized zirconia ceramic. *Journal of Materials Processing Technology* [online]. 2015, **222**, 61–74 [vid. 2016-03-02]. ISSN 09240136. Available at: [doi:10.1016/j.jmatprotec.2015.02.036](https://doi.org/10.1016/j.jmatprotec.2015.02.036)
- [46] ZHANG XIAOWEI, GUAN JIEREN a JIANG YEHUA. Multifunctional SLM device. CN108394099. 2018.
- [47] MERTENS, R., S. DADBAKSH, J. van HUMBEECK a J.-P. KRUTH. Application of base plate preheating during selective laser melting. *Procedia CIRP* [online]. 2018, **74**, 5–11. ISSN 22128271. Available at: [doi:10.1016/j.procir.2018.08.002](https://doi.org/10.1016/j.procir.2018.08.002)
- [48] LOSERTOVÁ, Monika. Textbook. 2014.

- [49] AGIUS, Dylan, Kyriakos KOUROUSIS a Chris WALLBRINK. A Review of the As-Built SLM Ti-6Al-4V Mechanical Properties towards Achieving Fatigue Resistant Designs. *Metals* [online]. 2018, **8**(1), 75. ISSN 2075-4701. Available at: doi:10.3390/met8010075
- [50] QIU, Chunlei, Nicholas J E ADKINS a Moataz M. ATTALLAH. Microstructure and tensile properties of selectively laser-melted and of HIPed laser-melted Ti-6Al-4V. *Materials Science and Engineering A* [online]. 2013, **578**, 230–239. ISSN 09215093. Available at: doi:10.1016/j.msea.2013.04.099
- [51] XU, W., E. W. LUI, A. PATERAS, M. QIAN a M. BRANDT. In situ tailoring microstructure in additively manufactured Ti-6Al-4V for superior mechanical performance. *Acta Materialia* [online]. 2017, **125**, 390–400. ISSN 13596454. Available at: doi:10.1016/j.actamat.2016.12.027
- [52] SOLIMAN, Hatem A. a Mohamed ELBESTAWI. *Titanium aluminides processing by additive manufacturing – a review* [online]. B.m.: Springer Science and Business Media Deutschland GmbH. 1. duben 2022. ISSN 14333015. Available at: doi:10.1007/s00170-022-08728-w
- [53] SHISHKOVSKY, I, I YADROITSEV a I SMUROV. Direct selective laser melting of nitinol powder. In: M SCHMIDT, F VOLLERTSEN a M GEIGER, ed. *Laser Assisted Net Shape Engineering 7* [online]. 2012, Physics Procedia, s. 447–454. Available at: doi:10.1016/j.phpro.2012.10.060
- [54] LÖBER, Lukas, Hochschule ESSLINGEN, Sara BIAMINO, Politecnico DI TORINO a Paolo FINO. Comparison of selective laser and electron beam melted titanium aluminides. In: [online]. B.m.: 2011 International Solid Freeform Fabrication Symposium, 2011. Available at: doi:http://dx.doi.org/10.26153/tsw/15316
- [55] SHI, Xuezhi, Huaxue WANG, Wuwei FENG, Yulian ZHANG, Shuyuan MA a Jun WEI. The crack and pore formation mechanism of Ti–47Al–2Cr–2Nb alloy fabricated by selective laser melting. *International Journal of Refractory Metals and Hard Materials* [online]. 2020, **91**. ISSN 22133917. Available at: doi:10.1016/j.ijrmhm.2020.105247
- [56] DOUBENSKAIA, Maria, Alexey DOMASHENKOV, Igor SMUROV a Pavel PETROVSKIY. Study of Selective Laser Melting of intermetallic TiAl powder using integral analysis. *International Journal of Machine Tools and Manufacture* [online]. 2018, **129**, 1–14. ISSN 08906955. Available at: doi:10.1016/j.ijmachtools.2018.02.003

- [57] POLOZOV, Igor, Artem KANTYUKOV, Vera POPOVICH, Jia Ning ZHU a Anatoly POPOVICH. Microstructure and mechanical properties of TiAl-based alloy produced by selective laser melting. In: *METAL 2020 - 29th International Conference on Metallurgy and Materials, Conference Proceedings* [online]. B.m.: TANGER Ltd., 2020, s. 1037–1041. ISBN 9788087294970. Available at: doi:10.37904/metal.2020.3604
- [58] CHEN, Ruirun, Qi WANG, Yaohua YANG, Jingjie GUO, Yanqing SU, Hongsheng DING a Hengzhi FU. Brittle–ductile transition during creep in nearly and fully lamellar high-Nb TiAl alloys. *Intermetallics* [online]. 2018, **93**, 47–54. ISSN 09669795. Available at: doi:10.1016/j.intermet.2017.11.009
- [59] HEARN, William, Robert STEINLECHNER a Eduard HRYHA. Laser-based powder bed fusion of non-weldable low-alloy steels. *Powder Metallurgy* [online]. 2021. ISSN 17432901. Available at: doi:10.1080/00325899.2021.1959695
- [60] MERTENS, R., B. VRANCKEN, N. HOLMSTOCK, Y. KINDS, J.-P. KRUTH a J. VAN HUMBEECK. Influence of Powder Bed Preheating on Microstructure and Mechanical Properties of H13 Tool Steel SLM Parts. *Physics Procedia* [online]. 2016, **83**, Physics Procedia, 882–890. ISSN 18753892. Available at: doi:10.1016/j.phpro.2016.08.092
- [61] KRELL, Julian, Arne RÖTTGER, Karina GEENEN a Werner THEISEN. General investigations on processing tool steel X40CrMoV5-1 with selective laser melting. *Journal of Materials Processing Technology* [online]. 2018, **255**(January), 679–688. ISSN 09240136. Available at: doi:10.1016/j.jmatprotec.2018.01.012
- [62] BOES, J., A. RÖTTGER, C. MUTKE, C. ESCHER a W. THEISEN. Microstructure and mechanical properties of X65MoCrWV3-2 cold-work tool steel produced by selective laser melting. *Additive Manufacturing* [online]. 2018, **23**(July), 170–180. ISSN 22148604. Available at: doi:10.1016/j.addma.2018.08.005
- [63] SANCHEZ, Salomé, Peter SMITH, Zhengkai XU, Gabriele GASPARD, Christopher J. HYDE, Wessel W. WITS, Ian A. ASHCROFT, Hao CHEN a Adam T. CLARE. Powder Bed Fusion of nickel-based superalloys: A review. *International Journal of Machine Tools and Manufacture* [online]. 2021, **165**. ISSN 08906955. Available at: doi:10.1016/j.ijmachtools.2021.103729
- [64] WARREN, J. a D. Y. WEI. The cyclic fatigue behavior of direct age 718 at 149, 315, 454 and 538 °C. *Materials Science and Engineering A* [online]. 2006, **428**(1–2), 106–115. ISSN 09215093. Available at: doi:10.1016/j.msea.2006.04.091

- [65] KANAGARAJAH, P., F. BRENNE, T. NIENDORF a H.J. MAIER. Inconel 939 processed by selective laser melting: Effect of microstructure and temperature on the mechanical properties under static and cyclic loading. *Materials Science and Engineering: A* [online]. 2013, **588**, 188–195. ISSN 09215093. Available at: doi:10.1016/j.msea.2013.09.025
- [66] DONACHIE, MATTHEW J. DONACHIE, Stephen J. *Superalloys: A Technical Guide, 2nd Edition* [online]. 2. vyd. B.m.: ASM International, 2002. ISBN 978-0871707499. Available at: https://books.google.cz/books/about/Superalloys.html?id=vjCJ5pI1QpkC&redir_esc=y
- [67] HAGEDORN, Y C, J RISSE, W MEINERS, N PIRCH, K WISSENBACH a R POPRAWA. Processing of nickel based superalloy MAR M-247 by means of High Temperature - Selective Laser Melting (HT - SLM). *High Value Manufacturing: Advanced Research in Virtual and Rapid Prototyping* [online]. 2014, 291–295. Available at: https://www.researchgate.net/publication/288236755_Processing_of_nickel_base_d_superalloy_MAR_M-247_by_means_of_High_Temperature_-_Selective_Laser_Melting_HT_-_SLM
- [68] PARK, Jung-Hyun, Gyung Bae BANG, Kee-Ahn LEE, Yong SON, Yeong Hwan SONG, Byoung-Soo LEE, Won Rae KIM a Hyung Giun KIM. Effect of Preheating Temperature on Microstructural and Mechanical Properties of Inconel 718 Fabricated by Selective Laser Melting. *Metals and Materials International* [online]. 2022. ISSN 1598-9623. Available at: doi:10.1007/s12540-022-01169-w
- [69] MIRKOOHI, Elham, Steven Y. LIANG, Hong Chuong TRAN, Yu Lung LO, You Cheng CHANG a Hung Yu LIN. Mechanics modeling of residual stress considering effect of preheating in laser powder bed fusion. *Journal of Manufacturing and Materials Processing* [online]. 2021, **5**(2). ISSN 25044494. Available at: doi:10.3390/jmmp5020046
- [70] KOUTNY, Daniel, David PALOUSEK, Libor PANTELEJEV, Christian HOELLER, Rudolf PICHLER, Lukas TESICKY a Jozef KAISER. Influence of Scanning Strategies on Processing of Aluminum Alloy EN AW 2618 Using Selective Laser Melting. *Materials* [online]. 2018, **11**(2), 298. ISSN 1996-1944. Available at: doi:10.3390/ma11020298
- [71] UDDIN, Syed Z., Lawrence E. MURR, Cesar A. TERRAZAS, Philip MORTON, David A. ROBERSON a Ryan B. WICKER. Processing and characterization of crack-free aluminum 6061 using high-temperature heating in laser powder bed fusion additive manufacturing. *Additive Manufacturing* [online]. 2018, **22**(June), 405–415. ISSN 22148604. Available at: doi:10.1016/j.addma.2018.05.047

- [72] VORA, Pratik, Rafael MARTINEZ, Neil HOPKINSON, Iain TODD a Kamran MUMTAZ. Customised Alloy Blends for In-Situ Al339 Alloy Formation Using Anchorless Selective Laser Melting. *Technologies* [online]. 2017, **5**(2), 24. ISSN 2227-7080. Available at: doi:10.3390/technologies5020024
- [73] VORA, Pratik, Kamran MUMTAZ, Iain TODD a Neil HOPKINSON. AlSi12 in-situ alloy formation and residual stress reduction using anchorless selective laser melting. *Additive Manufacturing* [online]. 2015, **7**, 12–19. ISSN 22148604. Available at: doi:10.1016/j.addma.2015.06.003
- [74] TRAN, Thang Q., Amutha CHINNAPPAN, Jeremy Kong Yoong LEE, Nguyen Huu LOC, Long T. TRAN, Gengjie WANG, Vishnu Vijay KUMAR, W. A.D.M. JAYATHILAKA, Dongxiao JI, Mrityunjay DODDAMANI a Seeram RAMAKRISHNA. 3D printing of highly pure copper. *Metals* [online]. 2019, **9**(7), 12–20. ISSN 20754701. Available at: doi:10.3390/met9070756
- [75] CONSTANTIN, Loic, Zhipeng WU, Nan LI, Lisha FAN, Jean François SILVAIN a Yong Feng LU. Laser 3D printing of complex copper structures. *Additive Manufacturing* [online]. 2020, **35**(March), 101268. ISSN 22148604. Available at: doi:10.1016/j.addma.2020.101268
- [76] FRIGOLA, Pedro, Ola HARRYSSON, T J HORN, Harvey WEST, Ronald AMAN, J M RIGSBEE, D A RAMIREZ, Lawrence MURR, Francisco MEDINA, R B WICKER a E RODRIGUEZ. Fabricating Copper Components with Electron Beam Melting. *Advanced Materials and Processes*. 2014, **172**, 20–24.
- [77] EL-WARDANY, Tahany I., Ying SHE, Vijay N. JAGDALE, Jacquelynn K. GAROFANO, Joe J. LIOU a Wayne R. SCHMIDT. Challenges in Three-Dimensional Printing of High-Conductivity Copper. *Journal of Electronic Packaging, Transactions of the ASME* [online]. 2018, **140**(2), 1–12. ISSN 15289044. Available at: doi:10.1115/1.4039974
- [78] POGSON, S. R., P. FOX, C. J. SUTCLIFFE a W. O'NEILL. The production of copper parts using DMLR. *Rapid Prototyping Journal* [online]. 2003, **9**(5), 334–343. ISSN 13552546. Available at: doi:10.1108/13552540310502239
- [79] LODES, Matthias A., Ralf GUSCHLBAUER a Carolin KÖRNER. Process development for the manufacturing of 99.94% pure copper via selective electron beam melting. *Materials Letters* [online]. 2015, **143**, 298–301 [vid. 2019-06-12]. ISSN 0167-577X. Available at: doi:10.1016/J.MATLET.2014.12.105
- [80] JIANG, Qi, Peilei ZHANG, Zhishui YU, Haichuan SHI, Di WU, Hua YAN, Xin YE, Qinghua LU a Yingtao TIAN. *A review on additive manufacturing of pure copper* [online]. B.m.: MDPI AG. 1. červen 2021. ISSN 20796412. Available at: doi:10.3390/coatings11060740

- [81] LYKOV, P.A., E.V. SAFONOV a A.M. AKHMEDIANOV. Selective Laser Melting of Copper. *Materials Science Forum* [online]. 2016, **843**(3), 284–288. ISSN 1662-9752. Available at: doi:10.4028/www.scientific.net/MSF.843.284
- [82] KADEN, Lisa, Gabor MATTHÄUS, Tobias ULLSPERGER, Hannes ENGELHARDT, Markus RETTENMAYR, Andreas TÜNNERMANN a Stefan NOLTE. Selective laser melting of copper using ultrashort laser pulses. *Applied Physics A* [online]. 2017, **123**(9), 596. ISSN 0947-8396. Available at: doi:10.1007/s00339-017-1189-6
- [83] TREVISTAN, Francesco, Flaviana CALIGNANO, Massimo LORUSSO, Mariangela LOMBARDI, Diego MANFREDI a Paolo FINO. Selective laser melting of chemical pure copper powders. In: *Euro PM 2017* [online]. 2017. Available at: <https://www.epma.com/publications/euro-pm-proceedings/product/ep17-3685087>
- [84] SIDLES, P. H. a G. C. DANIELSON. Conductivity of metals at high temperatures. *Ames Laboratory ISC Technical Reports*. 36. [online]. 1951, **36**. Available at: <https://linkinghub.elsevier.com/retrieve/pii/S0016003210901440>
- [85] IKESHOJI, Toshi-Taka, Kazuya NAKAMURA, Makiko YONEHARA, Ken IMAI a Hideki KYOGOKU. Selective Laser Melting of Pure Copper. *JOM* [online]. 2018, **70**(3), 396–400. ISSN 1047-4838. Available at: doi:10.1007/s11837-017-2695-x
- [86] COLOPI, M., L. CAPRIO, A.G. DEMIR a B. PREVITALI. Selective laser melting of pure Cu with a 1 kW single mode fiber laser. *Procedia CIRP* [online]. 2018, **74**, 59–63 [vid. 2019-06-12]. ISSN 22128271. Available at: doi:10.1016/j.procir.2018.08.030
- [87] JADHAV, S.D., S. DADBAKSH, L. GOOSSENS, J-P KRUTH, J. VAN HUMBEECK a K. VANMEENSEL. Influence of selective laser melting process parameters on texture evolution in pure copper. *Journal of Materials Processing Technology* [online]. 2019, **270**, 47–58 [vid. 2019-06-12]. ISSN 09240136. Available at: doi:10.1016/j.jmatprotec.2019.02.022
- [88] HORI, Eiji, Yuji SATO, Tomoki SHIBATA, Koji TOJO a Masahiro TSUKAMOTO. Development of SLM process using 200 W blue diode laser for pure copper additive manufacturing of high density structure. *Journal of Laser Applications* [online]. 2021, **33**(1), 012008. ISSN 1042-346X. Available at: doi:10.2351/7.0000311
- [89] KRUTH, J P, J DECKERS, E YASA a R WAUTHLE. Assessing and comparing influencing factors of residual stresses in selective laser melting using a novel analysis method. *Proceedings of the Institution of Mechanical Engineers Part B-Journal of Engineering Manufacture* [online]. 2012, **226**(B6), 980–991. ISSN 0954-4054. Available at: doi:10.1177/0954405412437085

- [90] LE ROUX, Sabine, Mehdi SALEM a Anis HOR. Improvement of the bridge curvature method to assess residual stresses in selective laser melting. *Additive Manufacturing* [online]. 2018, **22**(November 2017), 320–329. ISSN 22148604. Available at: doi:10.1016/j.addma.2018.05.025
- [91] G. LUTJERING, J. C. Williams. *Titanium*. 2nd editio. B.m.: Springer, 2007. ISBN 978-3-540-71397-5.
- [92] TANG, H. P., M. QIAN, N. LIU, X. Z. ZHANG, G. Y. YANG a J. WANG. Effect of Powder Reuse Times on Additive Manufacturing of Ti-6Al-4V by Selective Electron Beam Melting. *Jom* [online]. 2015, **67**(3), 555–563. ISSN 15431851. Available at: doi:10.1007/s11837-015-1300-4
- [93] YAN, M., W. XU, M. S. DARGUSCH, H. P. TANG, M. BRANDT a M. QIAN. Review of effect of oxygen on room temperature ductility of titanium and titanium alloys. *Powder Metallurgy* [online]. 2014, **57**(4), 251–257. ISSN 0032-5899. Available at: doi:10.1179/1743290114Y.0000000108
- [94] YAN, M., M. S. DARGUSCH, T. EBEL a M. QIAN. A transmission electron microscopy and three-dimensional atom probe study of the oxygen-induced fine microstructural features in as-sintered Ti-6Al-4V and their impacts on ductility. *Acta Materialia* [online]. 2014, **68**, 196–206. ISSN 13596454. Available at: doi:10.1016/j.actamat.2014.01.015
- [95] SILVERSTEIN, Ravit a Dan ELIEZER. Hydrogen trapping in 3D-printed (additive manufactured) Ti-6Al-4V. *Materials Characterization* [online]. 2018, **144**(April), 297–304. ISSN 10445803. Available at: doi:10.1016/j.matchar.2018.07.029
- [96] TAL-GUTELMACHER, E. a D. ELIEZER. High fugacity hydrogen effects at room temperature in titanium based alloys. *Journal of Alloys and Compounds* [online]. 2005, **404–406**(SPEC. ISS.), 613–616. ISSN 09258388. Available at: doi:10.1016/j.jallcom.2004.12.172
- [97] XU, Jianjun, Xin LIN, Pengfei GUO, Yunlong HU, Xiaoli WEN, Lei XUE, Jianrui LIU a Weidong HUANG. The effect of preheating on microstructure and mechanical properties of laser solid forming IN-738LC alloy. *Materials Science and Engineering A* [online]. 2017, **691**, 71–80. ISSN 09215093. Available at: doi:10.1016/j.msea.2017.03.046
- [98] LINGQIN, Xia, Chen GUANG, Zheng LUYU a Lu PAN. Explore the feasibility of fabricating pure copper parts with low-laser energy by selective laser melting. *Materials Research Express* [online]. 2020, **7**(10). ISSN 20531591. Available at: doi:10.1088/2053-1591/abbd08

- [99] OTT, Jonas, Andreas BURGHARDT, Dominik BRITZ a Frank MÜCKLICH. Influence of porosity and impurities on the thermal conductivity of pressure-less sintered Cu powder green bodies. *Powder Metallurgy* [online]. 2021, **0**(0), 1–12. ISSN 17432901. Available at: doi:10.1080/00325899.2021.1871806

10 LIST OF FIGURES AND TABLES

10.1 List of figures

Fig. 1-1 Laser powder bed fusion (LPBF) production principle. [4].....	12
Fig. 2-1 a) Example of classification of residual stresses into three categories [15]; b) origin of the type I residual stress [27].	15
Fig. 2-2 a) warping principle; b) warping accumulation principle. [29]	16
Fig. 2-3 a) influence of the absorption ratio on the laser wavelength [39]; b) influence of the temperature on the material reflectivity for 1064 nm wavelength [21].....	18
Fig. 2-4 The effect of powder bed preheating of LPBF processed Ti6Al4V; a) on the mechanical properties, b) on the residual stress. [8]	20
Fig. 2-5 The schema of scanning strategies used for assess the influence on the residual stress; a) meander with 45° rotation angle, b) meander with 90° rotation angle, c) chessboard scanning strategy, d) chessboard scanning strategy with 45° rotation angle , e) chessboard scanning strategy with 90° rotation angle. [7].....	21
Fig. 2-6 a) The effect of scanning strategy of LPBF processed Ti6Al4V on the residual stress; b) the effect of the chessboard scanning strategy vector length on the temperature and cooling rate. [7]	22
Fig. 2-7 a) Change of Al content as a function of energy density and preheating temperature; b) Quasi-binary Ti-Al phase diagram; c) XRD spectra for LPBF Ti45Al2Cr2Nb alloy processed at different energy density and preheating temperatures. [37].....	24
Fig. 2-8 Ti48Al2Cr2Nb processed using LPBF a-c) cross section image of specimen produced under different preheating temperatures d) influence of scanning speed and preheating temperature on the relative density. [57]	25
Fig. 2-9 M2 HSS tool steel processed using LPBF in combination with base-plate preheating a) Without preheating; b) Preheating at 90 °C; c) Preheating at 150 °C; d) Preheating at 200 °C. [40].....	26
Fig. 2-10 M2 HSS tool steel processed using LPBF in combination with base-plate preheating a) the effect on relative density; b) the effect on top surface roughness. [40]..	26
Fig. 2-11 Influence of preheating temperature and laser velocity on weld track geometrical properties made of 316L a) weld track cross-section; b) graphical representation. [36] ...	27

Fig. 2-12 Influence of preheating temperature on properties of H13 tool steel on: a) mechanical properties; b) Vickers microhardness measured on cross-sectioned specimens. [60]	28
Fig. 2-13 Influence of preheating temperature on properties of H13 tool steel on: a) relative density and crack length; b) unfused powder oxidation and solidified material oxygen uptake. [61]	29
Fig. 2-14 a) Classification of nickel-based superalloys based on susceptibility to weld cracking as a function of aluminium and titanium content [66].; b) SEM image of microstructure of MAR M-247 alloy produced without cracks with applied preheating at 1200 °C [67]......	30
Fig. 2-15 Effect of preheating temperature of 50, 100 and 150 °C on IN718; a) mechanical properties; b) micro hardness; c) residual stresses. [68]	31
Fig. 2-16 Effect of preheating temperature of 50 and 150 °C on microstructure of IN718; a) preheating at 50 °C; b) preheating at 150 °C. [68].....	31
Fig. 2-17 Validation of analytical model for predicting the residual stresses of IN718; a) σ_x direction; b) σ_z direction (build direction) [69]	32
Fig. 2-18 Effect of preheating on residual stress of IN718 prediction of analytical model; a) σ_x direction; b) σ_z direction (build direction) [69]	32
Fig. 2-19 Effect of preheating on AlSi10Mg: a) distortions of cut specimens; b) microhardness. [35].....	33
Fig. 2-20 EN AW 2618 processed by LPBF with preheating at 400 °C. Specimens with chessboard scanning strategy and gradually decreasing laser velocity. [70].....	34
Fig. 2-21 Cross-section LOM images of EN AW 6061 alloy; a) non-preheated specimen, XY section; b) non-preheated specimen, XZ section (building direction); c) preheated specimen at 500 °C, XY section; d) preheated specimen at 500 °C, XZ section. [71].....	35
Fig. 2-22 Test specimen in-situ fused to Al339 alloy from a blend of two alloys fabricated at preheating of 380 °C with 10 mm overhang. [72].....	35
Fig. 2-23 Pure copper produced using LPBF. [82]	36
Fig. 2-24 Copper produced using LPBF in combination with preheating at 100 °C. [83].	37
Fig. 2-25 a) Process map for copper processing using LPBF; b) cross-section of copper specimen showing relatively homogeneous center and porous borders. [86]	38
Fig. 2-26 a) Copper fabricated using blue diode laser; b) Scanning strategy for reaching relative density of 99.1 %. [88].....	39
Fig. 5-1 Bridge-shaped specimen in the cut state with dimensions and marked top surface (red dotted line).....	52

10.2 List of tables

Tab. 5-1 Chemical composition of virgin Ti6Al4V powder in weight percentage (wt. %).	51
Tab. 5-2 Chemical composition of virgin IN939 powder in weight percentage (wt. %)...	51
Tab. 5-3 Chemical composition of virgin copper powder delivered by vendor.	51

11 LIST OF SYMBOLS AND ABBREVIATIONS

AM	Additive manufacturing
PBF	Powder bed fusion
LPBF	Laser powder bed fusion
SLM	Selective laser melting
EBM	Electron beam melting
SEM	Scanning electron microscope
EDX	Energy-dispersive X-ray spectroscopy
XRD	X-ray diffraction
IN718	Inconel 718
IN939	Inconel 939
Q	Energy necessary for melting the powder (J/m^3)
ρ	Material density (kg/m^3)
c_p	Specific heat ($\text{J}/\text{kg}/\text{K}$)
T	Temperature (K)
L_f	Latent heat (J/K)
E_o	Volumetric energy density (J/mm^3)
LP	Laser power (W)
LV	Laser velocity(mm/s)
HD	distance between two neighbouring laser paths (mm)
LT	Powder layer thickness (mm)

